MEV SPECTROSCOPY FOR ULTRA-INTENSE LASER-MATTER INTERACTIONS

by

Siyu Luo

A dissertation submitted to the Faculty of the University of Delaware in partial fulfillment of the requirements for the degree of Doctor of Philosophy in Physics

Fall 2019

MEV SPECTROSCOPY FOR ULTRA-INTENSE LASER-MATTER INTERACTIONS

by

Siyu Luo

Approved: _____
Edmund R. Nowak, Ph.D.
Chair of the Department of Physics and Astronomy

Approved: _____
John A. Pelesko, Ph.D.
Dean of the College of Arts and Sciences

Approved: _____
Douglas J. Doren, Ph.D.
Interim Vice Provost for Graduate and Professional Education and
Dean of the Graduate College

I certify that I have read this dissertation and that in my opinion it meets the academic and professional standard required by the University as a dissertation for the degree of Doctor of Philosophy.

Signed: _____

Barry C. Walker, Ph.D.
Professor in charge of dissertation

I certify that I have read this dissertation and that in my opinion it meets the academic and professional standard required by the University as a dissertation for the degree of Doctor of Philosophy.

Signed: _____

Yi Ji, Ph.D.
Member of dissertation committee

I certify that I have read this dissertation and that in my opinion it meets the academic and professional standard required by the University as a dissertation for the degree of Doctor of Philosophy.

Signed: _____

Matthew F. DeCamp, Ph.D.
Member of dissertation committee

I certify that I have read this dissertation and that in my opinion it meets the academic and professional standard required by the University as a dissertation for the degree of Doctor of Philosophy.

Signed: _____

James MacDonald, Ph.D.
Member of dissertation committee

I certify that I have read this dissertation and that in my opinion it meets the academic and professional standard required by the University as a dissertation for the degree of Doctor of Philosophy.

Signed: _____

Andrew V. Teplyakov, Ph.D.
Member of dissertation committee

ACKNOWLEDGEMENTS

I am incredibly grateful for all the people who have helped my research and education during graduate school. I am would like to express my most sincere gratitude to my mentor and advisor, Dr. Barry C. Walker, for his extraordinary guidance throughout this journey. He has always be extremely engaging with my research, lead me to correct decisions, encouraged me to carry on when I am down. I wish to thank him from the bottom of my heart. I would also like to thank my committee members, who took valuable time out of their busy schedules to help me with my dissertation and participated in my defense. I am most certainly thankful to all the faculty in the department, for providing top of the line lectures, and of course all the staff, you make me feel like I have a second home at the opposite side of the earth. My gratitude to Maura Perkins and Elizabeth Bornemann for their kindness. I would also like to thank master machinists, Tom Reed and Derrick Allen for their incredible help over the years. My gratitude also goes to Dr. John Shaw and Dr. Everett Ramer, for giving me tremendous help on teaching.

I would like to thank my colleagues, Sui Luo, together with his loving wife, Jieru Zhang, for helping me adapting when I first came here, giving me a sense of security on a foreign land. Patrick Grugan, who gave me so much valuable advice in my research and always so fun to communicate with. I would also like to acknowledge the overall help and valuable friendship I have received from my fellow graduate students Yunjiao Cai, Xiangyu Ma, Wenrui Wang, Xingyu Shen and Onur Tosun. I wish you all the best in the future.

There have been many undergraduate students who helped me perform the experiments. Zach Germain, always there with me, starting up the laser, aligning the laser, shutting down the laser. Amylia Hoos and Zahide Demircioglu, patiently taking

the measurements hours after hours. Sam Hughes and Jacques Samaha, together we have disassembled and reassembled the spectrometer and electromagnet so many times. Jacques Samaha, It was always an pleasure working with them.

I am forever in debt to my loving family. Though out the years, my parents, Yongchong Luo, Yuan Xu, never stop giving me their unconditional love and incredible support from thousands of miles away. They always have faith in me, they never make me feels alone. My heartfelt thank you to Qiongxia Liu, for all her love and support, I would like to give one special gratitude to my grandfather, Guanyu Luo, who lead me into the world of science. For that, I dedicated this dissertation to him.

TABLE OF CONTENTS

LIST OF TABLES

LIST OF FIGURES

ABSTRACT

Strong and ultrastrong field light-matter interactions encompass topics across atomic and molecular physics, high harmonic generation, fusion science, quantum control, and molecular imaging, which includes x-ray ionization, multi-photoionization, tunneling ionization, and classical over the barrier ionization. Current laser technology has enabled us to generate terawatts (10^{12} watts) or even petawatts (10^{15} watts) of optical power, while being focused down to spots as small as few micrometers, can generate peak intensity up to 10^{22} W/cm^2. The traditional understanding of light-matter interactions breaks down at these extremely high intensities as the liberated photoelectrons possess speed highly close to that of light ($v/c \approx 1$) therefore entering the relativistic regime. Furthermore, the dynamics of relativistic photoelectrons change significantly since the effect of the laser magnetic field is no longer negligible. Traditional laser-matter spectroscopy techniques fail to accurately analyze photoelectrons and ions from ultrahigh intensity studies with terawatt and petawatt laser systems. The work presented in this dissertation is to offer some insights and measurements of photoelectron yields and energies of the ionization of chloromethane (CH_3Cl) and argon (Ar) in an ultrastrong laser field with intensities up to 10^{19} W/cm^2 as well as present a magnetic deflection, photoelectron spectrometer for ultrahigh intensity (10^{19} W/cm^2) laser interactions with atoms and molecules in the single atom/molecule limit, includes the spectrometer fabrication and calibration, noise background as well as example photoelectron spectra for argon and chloromethane over an energy range from 20 keV to 2 MeV.

Chapter 1

INTRODUCTION

1.1 Motivation

The interactions between light and matter have always been an important field in fundamental science. During the past few decades, the boundaries of this elementary interaction have been pushed by the rapid development of strong and ultrastrong fields of light. Strong and ultrastrong field light-matter interactions encompass a broad range of topics including the ultimate energy limit of [1] coherent x-ray generation [2] by high harmonic generation [3], pair creation [4], laser initiated nuclear reactions [5], and high field vacuum-polarization effects [6] to name a few.

Electrical field strength and magnetic field strength of such ultrahigh intense laser field can go up to 10^{12} V/cm and 10^{8} T, respectively. Atoms and molecules exposed to such tremendous fields ionize dozens of electrons with merely a few optical cycles of the laser field. Photoelectrons in this extreme environment can absorb hundreds of thousands of laser photons and having energy up to MeV level, therefore, entering the relativistic regime. Furthermore, the dynamics of relativistic photoelectrons presents a new frontier for light-matter interactions due to the inclusion of the laser magnetic field. Considerable photoelectron energies and more complicated photoelectron trajectories have a significant impact on the scattering process and radiation mechanisms occurring in the ultrastrong field. The dynamics of atoms and molecules in ultrahigh intensity field is still under-investigated and is an area of exciting new science. The new frontiers in high intensity laser science include, for example, attosecond science, high energy density physics, astrophysics, particle physics, nuclear physics, and laser-driven neutron and positron sources. Many experiments performed with terawatt and petawatt lasers address topics in relativistic laser-plasma physics and high

energy density science [7]. Fundamental studies of atoms and molecules continue to be of interest in their own right and as part of the single particle response that forms the underpinnings within relativistic laser plasma physics and high energy density science. Strong field atomic ionization is also one of the limited numbers of options [8] available to independently measure the peak intensity at the laser focus.

1.2 Description of Laser

Lasers are devices that generate or amplify coherent radiation at frequencies in the infrared, visible, or ultraviolet regions of the electromagnetic spectrum. The beams of radiation that lasers emit or amplify have remarkable properties of continuity, spectra purity, and intensity [9]. These properties have already led to an enormous variety of applications. The essential elements if a laser device is the following. A gain medium consisting of an appropriate collection of atoms, molecules, ions or in some cases semiconducting crystals, a pumping process to excite these medium in to higher energy levels, and suitable optical feedback elements that allow a beam of radiation to either pass once through the laser medium or bounce back and forth repeatedly through the laser medium.

If we are only to consider the case of linearly polarized light and treat the electromagnetic field classically, which is the case in the experiments discussed in this work, we can write the laser electric and magnetic field as.

$$\mathbf{E} = \mathbf{E}_0 cos(\omega t) \tag{1.1}$$

$$\mathbf{H} = \mathbf{H}_0 cos(\omega t) \tag{1.2}$$

where c is the speed of light. $\omega = 2\pi f$ is the angular frequency, t is the time and $\mathbf{E}_0$ and $\mathbf{H}_0$ are the peak electric field and magnetic field, respectively.

The optical intensity, I, of a laser beam at some location, is, in most cases, understood to be the optical power per unit area, which is transmitted through an imagined surface perpendicular to the propagation direction. The units of the optical

intensity (or light intensity) are W/m^2 or more commonly W/cm^2. The intensity is the product of photon energy and photon flux. For a laser beam with a flat-top intensity profile, namely, with a constant intensity over some area and zero intensity outside, the optical intensity is simply the optical power P divided by the beam area. For a Gaussian beam with optical power P and Gaussian beam radius r, the peak intensity on the beam axis is

$$I_{peak} = \frac{P}{\pi r^2/2} \tag{1.3}$$

In order to obtain ultrahigh intensities, the laser beam needs to be tightly focused to an extremely small focal point. Here I_{peak} introduces the Gaussian laser focus, as the spatial profile of the experimental laser used in this study is Gaussian (TEM_{00})

Due to diffraction, a Gaussian beam will converge and diverge from an area called the beam waist (ω_0), which is where the beam diameter reaches a minimum value, as shown in figure 1.1. The beam converges and diverges equally on both sides of the beam waist by the divergence angle θ. The beam waist and divergence angle are both measured from the axis, and Equation (1.4) and Equation (1.5) express their relationship.

$$\omega_0 = \frac{\lambda}{\pi\theta} \tag{1.4}$$

$$\theta = \frac{\lambda}{\pi\omega_0} \tag{1.5}$$

In the equations above, λ is the wavelength of the laser, and θ is a far-field approximation. Variation of the beam diameter in the beam waist region is defined by:

$$\omega(z)^2 = \omega(0)^2 + \left(\theta^2 z^2\right) \tag{1.6}$$

$$\omega(z) = \sqrt{1 + \left(\frac{\lambda z}{\pi\omega_0^2}\right)} \tag{1.7}$$

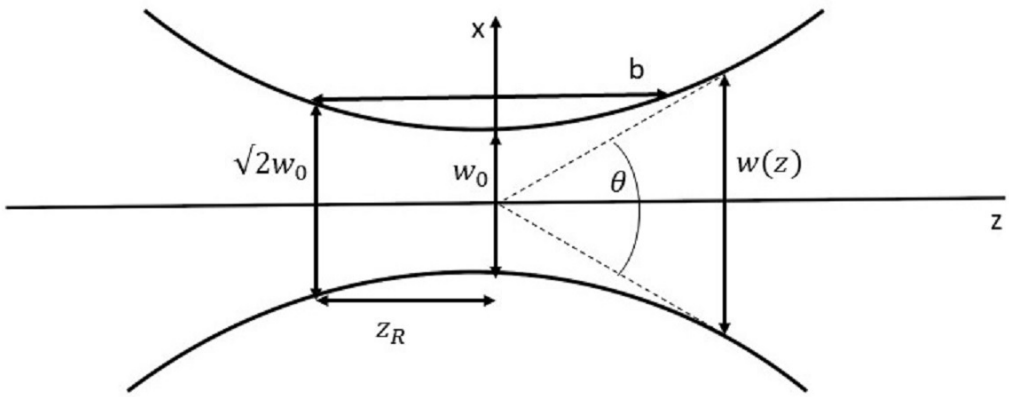

(a)

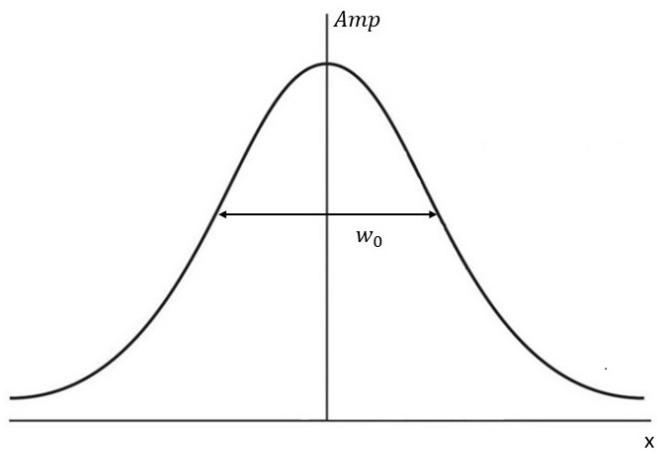

(b)

Figure 1.1: Beam profiles of a Gaussian laser focus. (a) Variation of the transverse beam width, w, as a function of the axial distance, z. The minimum beam diameter is w_0. (b) The transverse intensity distribution of the beam showing the TEM_{00} spatial profile at the laser focus.

The Rayleigh range of a Gaussian beam is defined as the value of z where the cross-sectional area of the beam is doubled. This occurs when $w(z)$ has increased to 2 w_0. Using Equation (1.5), the Rayleigh range (z_R) can be expressed as:

$$z_R = \frac{\pi \omega_0^2}{\lambda} \tag{1.8}$$

$$\omega_z = \omega_0 \sqrt{1 + \left(\frac{z}{z_R}\right)} \tag{1.9}$$

This allows $\omega(z)$ to also be related to z_R.

Therefore, the transverse intensity value of a Gaussian beam with peak power P is given by

$$I\left(x, z\right) = \frac{2P}{\pi \omega\left(z\right)} \cdot exp\left(-\frac{2x^2}{\omega\left(z\right)^2}\right) \tag{1.10}$$

where x is the transverse distance measured from propagation axis. The volume, V, of an isointensity profile of a Gaussian laser focus is defined as

$$V = \frac{\pi^2 w_0^4}{\lambda}\left(\frac{2}{9}\xi^3 + \frac{4}{3}\xi - \frac{4}{3}tan^{-1}\left(\xi\right)\right) \tag{1.11}$$

where $\xi = \sqrt{I_0/I - 1}$ and I_0 is the peak intensity [10].

1.3 Ionization dynamics in intense Laser fields

The ionization of atoms by strong or ultrastrong laser fields plays an important role in today's ultrafast laser laboratories. It is at the basis of important techniques such as high harmonic generation [11], which allows the production of attosecond ($1as = 10^{-18}s$) laser pulses [12], and furthermore allows the development of tomographic methods that make it possible to observe ultrafast electronic and atomic movements on the attosecond to few femtosecond ($1fs = 10^{-15}s$) timescale [13]. The most straightforward mechanism is the single photon ionization, where atom absorbs energy $E = hv$, from one photon, and released an electron to the continuum. Provided that the energy absorbed is equal to the ionization potential, which usually occurs at relatively low intensities in the order of 10^{12} W/cm^2 or lower.

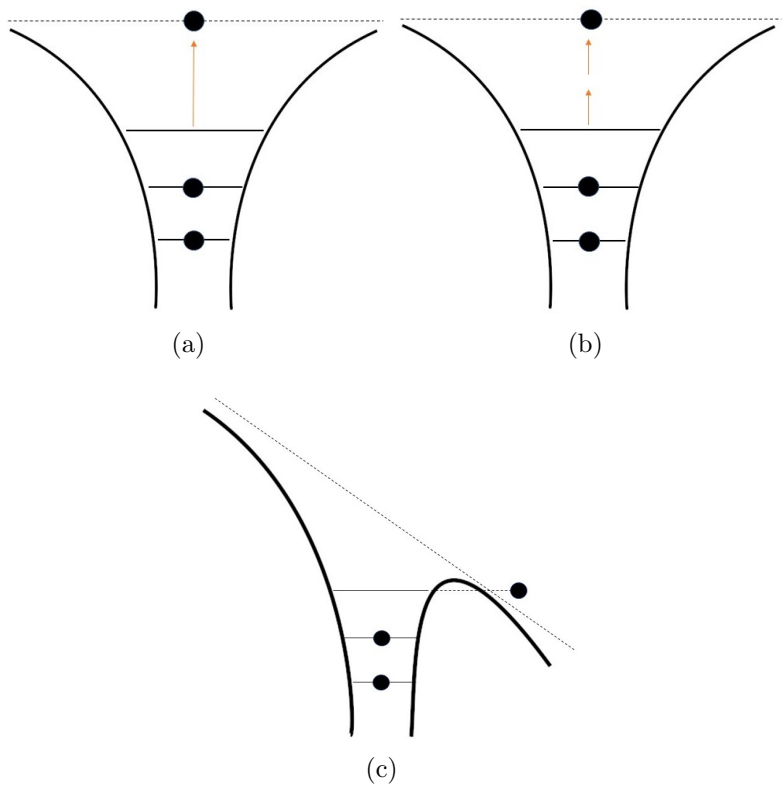

Figure 1.2: Schematic of (a) single photon ionization, (b) multiphoton ionization, and (c) tunneling ionization mechanisms.

A multiphoton process is defined here as the interaction between radiation and matter, accompanied by absorption or emission of no less than two photons. The probability of such a simple act cannot be formally represented in the form of a product of the probability of absorption and emission of individual photons [14]. As the intensity of the incident radiation increases to $10^{12} - 10^{14}$ W/cm^2, the atom may absorb a sufficient number of low energy photons each with energy hv to release an electron with an ionization potential equal to the sum of the absorbed photon energies. This mechanism is generally referred to as multiphoton ionization (MPI). If the atom absorbs N photons to release an electron with an ionization potential of Nhv, the process is known as N-photon ionization. As the intensity increases further ($> 10^{14}$ W/cm^2), the field strength of the incident radiation is strong enough to deform the Coulomb potential of the atom and electron now tunnels through the suppressed barrier and enters the continuum. As the intensity further increases, the barrier deformation increases allowing successive tunneling of more tightly bound electrons [15]. Therefore, this process where the electrons are ionized one after another in the increasing radiation field is known as sequential ionization (SI). The method implemented by Ammosov, Delone, and Krainov (ADK) [16] is considered the most valid and is widely being used in the field of intense laser-matter interactions.

Once an electron is freed from an atom by an intense laser, it is accelerated by the oscillating electric field. Before escaping entirely, it may recollide with its parent ion [17]. This revisit of the electron may result in an excitation, may knock off one or more electrons from the parent ion causing multiple ionization or recombine with the parent ion and release energy gained by the field as high harmonic generation (HHG). The existence of this nonsequential ionization (NSI) in multielectron atomic systems subjected to intense laser fields has been observed experimentally [18, 19, 20]. The multielectron NSI process may increase the yield by several orders of magnitude compared to SI yield [20].

As the laser intensity increases, ionization dynamics evolved from single photon ionization to multiphoton to tunneling. To determine when this transition took place

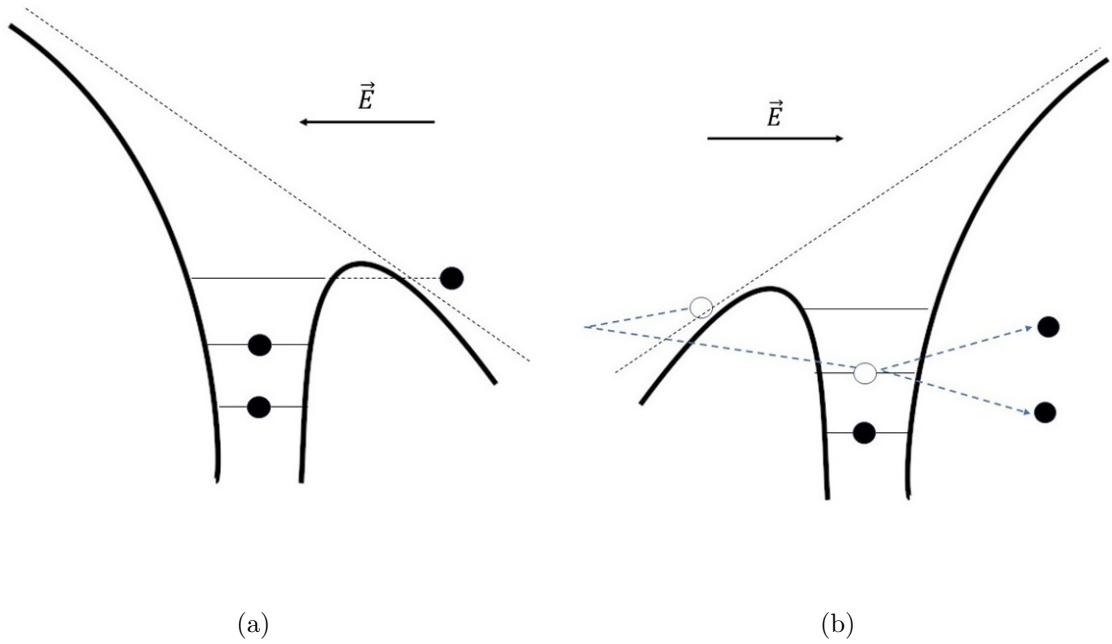

Figure 1.3: Schematic drawing of (a) initial ionization and then (b) recollide with its parent ion.

is essential, which is distinguished by Keldysh [21] parameter. In atomic units, the Keldysh parameter is defined as

$$\gamma = \sqrt{I_p/2U_p} \tag{1.12}$$

where I_p is the ionization potential of atoms, $U_p = E_0^2/4\omega^2$ is the ponderomotive energy, ω is the laser angular frequency, and E_0 is the electric field strength. Note that tunneling ionization will dominate if $\gamma < 1$, while multiphoton ionization prevails when $\gamma > 1$. A thorough understanding of atomic ionization in strong fields is essential for further explorations and diverse applications [22].

Worth mentioning is that the above ionization mechanisms neglect the influence of the laser magnetic field on the ionization processes, which is also known as the dipole approximation. It has also has been shown that the dipole approximation yields accurate values compared to a full classical electromagnetic laser field for intensities up to 10^{23} W/cm^2 [23]

1.4 The Ultrastrong Field and the Photoelectron Dynamics

Once the electron is released to the continuum, the properties of the radiation field primarily governed its dynamic. If an electron ionized in a 10^{19} W/cm^2 field is accelerated by an average field half of that in the peak intensity region of focus, by nonrelativistic kinetic equation $v = at$, its speed would surpass the speed of light c within a quarter cycle, which strongly suggests that it has entered the relativistic regime. Another way to look at the relativistic nature of such strong intensities is to utilize the expression of nonrelativistic pondermotive energy.

$$U_p = \frac{e^2 E_0^2}{4m_e\omega^2} \tag{1.13}$$

which exceeds the rest energy of an electron. Since $v/c \approx 1$ in this situation, the effect of the laser magnetic field $\vec{B}_{laser}$ is no longer negligible and deflects the electron in a direction perpendicular to its original path making the motion two dimensional. The magnetic field from the laser radiation field could significantly affect the re-scattering

dynamics and subsequent recombination by deflecting the returning electron away from its parent ion. We use the Lorentz deflection parameter [24] to gauge the transition of re-scattering dynamics from strong field to ultrastrong field, in atmoic units it is defined as,

$$\Gamma_R = \sqrt{\frac{U_p^3 I_p^3}{3c^2\omega}} \tag{1.14}$$

As the relativistic effects are in play for the atom-field interaction with the observed effects scaling roughly as $\exp[\Gamma_R]$, deflection becomes negligible when $\Gamma_R < 1$ and it plays an important role when $\Gamma_R > 1$.

1.5 Single Atom Response

In ultrastrong fields (10^{17} W/cm^2 to 10^{20} W/cm^2), an entire valence shell along with several inner shell electrons can be ionized [25]. Relativistic laser-matter interactions are mainly focusing on plasma physics and collective effects. A cogent description of the single atom response is vital to understand atomic clusters [26], high density targets [27], collision ionized electrons [28, 29], inner shell hole creation [30], radiation physics [31], and molecular physics [32] in comparable fields [33].

Low sample gas densities are used to limit space charges and ensure that the observed behavior is genuinely the response of a single atom. Plasma experiments usually operate in a regime where the interparticle separation distance is on the order of tens of nanometers [34]. The interparticle separation distance is well within the regime of the single atom response within the study of this dissertation, as shown in figure 1.4. There are only a few atoms at the center of the focus.

Experiments are limited to the spatial and temporal integration of the laser-matter response. The abundance of the signal generated from the low intensity region of the focus makes isolating the most intense interaction at the center of the focus difficult. Therefore, isolating the desired signal and reducing the background noise in order to extract any important information is one of the most critical tasks as well as one of the most challenging issues in ultrastrong laser-matter interaction experiments.

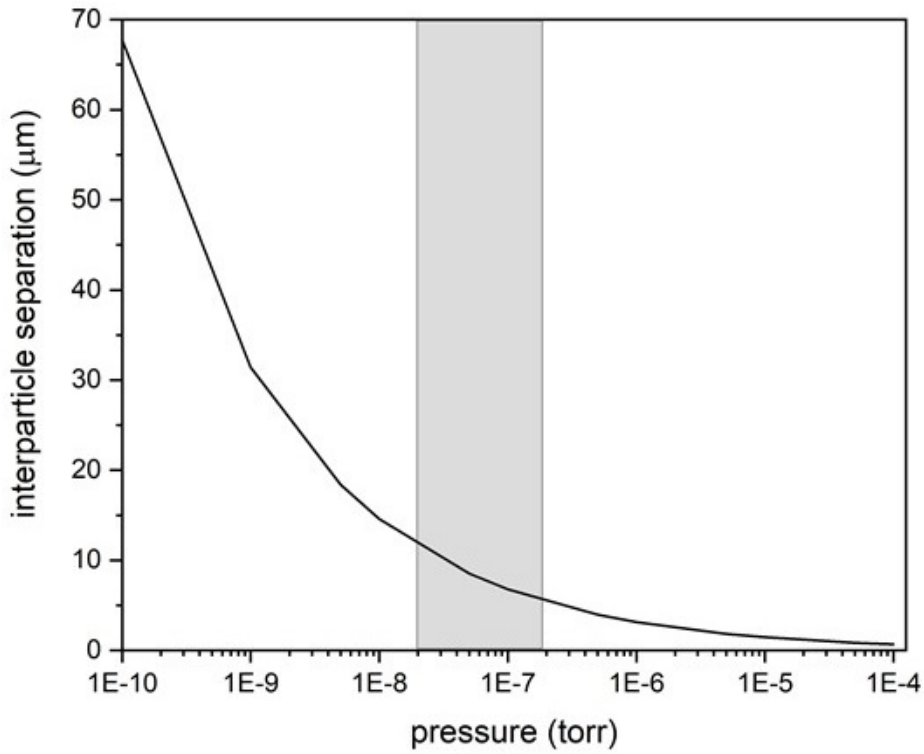

Figure 1.4: Interparticle separation distance as a function pressure. Shaded area represents the typical operating pressure during laser-matter experiments

1.6 Outline

The dissertation is organized as follows: Chapter 2 describes the laser system used to create ultraintense laser fields used in the experiments. Chapter 3 presents the design and fabrication of the home built photoelectron spectrometer used to measure products from ultraintense laser-matter interactions. Chapter 4 discusses the calibration of the spectrometer using various beta emission sources. Chapter 5 shows the laser ionization spectra collected by the spectrometer with atomic and molecular sample gas. Chapter 6 summarizes the results obtained in the dissertation, and also discusses the plans for some future experiments.

REFERENCES

[1] M. Klaiber, K. Z. Hatsagortsyan, J. Wu, S. S. Luo, P. Grugan, and B. C. Walker, "Limits of strong field rescattering in the relativistic regime," *Phys. Rev. Lett.*, vol. 118, p. 093001, Feb 2017.

[2] C. Spielmann, N. Burnett, S. Sartania, R. Koppitsch, M. Schnürer, C. Kan, M. Lenzner, P. Wobrauschek, and F. Krausz, "Generation of coherent x-rays in the water window using 5-femtosecond laser pulses," *Science*, vol. 278, no. 5338, pp. 661–664, 1997.

[3] M. Lewenstein, P. Balcou, M. Y. Ivanov, A. L'Huillier, and P. B. Corkum, "Theory of high-harmonic generation by low-frequency laser fields," *Phys. Rev. A*, vol. 49, pp. 2117–2132, Mar 1994.

[4] E. Liang, T. Clarke, A. Henderson, W. Fu, W. Lo, D. Taylor, P. Chaguine, S. Zhou, Y. Hua, X. Cen, *et al.*, "High e+/e- ratio dense pair creation with 10 21 w. cm- 2 laser irradiating solid targets," *Scientific Reports*, vol. 5, p. 13968, 2015.

[5] D. Giulietti, G. Boutoux, M. Aïche, G. Andrianaki, D. Batani, F. Burgy, M. Cipriani, F. Consoli, R. De Angelis, J. Ducret, *et al.*, "D+ d fusion reactions in 1018 w/cm2 intensity and repetitive laser-plasma interactions," *EPL (Europhysics Letters)*, vol. 119, no. 6, p. 65001, 2017.

[6] A. Di Piazza, C. Müller, K. Z. Hatsagortsyan, and C. H. Keitel, "Extremely high-intensity laser interactions with fundamental quantum systems," *Rev. Mod. Phys.*, vol. 84, pp. 1177–1228, Aug 2012.

[7] S. Gales, K. Tanaka, D. Balabanski, F. Negoita, D. Stutman, O. Tesileanu, C. Ur, D. Ursescu, I. Andrei, S. Ataman, *et al.*, "The extreme light infrastructure—nuclear physics (eli-np) facility: New horizons in physics with 10 pw ultra-intense lasers and 20 mev brilliant gamma beams," *Reports on Progress in Physics*, vol. 81, no. 9, p. 094301, 2018.

[8] W. Yan, C. Fruhling, G. Golovin, D. Haden, J. Luo, P. Zhang, B. Zhao, J. Zhang, C. Liu, M. Chen, *et al.*, "High-order multiphoton thomson scattering," *Nature Photonics*, vol. 11, no. 8, p. 514, 2017.

[9] A. E. Siegman, *Lasers*. Mill Valley, Calif.: University Science Books, 1986.

[10] M. Perry, O. Landen, A. Szöke, and E. Campbell, "Multiphoton ionization of the noble gases by an intense 10 14-w/cm 2 dye laser," *Physical Review A*, vol. 37, no. 3, p. 747, 1988.

[11] M. Ferray, A. L'Huillier, X. Li, L. Lompre, G. Mainfray, and C. Manus, "Multiple-harmonic conversion of 1064 nm radiation in rare gases," *Journal of Physics B: Atomic, Molecular and Optical Physics*, vol. 21, no. 3, p. L31, 1988.

[12] P. . M. Paul, E. Toma, P. Breger, G. Mullot, F. Augé, P. Balcou, H. Muller, and P. Agostini, "Observation of a train of attosecond pulses from high harmonic generation," *Science*, vol. 292, no. 5522, pp. 1689–1692, 2001.

[13] J. Itatani, J. Levesque, D. Zeidler, H. Niikura, H. Pépin, J.-C. Kieffer, P. B. Corkum, and D. M. Villeneuve, "Tomographic imaging of molecular orbitals," *Nature*, vol. 432, no. 7019, p. 867, 2004.

[14] V. Bonch-Bruevich, AM and Khodovoĭ, "Multiphoton processes," *Soviet Physics Uspekhi*, vol. 8, no. 1, p. 1, 1965.

[15] S. Augst, D. D. Meyerhofer, D. Strickland, and S.-L. Chin, "Laser ionization of noble gases by coulomb-barrier suppression," *JOSA B*, vol. 8, no. 4, pp. 858–867, 1991.

[16] M. Ammosov, N. Delone, V. Krainov, A. Perelomov, V. Popov, M. Terent'ev, G. L. Yudin, and M. Y. Ivanov, "Tunnel ionization of complex atoms and of atomic ions in an alternating electric field," *Sov. Phys. JETP*, vol. 64, no. 1191, p. 26, 1986.

[17] K. C. Kulander, J. Cooper, and K. J. Schafer, "Laser-assisted inelastic rescattering during above-threshold ionization," *Phys. Rev. A*, vol. 51, pp. 561–568, Jan 1995.

[18] D. N. Fittinghoff, P. R. Bolton, B. Chang, and K. C. Kulander, "Observation of nonsequential double ionization of helium with optical tunneling," *Physical review letters*, vol. 69, no. 18, p. 2642, 1992.

[19] B. Walker, E. Mevel, B. Yang, P. Breger, J.-P. Chambaret, A. Antonetti, L. F. DiMauro, and P. Agostini, "Double ionization in the perturbative and tunneling regimes," *Physical Review A*, vol. 48, no. 2, p. R894, 1993.

[20] B. Walker, B. Sheehy, L. F. DiMauro, P. Agostini, K. J. Schafer, and K. C. Kulander, "Precision measurement of strong field double ionization of helium," *Physical Review Letters*, vol. 73, no. 9, p. 1227, 1994.

[21] L. Keldysh *et al.*, "Ionization in the field of a strong electromagnetic wave," *Sov. Phys. JETP*, vol. 20, no. 5, pp. 1307–1314, 1965.

[22] M. Li, J.-W. Geng, H. Liu, Y. Deng, C. Wu, L.-Y. Peng, Q. Gong, and Y. Liu, "Classical-quantum correspondence for above-threshold ionization," *Phys. Rev. Lett.*, vol. 112, p. 113002, Mar 2014.

[23] P. D. Grugan, S. Luo, M. Videtto, C. Mancuso, and B. C. Walker, "Classical study of ultrastrong nonperturbative-field interactions with a one-electron atom: Validity of the dipole approximation for the bound-state interaction," *Phys. Rev. A*, vol. 85, p. 053407, May 2012.

[24] S. Palaniyappan, I. Ghebregziabher, A. DiChiara, J. MacDonald, and B. Walker, "Emergence from nonrelativistic strong-field rescattering to ultrastrong-field laser-atom physics: A semiclassical analysis," *Physical Review A*, vol. 74, no. 3, p. 033403, 2006.

[25] K. Yamakawa, Y. Akahane, Y. Fukuda, M. Aoyama, N. Inoue, H. Ueda, and T. Utsumi, "Many-electron dynamics of a xe atom in strong and superstrong laser fields," *Physical Review Letters*, vol. 92, no. 12, p. 123001, 2004.

[26] T. Ditmire, J. Tisch, E. Springate, M. Mason, N. Hay, J. Marangos, and M. Hutchinson, "High energy ion explosion of atomic clusters: Transition from molecular to plasma behavior," *Physical Review Letters*, vol. 78, no. 14, p. 2732, 1997.

[27] P. Norreys, M. Zepf, S. Moustaizis, A. Fews, J. Zhang, P. Lee, M. Bakarezos, C. Danson, A. Dyson, P. Gibbon, *et al.*, "Efficient extreme uv harmonics generated from picosecond laser pulse interactions with solid targets," *Physical review letters*, vol. 76, no. 11, p. 1832, 1996.

[28] A. Dorn, A. Kheifets, C. Schröter, B. Najjari, C. Höhr, R. Moshammer, and J. Ullrich, "Double ionization of helium by electron-impact: complete pictures of the four-body breakup dynamics," *Physical review letters*, vol. 86, no. 17, p. 3755, 2001.

[29] R. Moshammer, B. Feuerstein, D. Fischer, A. Dorn, C. Schröter, J. Deipenwisch, J. C. López-Urrutia, C. Höhr, P. Neumayer, J. Ullrich, *et al.*, "Non-sequential double ionization of ne in intense laser pulses: a coincidence experiment," *Optics express*, vol. 8, no. 7, pp. 358–367, 2001.

[30] A. Becker, F. Faisal, Y. Liang, S. Augst, Y. Beaudoin, M. Chaker, and S. Chin, "Laser-induced inner shell vacancies in doubly ionized argon," *Journal of Physics B: Atomic, Molecular and Optical Physics*, vol. 33, no. 15, p. L547, 2000.

[31] J. Peatross, C. Müller, K. Z. Hatsagortsyan, and C. H. Keitel, "Photoemission of a single-electron wave packet in a strong laser field," *Physical review letters*, vol. 100, no. 15, p. 153601, 2008.

[32] S. Palaniyappan, R. Mitchell, R. Sauer, I. Ghebregziabher, S. L. White, M. Decamp, and B. Walker, "Ionization of methane in strong and ultrastrong relativistic fields," *Physical review letters*, vol. 100, no. 18, p. 183001, 2008.

[33] A. D. DiChiara, I. Ghebregziabher, R. Sauer, J. Waesche, S. Palaniyappan, B. L. Wen, and B. C. Walker, "Relativistic mev photoelectrons from the single atom response of argon to a 10^{19}W/cm^2 laser field," *Phys. Rev. Lett.*, vol. 101, p. 173002, Oct 2008.

[34] W. Kruer, *The physics of laser plasma interactions.* CRC Press, 2018.

Chapter 2

ULTRAFAST TERAWATT LASER SYSTEM

2.1 Introduction

High power ultrafast lasers are widely used to study processes initiated by the interaction of light with matter. It is widely applied in experiments on photoexcitation of gaseous, solid, and even liquid media. One of the most critical advances in laser technology is the chirped pulse amplification (CPA) technique, introduced by Strickland and Mourou in 1985 [1]. Amplification of an ultrashort pulse can lead to uncontrollable high intensities in the amplifier, nonlinear effects, and disastrous damage to the laser cavity. The elemental concept behind the CPA technique is to stretch out an ultrashort pulse in the time domain before any amplification, therefore avoid such effects. The pulse is then compressed to its transform limited duration after the amplification. A schematic drawing of the CPA technique is shown in figure 2.1. Another extraordinarily significant breakthrough in the technology of ultrafast laser was achieved with the demonstration of the self-mode-lock Ti: sapphire laser in 1991 [2]. Since then, people obtained a dramatic reduction in achievable pulse duration [3, 4]. The self-mode-lock technique, together with the concept of CPA, has led to a considerable increase in peak power acquirable by laser systems [5].

Ultraintense fields are classified here as fields in the intensity range from 10^{17} to 10^{20} W/cm^2. To achieve these intensities, one is required not only to develop a highly stable laser system with well-controlled pulse characteristics in space and time but also to design an interaction region to provide high signal to noise ratio and high dynamic range.

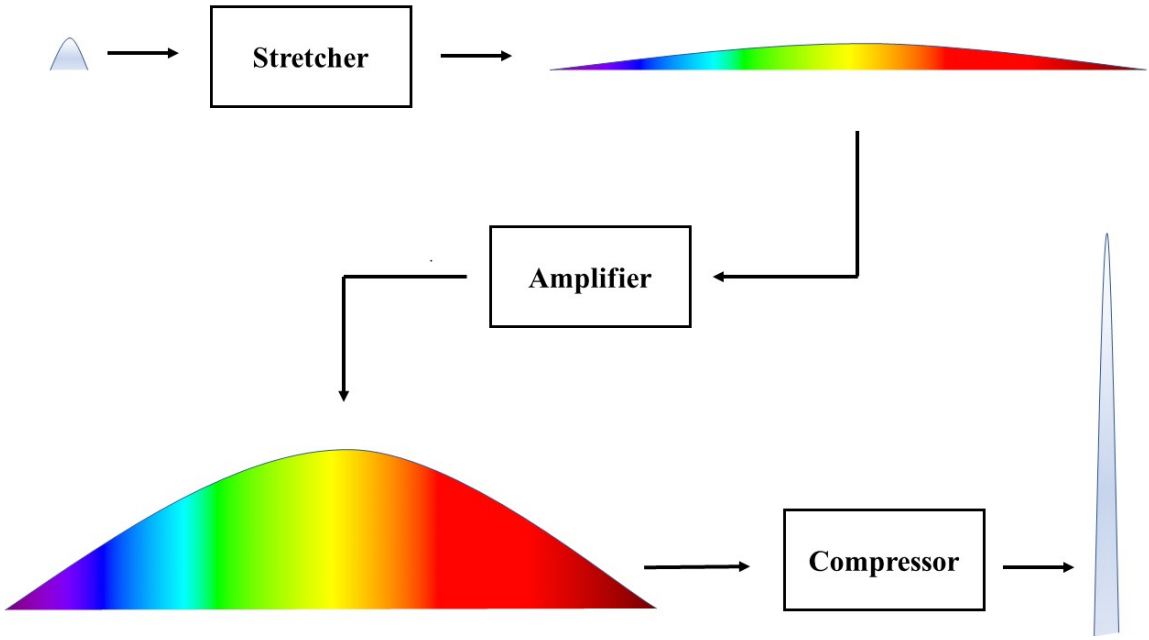

Figure 2.1: Schematic layout describing the chirped pulse amplification concept. Initial seed is typically stretched by a factor of 10^3–10^5 before amplification. Subsequent to amplification (gain $> 10^6$ or higher), the amplified pulse is compressed to its transform limited pulse duration using a pulse compressor.

2.2 Overview

The laser system used in this work is a home built chirped pulse amplification terawatt laser system. Mode-locked laser pulses of 76Mhz repetition rate, 150mW average power with a pulse duration of 25fs, are generated from a Ti: sapphire oscillator. In an optical stretcher, these pulses are stretched into 500ps. The stretched pulse train is then selected at a 10Hz repetition rate and sent into a regenerative amplifier, where the pulse energy is amplified into 5mJ/pulse. The output pulses are then delivered to a multipass amplifier where the pulses are further amplified into 250mJ/pulse. Eventually, the laser pulses are sent to a compressor, where the pulse duration is compressed into 40fs full-width at half-maximum (FWHM). We show a schematic drawing of the laser system in figure 2.2.

2.3 Ti:sapphire Oscillator

The core of the entire laser system is the Kerr-lens mode-locked oscillator. We use a Brewster-cut, 2.2 mm long Ti: sapphire crystal as the large-bandwidth [6] laser gain medium that is continuously pumped by an intra-cavity doubled, diode pumped 532 nm laser. To realize mode-locking, we applied two Brewster-cut fused-silica prisms in the cavity as the primary mechanism for dispersion compensation [7, 8]. Furthermore, a vertical slit is inserted into the cavity at the position right in front of the output coupler [9]. The vertical slit provides high loss for the continuous wave (CW) mode but low loss for the mode-locked mode so that the laser cavity selects the mode-locked mode. We mount the vertical slit on a translation stage to provide the motion perpendicular to the cavity beam; thus, one can realize the fine adjustment of the slit position. At normal mode-locked operation, the slit is opened to 1mm in width. At 1.9 W pump power typical mode-locked power output is 160 $\pm$ 10 mW. As the spectral bandwidth out of the oscillator is a vital parameter, which at narrow limits affects the performance of the subsequent amplification stages, it is kept around 55 $\pm$ 5 nm FWHM with a center wavelength of 790 $\pm$ 10 nm.

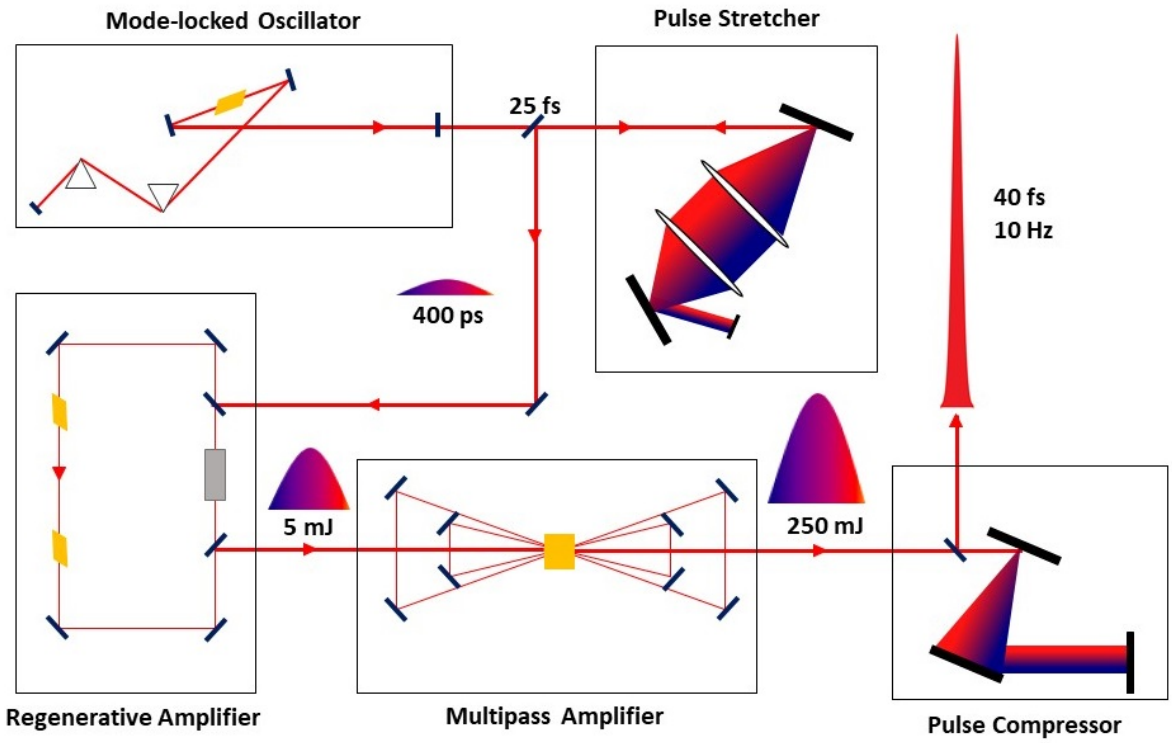

Figure 2.2: Schematic drawing of the self-mode-lock chirped pulse amplification Ti: sapphire laser system used in the dissertation study.

2.4 Pulse Stretcher

Amplification of ultrashort pulses must be performed with utmost caution as it can lead to permanent and catastrophic damage to laser gain medium and cavity optics in optical amplifiers. Stretch out the short pulse in the time domain is crucial for successful laser amplification. The stretcher consists of two 1200-grooves/mm gratings put in parallel, one 8-inch diameter concave mirror, two folding mirrors, and one retro-reflector. After the stretch, the seed pulses are stretched to 500ps FWHM with a stretching factor of roughly 20000 times. Such a sizeable stretching ratio enables the amplifiers to be operated well above the saturation fluence.

2.5 Regenerative Amplifier

The pulses of 76 MHz repetition rate from the oscillator are stretched in the time domain and are sent into a dual crystal regenerative amplifier. The regenerative amplifier is the first stage of the two-stage amplification. It selects pulses at a repetition rate of 10 Hz and amplifies each pulse to 8 mJ with a gain factor of 10^7. We employed low repetition rates since in high field experiments, the configuration of this kind is capable of delivering a large amount of energy per pulse while still maintaining low average power output. A ring-cavity configuration is used to maintain a high final beam quality. Two Brewster-cut, 10 mm long Ti: sapphire crystals are utilized as the gain medium and are differentially pumped by a 532 nm pump beam generated by an intra-cavity doubled, Q-switched, Nd: YAG laser operating at 10 Hz rate. After injection, the laser requires 16 to 18 round trips within the laser cavity while been amplified. Worth mentioning, energy before the main pulse is a severe concern when studying laser-matter interactions [10], in our operation, leakage pulse, have energy less than 1% of the main pulse. An electronic optic modulator, pockels cell is used to control the injection and the cavity dump. The final amplified energy after the regenerative amplifier is approximately 5.0 mJ/pulse, with a conversion efficiency of 30%.

2.6 Multipass Power Amplifier

If more power is desired, a multipass amplifier, which is the second and final stage of amplification, was employed after regenerative amplifier to reach the millijoule [11, 12] level with more energy from the pump lasers. Essentially, the amplified pulse from the regenerative amplifier now acts as a seed pulse for the multipass stage and crosses an anti-reflection (AR) coated 22 mm long Ti:sapphire gain medium five times while the crystal is being optically pumped by an intra-cavity doubled, Q-switched, Nd:YAG laser operating at 10 Hz rate. A micro-optic lenslet array is used to spatially filter the pump beam in order to improve the spatial mode and reliability of the final amplified beam. This technique minimizes the anomalies due to pump beam alignment distortions and changes in the pump laser. As a result, this multipass amplifier can amplify 6mJ pulses into 250mJ at a repetition rate of 10Hz. The green (532nm) energy conversion efficiency is roughly 30%.

2.7 Pulse Compressor

One must compress the final amplified pulse back down to the femtosecond (10^{-15} s) level to regain the optimum peak power. Due to material dispersion of the optical components and gain media used in amplifiers, the final pulse is much longer in the time domain than the initial pulse. Therefore, the final stage of the CPA technique always consists of an efficient pulse compressor

The compressor consists of two parallel gratings, 1500 lines/mm, and a retro-reflector in a double pass arrangement [13]. The gratings must be aligned to an accuracy of less than a milliradian to balance the group delay of the stretcher and amplification network. The compressor will provide 150mJ/pulse of compressed pulse energy. The final pulse duration measured using frequency-resolved optical gating (FROG) pulse measurement technique provides an FWHM temporal duration of 40fs. Based on these energy and temporal specifications, the peak power output of the laser is approximately four terawatts (4 TW).

2.8 Ultrashort Pulse Characterization and Diagnostics

Spatial chirp, namely the spatial dependence of spectral components of the laser beam at the transverse focal cross-section, is a very common and often undesirable distortion in ultrafast optics [14]. For achieving ultrashort pulse durations, we made a substantial amount of efforts to compensate not only the linear but also the nonlinear chirp components introduced by the stretcher–amplifier–compressor system. Proper focusing depends on both an excellent focusing optic and low spatial phase distortions, thus demanding both high-quality optical components and minimized nonlinear effects [15].

Temporal broadening, namely the deviation from the Fourier-transform-limited pulse duration, is the second pulse distortions associated with the CPA technique. This distortion comes from misalignment of components, the mismatch between the stretcher and the compressor, as well as achromatic and geometrical aberration in the optics [16]. Due to the extremely short duration, characterizing the ultrashort pulse temporal information is inherently a complicated process and requires specially developed meticulous techniques.

2.8.1 Spatial Profile Diagnose

One can characterize a laser beam by measuring its spatial intensity profile at points perpendicular to its direction of propagation. The spatial intensity profile is the variation of intensity as a function of distance from the center of the beam. The apparatus used in the diagnosing includes a long focal length (4m) focusing lens, a CCD camera mounted on a translation stage, and a serious of neutral density filters to properly attenuate the intensity of the laser beam to eliminate detector saturation and damage to the CCD camera. We transmitted signals from the CCD camera signal to a CRT monitor. The goal is essentially to reach the smallest possible spot size appear on the screen. We show a schematic drawing of the spot size measurements in figure 2.3.

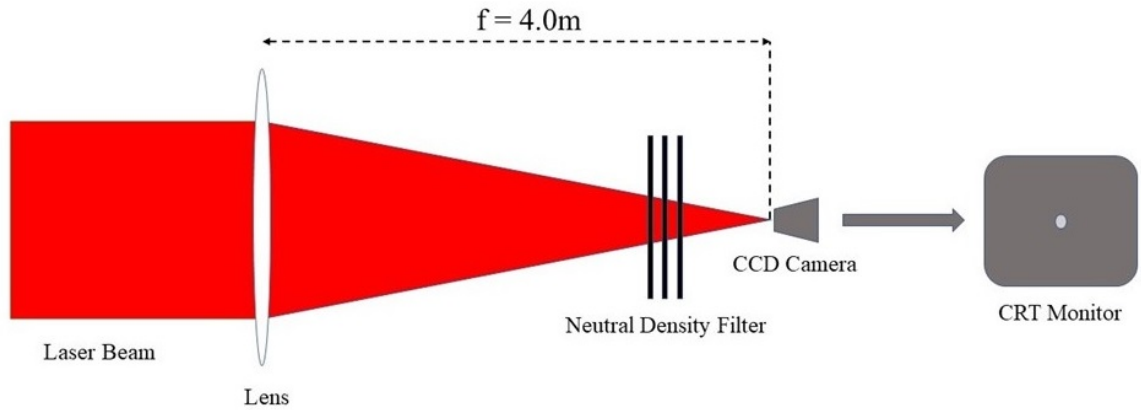

Figure 2.3: Schematic layout of the setup used to measure the laser spatial profile.

Using an index card (approximately 1" wide) to carefully block the center of the spectrum, where the laser beam is entirely spatially stretched, one can examine if the laser spot size is optimal. Typically, if two distinct spots appear on the screen after blocking, it suggests the compressor grating configuration is not parallel. Given such a situation, one of the compressor grating angles needs to be adjusted using the rotational actuator located underneath the grating until two spots perfectly overlap with each other.

2.8.2 Temporal Profile Diagnose

As the duration of the pulses shrinks in length, the difficulty in measuring it becomes increasingly significant. Measuring ultrafast optical events is not straightforward since the period of the wave is several orders of magnitude less than the fastest solid-state detector response times. Fortunately, over the past years, remarkable progress has occurred in the development of techniques for the measurement of ultrashort laser

pulses. One of which been utilized in our study is the most commonly used pulse-measurement method, frequency-resolved optical gating, FROG [17] and spectrally and temporally resolved upconversion technique, STRUT [18]. A schematic drawing for both setups is shown in figure 2.4.

When operating, in essence, pulses entering the FROG apparatus are first aligned by two irises (not shown in the figure). After alignment, the incident beam is split into two identical components by a beam splitter. One arm is delayed with respect to the other in time using a precision translation stage. Both beams are then focused inside a type II nonlinear BBO crystal, which acts as a second harmonic generator. The spectrometer then captures the signal of the second harmonic beam for a specific amount of time delays. The captured spectrogram is then processed using a pulse retrieval program to obtain pulse information such as pulse amplitude and spectral phase.

Though it can provide us with a complete characterization of ultrashort pulses, the FROG spectrogram is typically time-consuming. Therefore, we introduce the STRUT method to compensate and reduce the diagnosis time. The only difference between a FROG and a STRUT setup is the additional narrow-bandpass filter (800 ± 5nm) inserted to one of the arms. The STRUT provides a simple but reliable analysis of femtosecond pulses, the resulting spatiotemporal and spatiospectral image presents clear information about femtosecond pulses produced by either oscillators or amplifiers. [18]. Commonly, STRUT scans are followed by FROG scans to obtain complete pulse temporal and spectral information. The typical retrieved pulse duration of this laser is 40fs. Given that $\Delta\lambda = 40$nm ($\lambda_0 = 790$ nm) after amplification, the transform limit of such pulse is 23 fs. Compensating the remaining phase error could provide a 50% increase in the peak intensity. However, it is not practical to reach the transform limit due to the accumulated higher order (> 3) dispersion.

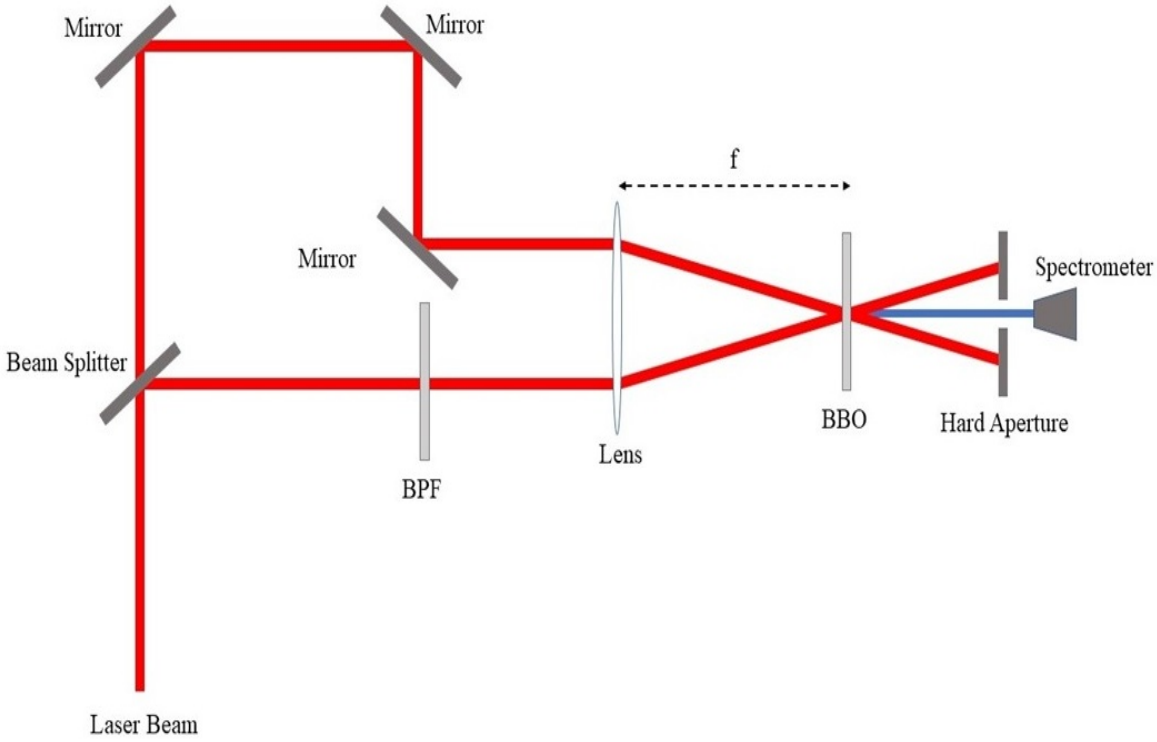

Figure 2.4: Schematic drawing of the FROG setup. BBO doubling crystal (BBO) is used to generate second order harmonic from the incident beam. The spectrometer is used to capture the spectrogram using a LabView program. The same setup can be used to perform STURT measurements by adding the narrow bandpass filter (BPF) in the reference arm.

REFERENCES

[1] P. Maine, D. Strickland, P. Bado, M. Pessot, and G. Mourou, "Generation of ultrahigh peak power pulses by chirped pulse amplification," *IEEE Journal of Quantum Electronics*, vol. 24, no. 2, pp. 398–403, 1988.

[2] D. E. Spence, P. N. Kean, and W. Sibbett, "60-fsec pulse generation from a self-mode-locked Ti:sapphire laser," *Optics Letters*, vol. 16, no. 1, pp. 42–44, 1991.

[3] L. Xu, C. Spielmann, F. Krausz, and R. Szipöcs, "Ultrabroadband ring oscillator for sub-10-fs pulse generation," *Optics Letters*, vol. 21, no. 16, pp. 1259–1261, 1996.

[4] I. Jung, F. Kärtner, N. Matuschek, D. Sutter, F. Morier-Genoud, G. Zhang, U. Keller, V. Scheuer, M. Tilsch, and T. Tschudi, "Self-starting 6.5-fs pulses from a Ti:sapphire laser," *Optics Letters*, vol. 22, no. 13, pp. 1009–1011, 1997.

[5] M. D. Perry and G. Mourou, "Terawatt to petawatt subpicosecond lasers," *Science*, vol. 264, no. 5161, pp. 917–924, 1994.

[6] M. Birnbaum and A. J. Pertica, "Laser material characteristics of ti:al2o3," *J. Opt. Soc. Am. B*, vol. 4, pp. 1434–1436, Sep 1987.

[7] R. Fork, O. Martinez, and J. Gordon, "Negative dispersion using pairs of prisms," *Optics Letters*, vol. 9, no. 5, pp. 150–152, 1984.

[8] C. Durfee, S. Backus, M. M. Murnane, and H. C. Kapteyn, "Design and implementation of a tw-class high-average power laser system," *IEEE Journal of Selected Topics in Quantum Electronics*, vol. 4, no. 2, pp. 395–406, 1998.

[9] D. Negus and C. Seaton, "Ease of use and versatility mark modelocked ti: sapphire design," *Laser Focus World*, vol. 28, no. 2, pp. 69–72, 1992.

[10] C. Ziener, G. Stobrawa, H. Schwoerer, I. Uschmann, and R. Sauerbrey, "Novel device for the generation of controlled prepulses in a Ti:Sapphire laser amplifier chain," *Review of Scientific Instruments*, vol. 71, no. 9, pp. 3313–3316, 2000.

[11] Q. Fu, F. Seier, S. Gayen, and R. Alfano, "High-average-power kilohertz-repetition-rate sub-100-fs Ti:sapphire amplifier system," *Optics Letters*, vol. 22, no. 10, pp. 712–714, 1997.

[12] Y. Nabekawa, Y. Kuramoto, T. Togashi, T. Sekikawa, and S. Watanabe, "Generation of 0.66-TW pulses at 1 kHz by a Ti:sapphire laser," *Optics Letters*, vol. 23, no. 17, pp. 1384–1386, 1998.

[13] J. Squier, C. P. Barty, F. Salin, C. Le Blanc, and S. Kane, "Use of mismatched grating pairs in chirped-pulse amplification systems," *Applied Optics*, vol. 37, no. 9, pp. 1638–1641, 1998.

[14] X. Gu, S. Akturk, and R. Trebino, "Spatial chirp in ultrafast optics," *Optics Communications*, vol. 242, no. 4-6, pp. 599–604, 2004.

[15] G. Pretzler, A. Kasper, and K. Witte, "Angular chirp and tilted light pulses in CPA lasers," *Applied Physics B*, vol. 70, no. 1, pp. 1–9, 2000.

[16] C. Fiorini, C. Sauteret, C. Rouyer, N. Blanchot, S. Seznec, and A. Migus, "Temporal aberrations due to misalignments of a stretcher-compressor system and compensation," *IEEE Journal of Quantum Electronics*, vol. 30, no. 7, pp. 1662–1670, 1994.

[17] R. Trebino, K. W. DeLong, D. N. Fittinghoff, J. N. Sweetser, M. A. Krumbügel, B. A. Richman, and D. J. Kane, "Measuring ultrashort laser pulses in the time-frequency domain using frequency-resolved optical gating," *Review of Scientific Instruments*, vol. 68, no. 9, pp. 3277–3295, 1997.

[18] J.-K. Rhee, T. S. Sosnowski, A.-C. Tien, and T. B. Norris, "Real-time dispersion analyzer of femtosecond laser pulses with use of a spectrally and temporally resolved upconversion technique," *JOSA B*, vol. 13, no. 8, pp. 1780–1785, 1996.

Chapter 3

MEV PHOTOELECTRON SPECTROMETER DESIGN

3.1 Introduction

Spectroscopy techniques such as time-of-flight (TOF), velocity map imaging (VMI) [1] and cold target recoil ion momentum spectroscopy [2] revolutionized measurements of laser-matter interactions. High peak power terawatt and petawatt laser systems [3, 4, 5] can create focus fields with intensities of 10^{21} W/cm^2. The current design target [6] for the highest intensity achievable is an ambitious 10^{24} W/cm^2. Such intensities have reached the ultrastrong limit [7]. Even for intensities at the strong-ultrastrong field boundary, approximately 1 a.u. of field, 3×10^{16} W/cm^2, traditional spectroscopy techniques struggle to accurately and reliably analyze photoelectrons and ions created by intense laser-matter interactions [5]. At the intensity of 10^{19} W/cm^2, the interaction of ultrastrong fields with atoms and molecules creates ions and electrons with energies up to 10^2 eV and 10^6 eV respectively [8]. Quantifying and analyzing such high energy products from ultrahigh intensity interactions requires a new generation of spectrometers [9, 10, 11, 12] and sample preparation [13]. At this time, a "breakthrough" technology for measuring the interactions of atoms and molecules in ultrastrong fields has not yet emerged.

Several issues shape the spectrometer design for ultrahigh laser intensities. First, atoms and molecules will experience multiple ionization processes and may even be stripped of all electrons to a bare nucleus. Being created across the laser focus volume, this can result in more than 10^5 photoelectrons from the background gases even with a high vacuum interaction region, which created difficulties in extracting any useful information. For this reason, ultraintense laser studies with atoms and molecules require ultrahigh vacuum (UHV) to reduce the amount of ionization from background gases.

Second, photoelectrons from background gas ions are overwhelmingly nonrelativistic and have energies in the 0 eV to 10 keV range. As a result, background photoelectrons can be excluded by a spectrometer having a 10^6 rejection for low energy electrons.

For laser intensities from 10^{17} W/cm^2 to 10^{20} W/cm^2, in the ultrahigh intensity region, photoelectron energies span from 20 keV to 2 MeV. TOF is no longer useful when photoelectrons have an energy greater than 100 keV, as the motion becomes relativistic, and photoelectrons possess a common speed near that of light. Large collection coincidence spectrometers [2], parabolic reflector collectors [14], and magnetic bottle spectrometers [15] are also unable to analyze high energy electrons, due to a combination of collection geometry and timing issues.

Ultraintense laser photoelectron spectroscopy is further complicated by electron emission into a wide range of angles [16]. Photoemission from the lower intensity, nonrelativistic laser interactions can be approximated as a dipole interaction where photoelectron emission is aligned with the plane perpendicular to laser propagation vector $\hat{k}$ and is typically peaked along the direction of $\hat{E}$. For a relativistic laser-matter interaction, the photoelectron may absorb millions of photons and, as a result, have a significant momentum along $\hat{k}$. The final direction and magnitude of the electron momentum $\hat{p}$ is an essential part of the physics behind the light-matter interactions and can fall within a large 2 π steradian solid angle centered on $\hat{k}$.

Electron spectrometers, such as the one presented here, are of the type that can be incorporated into high intensity laser beam lines with a vacuum follicle to isolate the ultrahigh vacuum (UHV) experimental interaction region from the vacuum of the laser system [17]. Relativistic high field atomic physics and MeV electron spectroscopy for ultrahigh intensity focused laser experiments are part of the science needed to support future experiments that require single particle sensitivity, angle, and energy resolved measurements with a very low event background. One may compare the described MeV spectrometer with current electron spectroscopy of keV to GeV energies that have been essential to the success of modern high energy density laser plasma science. These

high energy density spectrometers, which also use a magnetic field energy analyzer and scintillation detection, are optimized for the detection of many electrons in a collimated beam from a single laser shot. Several hundred pico-Coulombs of electron charges may be detected in a single shot within an electron divergence of order one milliradian [18]. The event rate/solid angle in such an experiment is 10^{14} higher than that resulting from the energy and angle resolved measurements of a single atom or molecule in an ultraintense laser focus.

We present a magnetic deflection spectrometer for ultrahigh intensity laser experiments in a focused geometry with atomic and molecular samples. The spectrometer provides the high dynamic range and low background event rate necessary for low sample density experiments that are free from Coulomb explosion. The kinetic energy (E_k) resolution (E_k at full-width-half-maximum, FWHM) of the spectrometer is variable over the range $0.05 < \Delta E_k/E_k < 0.4$. The spectrometer operates in UHV and utilizes a rotation stage in the vacuum for the magnet analyzer to select photoelectrons as a function of the emitted into the angle from the laser wave vector direction, $\hat{k}$.

3.2 Simulation

Building such a massive, complex magnetic deflection spectrometer requires careful design and planning. Prior to the fabrication process, a simulation of the photoelectrons trajectory was done to give us some insight into the dynamic of the photoelectron inside the chamber and to serve as a strong and powerful tool to help determine both the overall and details of the photoelectron spectrometer design.

In order to clarify the spatial coordinates associated with experimental photoelectron acquisition and to obtain a clear picture of the exit conditions of those photoelectrons, we defined a two-parameter coordinate system derived from spherical spatial coordinates, θ (polar) and ϕ (azimuthal), which is also the coordinate system used in the simulation. The polar angle is measured from the laser propagation direction $\hat{k}$. The azimuthal angle is measured from the laser electric field $\vec{E}_{laser}$. With this

coordinate setup, our electromagnetic analyzer will be in the $\hat{x}$ direction, and the detector assembly will be directly above the laser focus and in the $\hat{y}$ direction. A drawing of the coordinate system is shown in figure 3.1.

When charged particles move through the magnetic field, they experience direction change of velocity by interacting with the Lorentz force. We can interpret photoelectron energy selection as follows, assume a photoelectron with a rest mass m_0 and velocity v enters the magnetic field with a field magnitude B. If the electron deflects, towards the spatially fixed detector, by an angle α and the corresponding mean radius of curvature is R, using Newton's $2nd$ law and Lorentz force equation, we can show that,

$$F = m_0 \frac{v^2}{R} \tag{3.1}$$

$$evB = m_0 \frac{v^2}{R} \tag{3.2}$$

$$R = \frac{m_0 v}{eB} \tag{3.3}$$

R is also known as the Larmor radius or the radius of gyration. At relativistic velocities, namely when $v/c \approx 1$, term $m_0 v$ can be replaced by $\gamma m_0 v$ where γ is defined as

$$\gamma = \frac{1}{\sqrt{1 - \left(\frac{v}{c}\right)^2}} \tag{3.4}$$

γ is also know as the Lorenz factor and c is the speed of light in vacuum. The relativistic momentum p of a photoelectron is given by

$$p = \gamma m_0 v \tag{3.5}$$

and combine equation (3.4) and (3.5). we can obtain the velocity of the photoelectron

$$v = \sqrt{\frac{(p/m_0)^2}{(1 + \frac{(p/m_0)^2}{c^2})}} \tag{3.6}$$

The Lorentz force equation:

$$\vec{F} = q\vec{v} \times \vec{B} \tag{3.7}$$

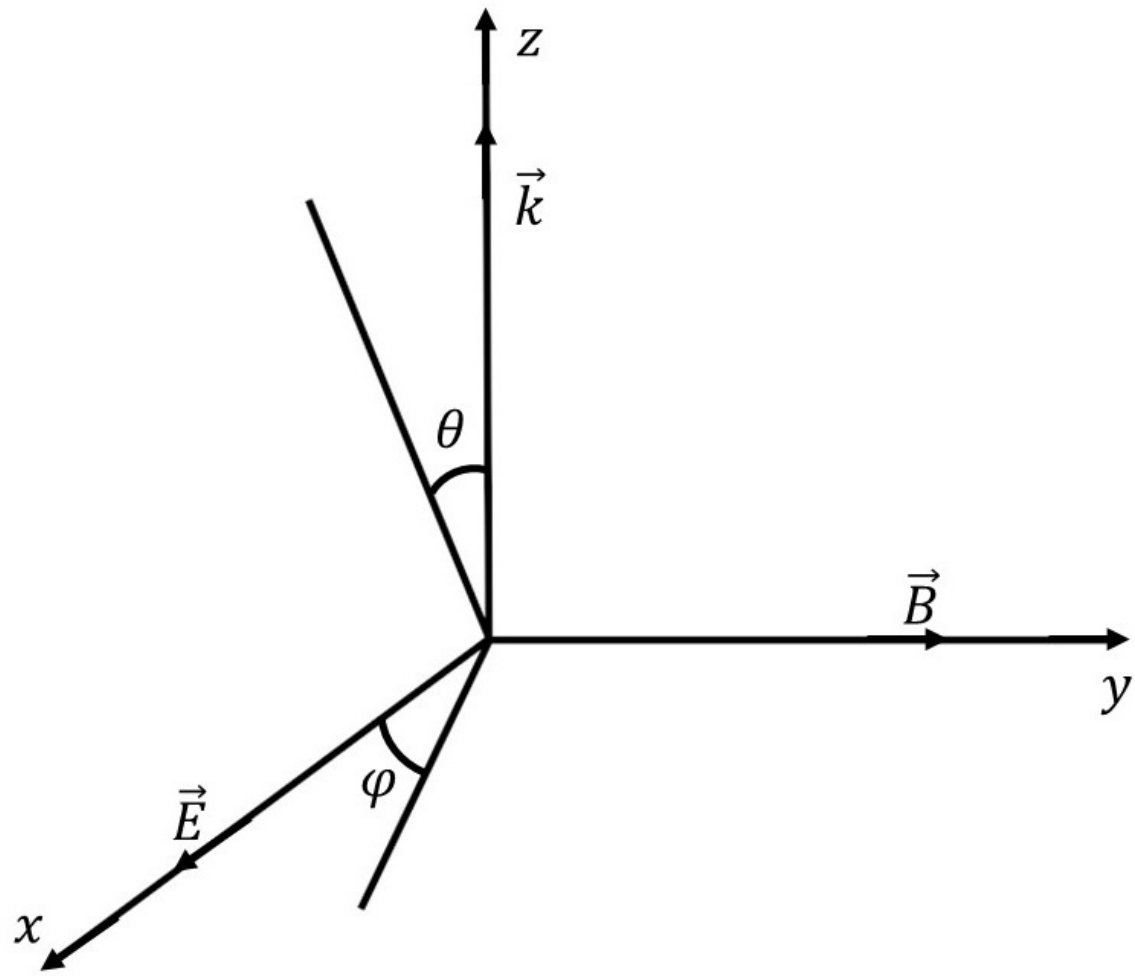

Figure 3.1: Two-parameter coordinate system used for photoelectron detection and characterization. We superimposed the origin of the coordinate system with the laser focus. The electromagnet analyzer is at $\hat{x}$ axis and the detection assembly is at $\hat{y}$ axis.

Newton's $2nd$ law of motion can also be written as

$$\vec{F} = \frac{d\vec{p}}{dt} \tag{3.8}$$

combine equation (3.7) and (3.8) we have

$$d\vec{p} = q\vec{v} \times \vec{B} \cdot dt \tag{3.9}$$

Here we employed time integration scheme to help us calculate the trajectory of the photoelectron. Therefore, equation (3.9) can be rewritten as,

$$\Delta\vec{p} = q\vec{v} \times \vec{B} \cdot \Delta t \tag{3.10}$$

we used equation (3.6) and (3.10) as the fundamental simulation equations of the magnetic deflection spectrometer. Essentially, the photoelectrons are given the initial position at the laser focal point, as well as initial momentum. The magnetic field generated by our electromagnet analyzer was considered constant over a small circular region; more detail of this approximation can be found in Section 3.4. The change of momentum was calculated for each time step, which is set at Δt = 10^{-10} s based on the geometry of the spectrometer. The change of position is also determined using equation (3.6) and

$$\Delta\vec{r} = \vec{v} \cdot \Delta t \tag{3.11}$$

Two termination or boundary conditions were used in the simulation, reaching either of the conditions will terminate the calculation and yield results. First is when the photoelectron position reached the height of the detector, while the other one is when the photoelectron has traveled the maximum time ($1 \times 10^{-7} s$). Once terminated, the final coordinates information of the photoelectron will be examined. If it is within the dimension of the detector, its trajectory will be plotted, and initial position and momentum will be recorded, otherwise, such information will be discarded. Figure 3.2 shows the flow chart of the simulation. Python source codes of this simulation are given in Appendix A.

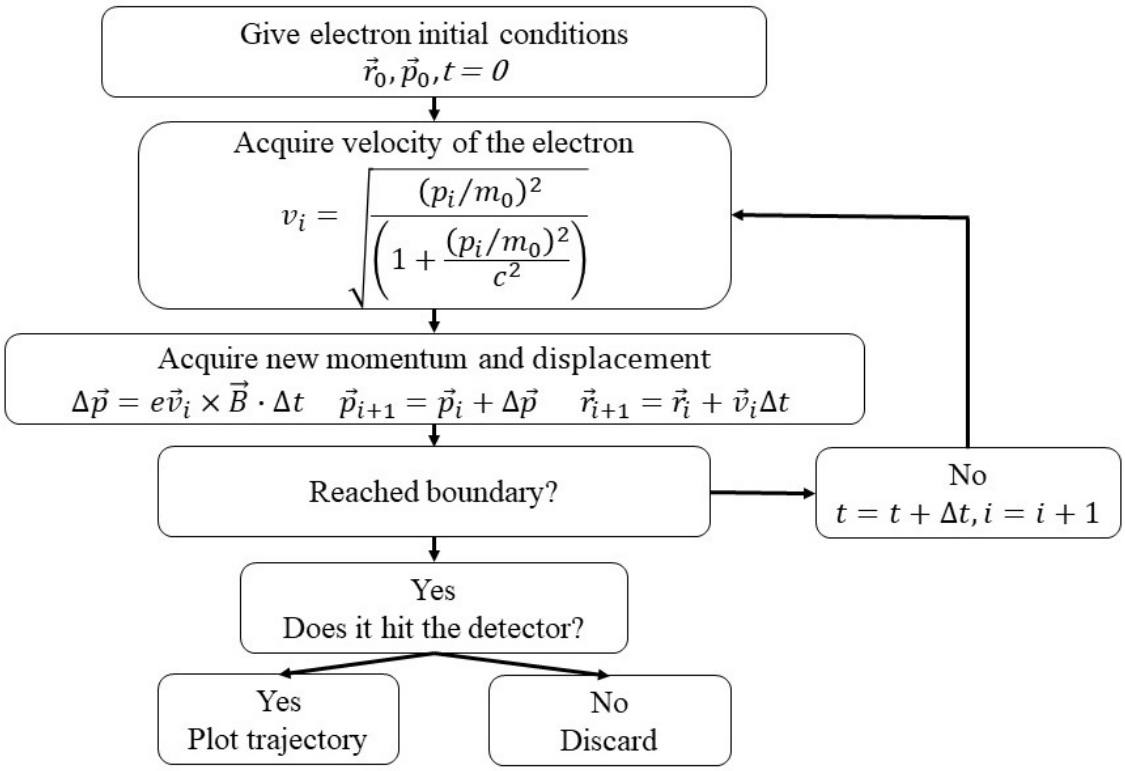

Figure 3.2: Flow chart of the time integration method used in the simulation to calculate the trajectory of the photoelectron generated from laser-matter interactions

3.3 Energy Resolution

The energy resolution of the photoelectron detection scheme is defined as the full-width of an energy peak at half-maximum (FWHM), ΔE_k, divided by the peak (mean) electron energy, E_k. The energy resolution, $\Delta E_k/E_k$ of the spectrometer, is an imperative performance parameter. It describes its ability to distinguish two nearby energy photoelectrons. In essence, ΔE_k will be displayed in the energy spectrum as a broadened peak. In our magnetic deflection spectrometer, this is due to the small difference in the Lamar radius for different electron energies as well as the integration time of all the electronics involves in the detection. Here we are going to employ the simulation created from the previous section to calculate the energy resolution.

We calculated the magnetic field that was capable of deflecting the photoelectron to the center of the detector, whose value is then fixed for the rest of the calculation. Afterward, we expand the energy of the photoelectrons both ways, with small step size, typically 25 keV, and examine the upper and lower limit of the photoelectron energies that were captured by the detector assembly, therefore reveal the energy resolution of the spectrometer. Worth mentioning, the initial momentum in the simulation were given a small angular dispersion with respect to the horizontal direction and toward the electromagnet analyzer, to simulate the angular acceptance of the spectrometer.

In this study, we explored two possible setups based on our UHV main chamber geometry and available materials, namely, a high resolution setup with a smaller diameter (3cm) scintillator plastic at a higher position (almost levels with the top large flange), and a low resolution setup with a larger diameter plastic (10cm) at a lower position (approximately 15 cm lower than the high resolution setup). Baffle slits have a 2° acceptance angle for both experiment setups. Example trajectories are shown in figure 3.3 for the low resolution setup.

A $\Delta E_k/E_k = 0.05$ is expected with 500 keV at the high resolution setup and $\Delta E_k/E_k = 0.4$ is expected at low resolution setup through simulations. Also, the resolution simulations are confirmed with a pure graphing method using AutoCAD. Peak transmission for the high resolution mode shown is calculated to be 80 %, while

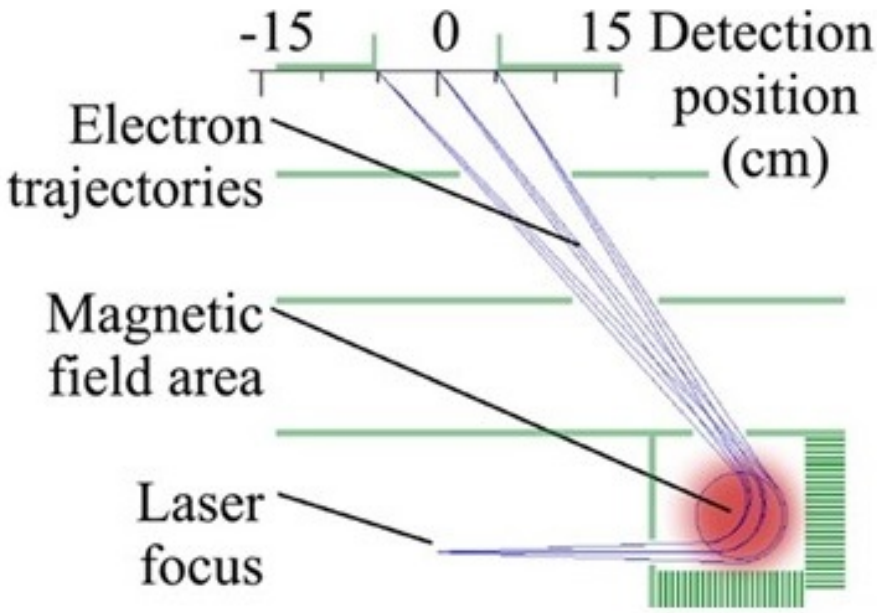

Figure 3.3: Example trajectories (blue lines) across the entrance slit and detector are shown with the magnetic field (red), which is directed out of the page. Baffles in the cross-section are shown by green lines for the entrance and exit slits and with a closely spaced line hatch where the electron and photon absorption baffles are placed around the magnet.

for a $\Delta E_k/E_k = 0.4$ mode, 100% of the electrons entering the spectrometer slit at the central energy are detected. The spectrometer geometry gives a detection solid angle that is limited by the gap between the electromagnet. The calculated resolution for both setups is shown in figure 3.4.

Furthermore, we did a calculation of the relativistic trajectories based on a peak field of 408 Gauss magnetic field generated by the electromagnet. By recording the final coordinates of photoelectrons with various energies (from 350 keV to 850 keV) at the height of the detector assembly. As anticipated, the calculation shows an explicit trade-off between energy resolution and the amount of signal, as shown in figure 3.5. Through this calculation, we were able to fine-tune the detector position as well as the angular acceptance. A sweet spot between the two critical parameters was achieved to give us a decent energy resolution while still maintaining a reasonable photoelectron signal capture rate.

According to the simulations results, low resolution setup was selected, due to the much higher signal rate, which is approximately an order of magnitude higher than the high resolution. To compensate for the reduced energy resolution, magnetic analyzer currents been measured were decided carefully to avoid any overlap in the energy spectrum.

3.4 Magnetic Deflection Spectrometer

The spectrometer primarily consists of an ultra-high vacuum (UHV) chamber used as an interaction chamber. It is made up of the following essential components: UHV interaction region, parabolic mirror focusing, effusive sample gas delivery, rotational magnetic deflection analyzer, baffle slits, and plastic scintillator/photomultiplier tube (PMT) or micro channel plate (MCP) detection assembly.

The UHV chamber is pumped using two turbomolecular pumps. One 300l/s and 500l/s primary turbomolecular pumps backed by a secondary 70l/s high conductance turbomolecular pump. The high conductance secondary turbomolecular pump is backed with a roughing pump, which does not need to be oil free for most experiments.

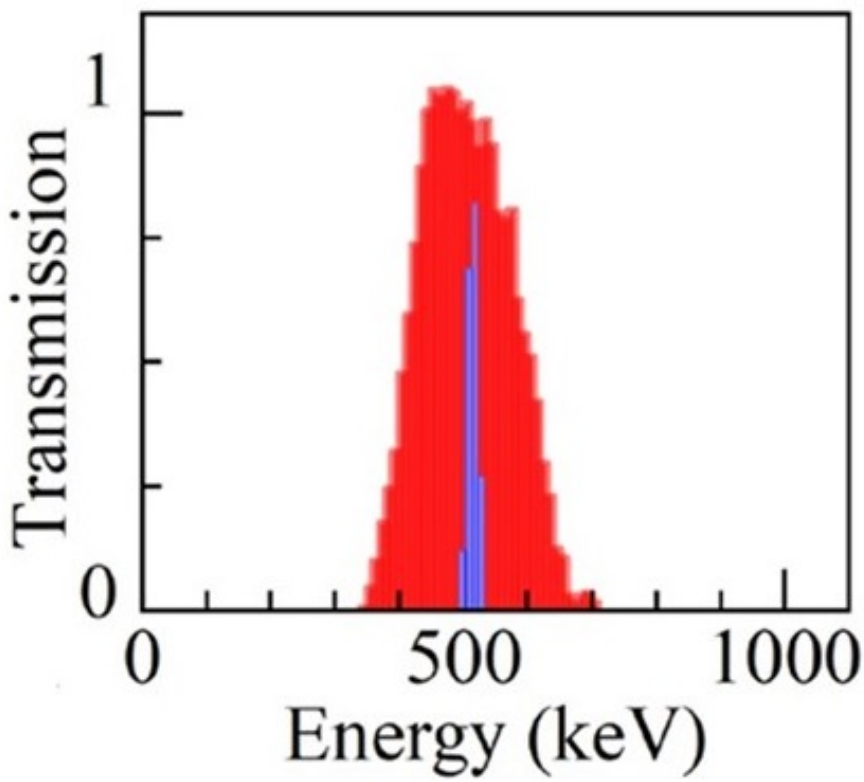

Figure 3.4: The calculated resolution $\Delta E_k/E_k = 0.05$ at 500 keV with a 2.1° slit, 3 cm scintillator, and detector position is given in blue. $\Delta E_k/E_k$ for a 2° slit and 10 cm diameter detector at the low position [which is 15 cm lower and roughly levels with the top large flange] is also shown in red.

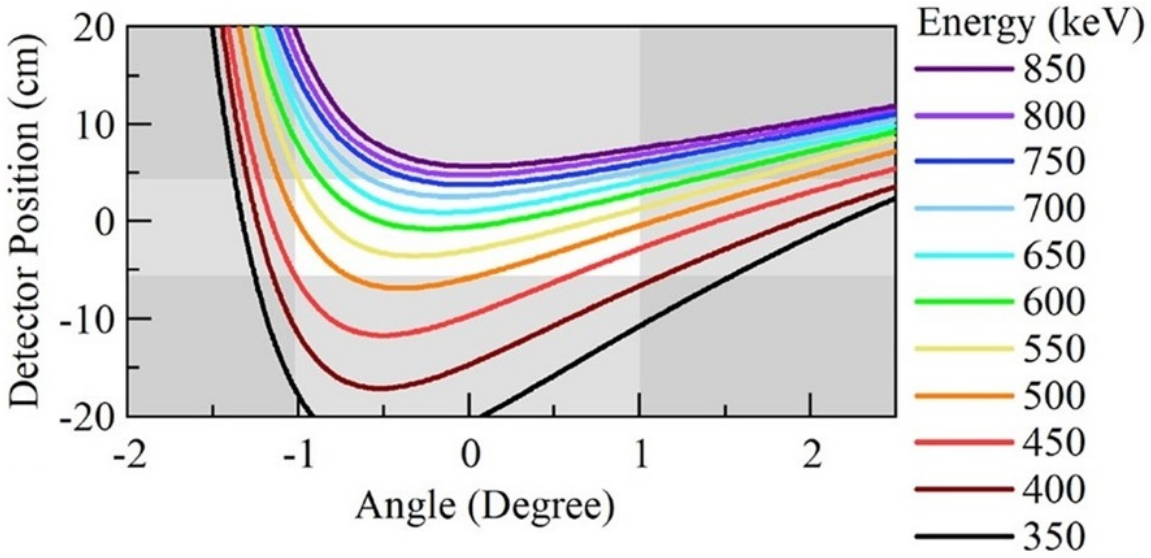

Figure 3.5: Relativistic trajectory calculations for a peak field of 408 G give the dispersion of the electron position at the detector as a function of E_k and emission angle from the laser focus to the analyzer slit. Electrons excluded by a $\pm$ 1° entrance slit and 10 cm detector are the highlighted area in the center.

Ultimate pressures of $\sim 10^{-9}$ Torr are achieved after a 70^oC bakeout. Bakeout are realized by using several mineral wool pads to create a heat insulation cubic and heat up by using four stove heating elements connected to 4 variable transformers. Temperature is controlled by varying the voltage output from those variable transformers. After 48 hours of baking and the subsequent cooling down to room temperature, the ultimate minimum pressure is achieved at typically 2×10^{-9} Torr. The plastic scintillator softening point limits the bakeout temperature.

We send high purity sample gas at room temperature into the ultrahigh vacuum chamber through a gas manifold. The inlet leak valve controls the pressure, and the real-time pressure is monitored by using a hot-filament ionization gauge. Based on the sample species and laser intensity, a typical pressure range of the sample gas into the interaction chamber is varied from 1.0×10^{-8} Torr to 1.0×10^{-7} Torr. At the interaction region, a skimmed, effusive beam of atom/molecules across the laser at 90 degrees. Generated photoelectrons are emitting with a large 2π steradian solid angle centered on $\hat{k}$. Those electrons that entered the gap between the two electromagnets will be deflected and eventually reach the detection assembly. Figure 3.6 provides both the top and side view of the chamber.

3.4.1 Laser Focus

The laser beam enters the interaction chamber through a near-infrared (N-IR) anti-reflection coated 0.25" thick fused silica entrance window. Prior to entering the chamber, the beam was carefully aligned using two irises to guarantee a straight and level beam path. A 5m long black coated beam tube (not shown in the figure) is also used to significantly reduce the disturbance from airflow along the beam path before it enters the chamber. The incident beam is focused using a 3" diameter (f/2) gold-coated 60° off-axis parabolic mirror to obtain a near diffraction limited focus. The following two steps obtain the best possible focal point size. First, a rough alignment is done by optimizing the air breakdown of the focal point inside the chamber, which typically is sufficient for a regular alignment. A telescope and a CCD camera combination

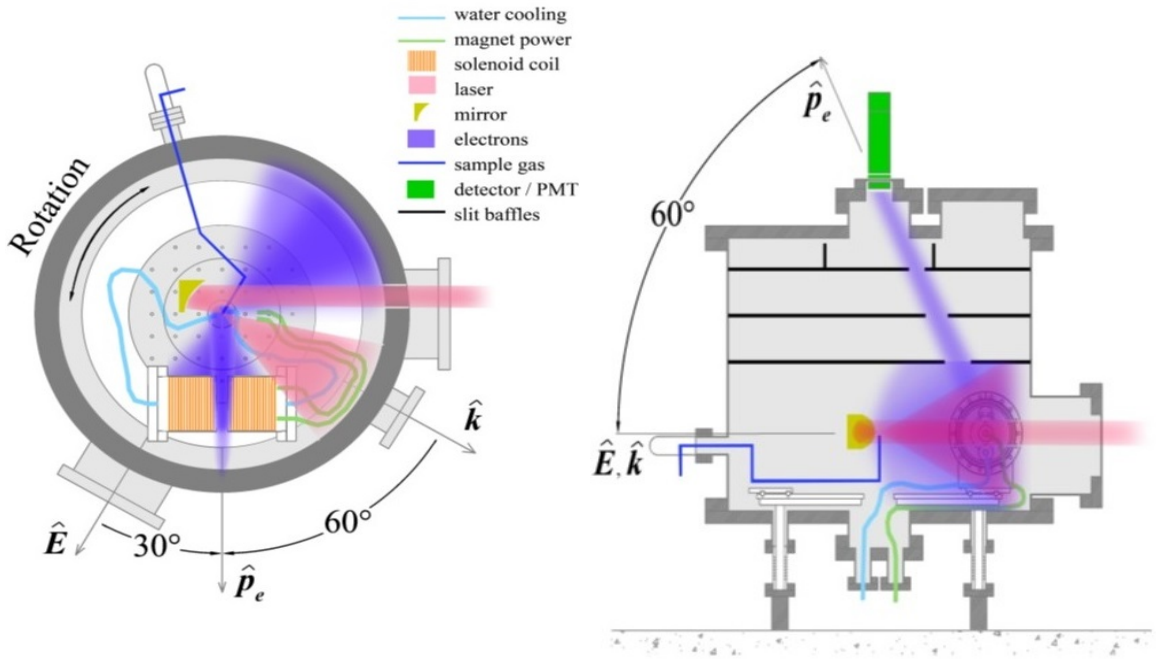

(a) (b)

Figure 3.6: Top (a) and side (b) views of the main chamber. Water cooling, magnet power, magnet coils, laser beam, parabolic mirror, sample gas delivery line, baffles, and scintillator/photomultiplier tube detector are indicated. Photoelectrons are indicated with shading.

detecting the laser focus can be used if a better alignment is desired. A series of neutral density filters must be applied to avoid detector saturation, the signal generated by the CCD camera will be monitored using a CRT screen, while alignment is realized by obtaining the smallest spot size appear on the screen. The use of a reflective parabolic optic provides a threefold advantage over refractive spherical optics by eliminating chromatic and spherical aberrations and facilitating and unobstructed propagation for the incident laser beam. The mirror is mounted on a two tilt controller (vertical and horizontal) to align the mirror with respect to the beam propagation axis. The mirror is also precisely aligned in the $\hat{x}$, $\hat{z}$ direction to place the focal point right at the center of the main UHV chamber; the height is also carefully adjusted, so the separation between the laser focus and the gas jet is within 2mm.

3.4.2 Rotational Magnetic Deflection Analyzer

We use a rotational magnetic deflection electron spectrometer to acquire angle and energy resolved photoelectrons generated through ultra-intense laser-matter interactions. It consists of three fundamental components, a rotational analyzer, a set of electromagnets, and the detector assembly. Photoelectrons generated from ultra-intense laser-matter interactions are angle resolve through the rotational analyzer and energy resolved by the electromagnet and deflected towards the detection assembly. Every step mentioned above though can be described with a couple of simple sentences but requires a substantial amount of planning, testing, building, rebuilding, and tweaking. The following sections will introduce all of the processes of design and fabrication.

3.4.2.1 Design Considerations in Photoelectron Detection

Energies of the photoelectrons created by ultra-intense laser-mater interactions can go up to several mega electron volts. Traditional spectroscopy techniques are unable to reliably and accurately measure and analyze such high energy electrons. The

goal is to design and fabricate a photoelectron spectrometer for ultrahigh intensity laser interactions with atoms and molecules in the single atom/molecule limit.

3.4.2.2 Rotational Analyzer

One of the most essential features of the spectrometer is its ability to spatially (θ) resolve photoelectron generated at the interaction region. With a range of motion from 5° to 100° with respect to the direction of laser propagation vector $\hat{k}$. Such operation is realized with a turntable assembly and a custom gear set connected to a UHV rotational feedthrough.

The turn table assembly consists of three layers. A side view and top view are provided in figure 3.7. The bottom layer is a breadboard that acts as the foundation of the entire turntable assembly. Built with multiple evenly spaced 1/4" 20 taped screw holes, it is capable of supporting a great deal of weight reliably. The breadboard is directly attached to the bottom of the chamber using six 1" diameter stainless posts. The middle layer and the top layer has an identical ring shape with a diameter of 0.6 m. Both layers have a pair of identical V grooves channel carved. Multitudinous stainless ball bearings are filled in both grooves to support the top layer. The outside of the top layer has gear teeth cut into it, which are coupled with the custom made gear set (not shown in the figure) with a 10:1 reduction ratio. The whole gear set is controlled by a shaft attached to a rotational feedthrough, which can be accessed from outside of the chamber, therefore making it possible to control the rotation of the magnetic analyzer without interfering with the ultra-high vacuum. Rotation of the turntable allows the analysis of photoelectrons emitted into angles from 5° to 100° off $\hat{k}$ vector of the laser beam. Photoelectron emission at all angles from $\hat{E}$ and perpendicular to $\hat{k}$ is fully accessible using a zero-order half-wave plate to rotate $\hat{E}$ just before the parabolic mirror.

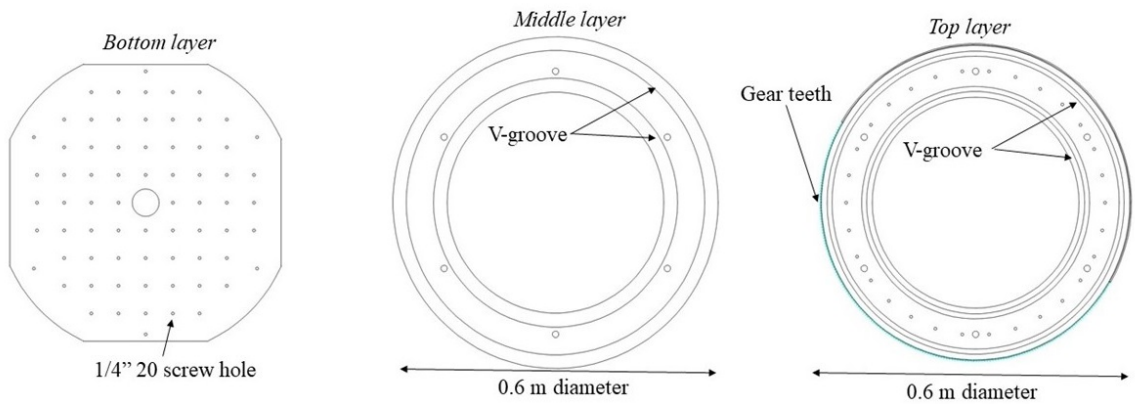

(a)

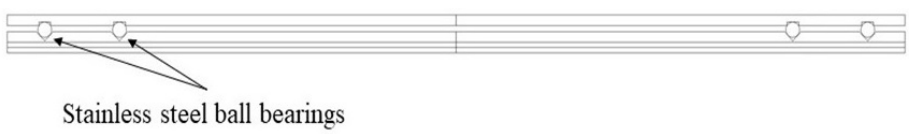

(b)

Figure 3.7: Top (a) and side (b) views of the three layers of turn table assembly. Stainless ball bearings are been put inside the v-groove to support the top layer. Gear teeth are cut into the outside of the top layer to couple to the custom made gear set (not shown in the figure) with a 10:1 reduction ratio.

3.4.3 Electromagnet

3.4.3.1 Electromagnet Overview

The electromagnets we custom-built to use in this spectrometer consists of two identical solenoids. Each of them has 9 layers of 14 gauge polyimide insulation wire. Each solenoid is 100mm long and has a 63.5mm long iron core to enhance the magnetic field and 530 winding from 90mm inner diameter to 120mm outer diameter. Both solenoids are housed inside two identical UHV confalt cans. Small UHV feedthrough provides power and water cooling to the coil housing, therefore grant the assembly UHV compatibility. Each coil can be energized with 12 A and has a resistance of 1.2 Ω. The separation gap between the two coils is 2.5 cm. An exploded, and 3-D crosssection view drawing of one of the electromagnets is shown in figure 3.8. Both UHV cans are placing horizontally and facing each other. A pair of identical aluminum brackets are used to support the cans on top of the turntable. In order to guarantee both electromagnets are sharing the same horizontal axis, the supporting brackets are carefully crafted and measured to assure same dimensions, three 0.5 inch aluminum shafts with the same length that attach to both conflat cans were also utilized to enhance the alignment, as well as establish additional stability. This carefully put-together configuration typically provides a uniform axial magnetic field on the radial (vertical) plane in the gap between the two electromagnets.

3.4.3.2 Magnet Wire

Being placed inside a UHV environment, inspections, and repairs of the electromagnet coil require a significant amount of time and effort. Therefore, as the most fundamental component of the coil, magnet wire needs to be able to sustain a relatively high temperature for an extended time, especially during the high energy electrons collections, which could take up to several hours. Besides, strong chemical resistance is critical since corrosion and contamination will occur inevitably, even with extraordinary effort been put in to keep the cooling water clean. Having superior chemical

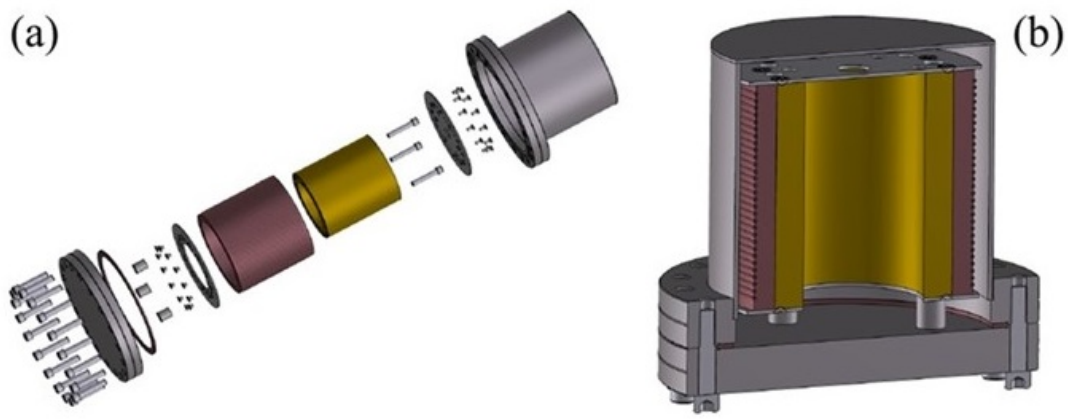

Figure 3.8: Exploded view (a) and 3D cross-sectional view (b) of the magnet assembly. Water cooling and magnet current are delivered by UHV feedthroughs (not shown) through the bottom conflat flange.

resistance could significantly increase the reliability and longevity of the electromagnet. Polyimide insulation was chosen for its exceptional thermal stability, phenomenal physical abrasion resistance, and unsurpassed chemical resistance. Its thermal stability is shown in figure 3.9 [19].

Even with the utterly reliable choice of magnet wire, connections between the UHV electric feedthrough and the solenoid magnet wire are still prone to having an electrical breakdown. Silicon sealant was used in between the solder point of the magnet wire and the UHV electric feedthrough. Furthermore, to avoid potential abrasion damage between the solenoid and the magnet wire, additional layers of plastic were placed in between the magnet wire and the solenoid. With all the insulation approach, the final resistance between the electromagnet assembly to the ground is kept well beyond 100kΩ level.

Selecting the gauge of the magnet wire is another important aspect of the design. With a fixed dimension of the solenoid and fixed maximum power output from the power supply. The choices of the wire gauge will determine the total resistance, the maximum magnetic field, and the heat generation. If we consider the simplest case, the magnetic field generated by an ideal solenoid at the center of the coil is given by Ampere's law:

$$B = \mu n I \tag{3.12}$$

Here μ is the permeability of vacuum, n is the density of the magnet wire, and I is the current. Therefore, by finding the average density of the different gauge wire, as well as the maximum current possible with the DC power supply, the maximum magnetic field can be attained with a certain wire gauge. Though the solenoid here is certainly not ideal, this approximation still holds since the real magnetic field generated by the electromagnets have a positive correlation to the result obtained from the calculation.

Since the choice of the gauges of wire is rather limited due to the production (typically only even number gauge wire are available), calculations are rather trivial. Python source codes of the calculation can be found in Appendix A. Gauge 14 wire was selected; the measured resistance of each coil at room temperature is $1.2 \pm 0.1\ \Omega$.

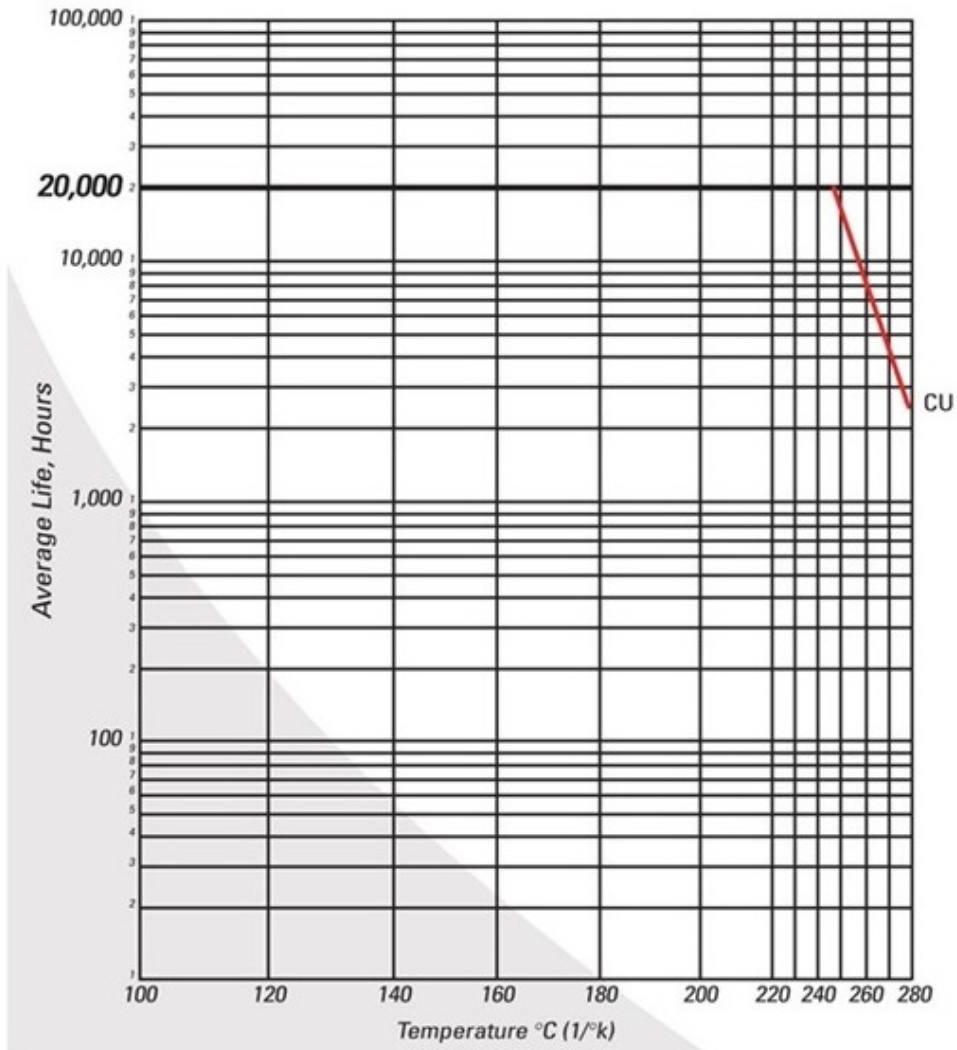

Figure 3.9: The average life of the heavy build polyimide insulation wire used in the experiment. The typical wire temperature during operation is 70°C.

3.4.3.3 Cooling and Powering

The electromagnets are powered using two HP/Agilent 6264B variable DC power supplies. Each of them is capable of delivering a maximum of 24V and 24A. They are connected in a "master-slave" parallel configuration with a total current output of 48A, the total voltage output of 24V, and the total power output of 1152W. The parallel configuration also provides better performance at high current by eliminating power supply overloads.

Cooling and powering become particularly complicated as the whole electromagnet assembly needs to operate with ultra-high vacuum compatibility. We went through a substantial amount of testing and building to find the proper solution. First of all, two electrical feedthroughs and two liquid feedthroughs are placed on the conflat flange, as stated previously. Traditional wire insulation is not an option as they will outgas and contaminate the UHV chamber, therefore prevent the chamber from reaching the ultimate pressure and creating unwanted background noise during laser-matter interactions. Such an issue was resolved by using bare copper wire then wrap the wire around with a series of ceramic beads as the insulation layer.

The other key concern associated with the electromagnet is the ohmic heating caused by the resistance of the copper wire. During continuous operation, even at relatively low currents, the thermal load is sufficient enough to heat the copper wire. Though from the previous discussions, we have learned that the magnet wire has exceptional heat resistance, it is the change of resistance (Ω) introduced by the variation of temperature that concerns. Resistance change leads to the changes of current going through the electromagnet and ultimately alters the magnetic field. Once it takes place during a data collection, can significantly reduce the reliability and accuracy of the measurement. Therefore, it makes cooling the magnet wire a critical component to a successful experiment. Air cooling is not applicable in this configuration. Therefore, we used a circulating chilled liquid cooling loop to reduce the thermal load on the electromagnet by removing excessive heat from the wire. Two different types of liquid coolant were tested, mineral oil and water. Mineral oil was utilized for its excellent

electrical insulation properties. The result is somewhat disappointing as though it delivered superb electrical insulation, mineral oil did not perform well enough in thermal transferring, and the complication it brings when cleaning and refreshing the coolant is significant. The final liquid cooling agent we used is water. Though it did not provide as good electrical insulation as mineral oil, excellent thermal performance is observed during testing, the clean and refresh process is also rather straightforward. The cooling water line is connected in series between two UHV cans. To accommodate the rotational analyzer design, we have employed flexible stainless steel bellow to delivery cooling water. To assure efficient and thorough cooling on both electromagnets, the position of the UHV liquid feedthroughs is carefully placed so the outlet would always be on the top position, and the inlet would always be at the bottom position thus the cooling water will always emerge the whole solenoid before exiting.

3.4.3.4 Magnetic Field

To characterize the field generated by the electromagnet, we measured the axial magnetic fields as a function of the axial distance. Measurements were made using a magnetic field sensor capable of measuring fields up to 30000 Gauss with a $\pm 2\%$ resolution. The magnetic probe is attached to a translation stage to take precise measurements of the distance. Figure 3.10 shows the results when we put the magnetic probe at the center of the gap while running 1.25 A on each coil with a super Gaussian fit. The measurements indicate a rather uniform magnetic strength within the circle having a diameter of approximately 6 cm, such magnetic field can be approximated to a constant field with a magnitude of its center value, in the simulation we used the same approximation, hence, make it easy to determine the kinetic energy of the electron reaching the detection assembly. Also, we noticed a sharp drop off in terms of the magnetic field strength outside the dimension mentioned above. The measurements indicate an "edge to center" ratio better than two orders of magnitude. Such characteristic assures minimum extra magnetic field to disturb the trajectory of desired photoelectrons.

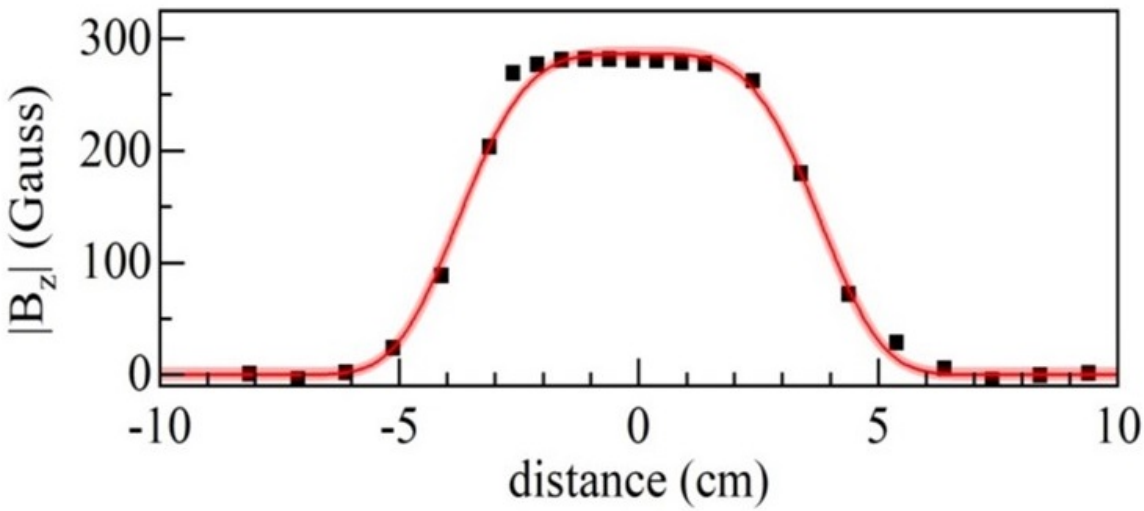

Figure 3.10: Analyzer magnetic field as a function of distance, s, from the magnet center while running 1.25 A on each coil.

A measurement of the voltage supplied to the electromagnet and the magnetic field generated is shown in figure 3.11, then we use the measured magnetic data in the simulation, a mapping between the energies of the photoelectrons that reach the center of the detection assembly and the voltage was created, as shown in figure 3.12.

One major disadvantage of such electromagnets is the magnetic hysteresis effect. Magnetic hysteresis occurs when one applies an external magnetic field to a ferromagnetic material, such as the iron core in our electromagnet, and the atomic dipoles align themselves with it. Even after removing the field, part of the alignment will be retained. Once magnetized, the magnet will stay magnetized indefinitely. To demagnetize it requires heat or a magnetic field in the opposite direction. In our case, the residual field caused by the hysteresis is measured to be roughly 20 Gauss after applied a current more than 20 minutes. If left unattended, this residual field will cause significant error in terms of energy calibration, especially during lower energy photoelectron acquisitions. We primarily used two different methods to resolve this issue. First, after each collection, the electromagnet is connected to the DC power supply with reversed polarity, thus creating a negative field to achieve demagnetize. Second, a variable alternating current source is connected to the electromagnet if a long (> 60 min) gap between collection is planned. One can typically reduce the residual field to less than 5 Gauss after performing such procedures.

3.4.4 Photoelectron Detection Technique

3.4.4.1 Scintillator and Photo Multiplier Tube

The final stage of the photoelectron acquisition process is the detection stage, where those angle and energy resolved photoelectrons are captured and analyzed. To be able to measure and analyze photoelectrons produced in ultra-intense laser-matter interactions accurately is the design goal for this spectrometer. Experiments conducted in this spectrometer include photoelectrons energies up to mega-electron volts. Therefore, in this experiment, the primary detection technique is a scintillator coupled with

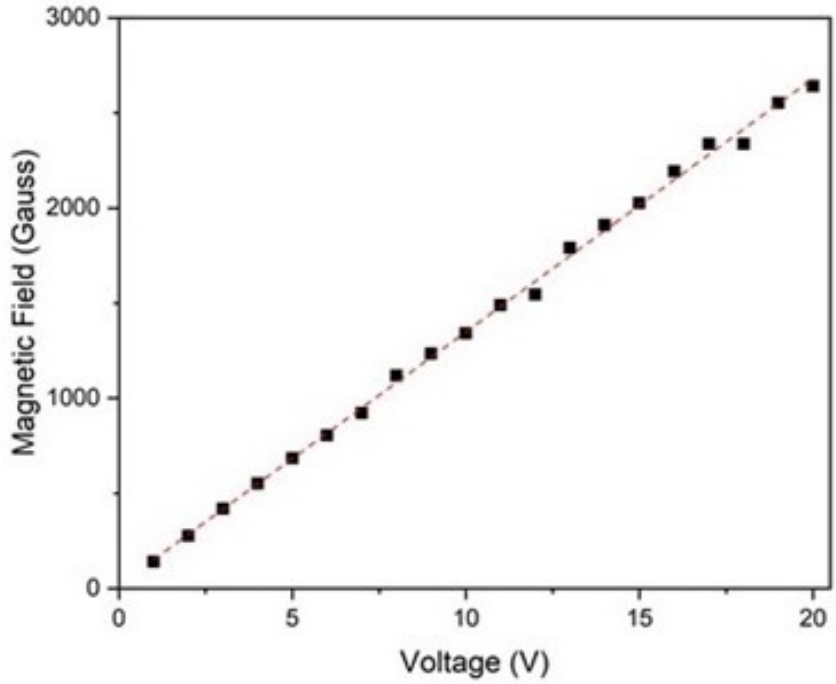

Figure 3.11: The magnetic field generated as a function of the voltage supplied to the electromagnet at the center of the gap between two electromagnets, the red dashed line shows the linear fit of the data.

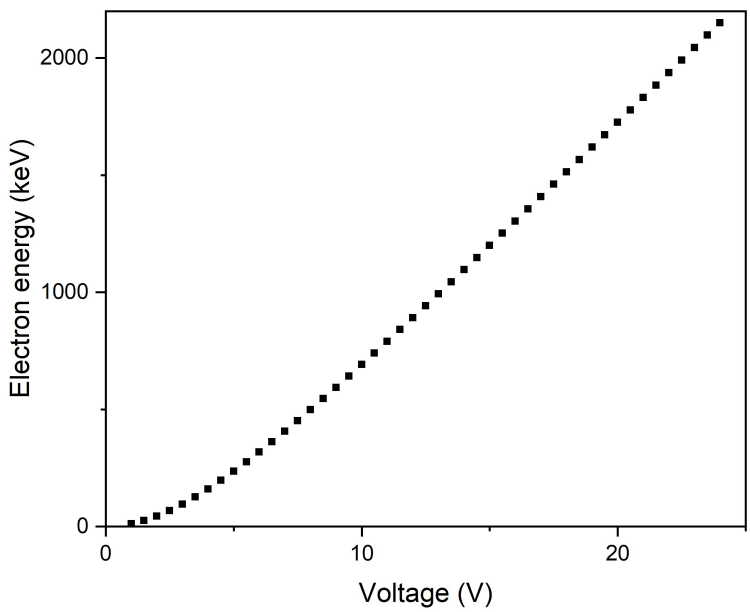

Figure 3.12: Calculated photoelectron energies as a function of voltage supplied to the electromagnet. The maximum photoelectron energy that can reach the center of the detector is approximately 2.1 MeV.

a photomultiplier tube (PMT) to measure high energy photoelectron up to a few MeV range.

In this nuclear instrumentation detection technique, namely scintillation counting, consists of a scintillator which generates photons in response to incident radiation, a sensitive photodetector, in our case, a 2" photomultiplier tube (BURLE 8575). A 1 cm thick scintillator plastic (Bicron BC-408) is used to produce a beam of photons as it excited by an incident beam of energetic photoelectrons. Generated photons are then collected and converted into an electronic signal proportional to the strength of the incident photoelectrons using a photomultiplier tube. We show a schematic drawing in figure 3.13. [20].

This electronic signal was analyzed using two different methods. First, the electronic signal was directly sent to a fast response digital oscilloscope (TDS5052) after the preamplifier (ORTEC VT 120). The electronic signal is then discriminated based on peak pulse voltage. We used fast frame acquisition mode in the data collection. We mostly use this mechanism when calibrating with beta emission sources for its capability of counting a large amount of signal in a relatively short time. The other method, the electronic signals are sent to a preamplifier (Ortec VT 120), voltage discriminator (Ortec 9307), and finally an endoscopic time analyzer (ORTEC PTA 9308), where the signal is being digitized and downloaded to a computer to generated Time-Of-Flight (TOF) histograms. The start of the time-of-flight signal is synced with the laser pulse signal from the regenerative amplifier.

Figure 3.14 shows the scintillation emission spectrum and the PMT photocathode spectral responsibility characteristic. Scintillator emission ranges from 360 nm to 520 nm and has a peak of approximately 430 nm [21], and the PMT response ranges from 280nm to 620nm and has with a peak of approximately 400nm [22]. Together, they make an efficient combination of photoelectron detection. According to specifications given [22], the scintillator provides an approximately 2.5 ns wide (FWHM) output pulses with a rise time of 0.9 ns and decay time of 2.1 ns, thus making it suitable for applications based on fast timing characterizations. Besides, a 10 mm thickness of the

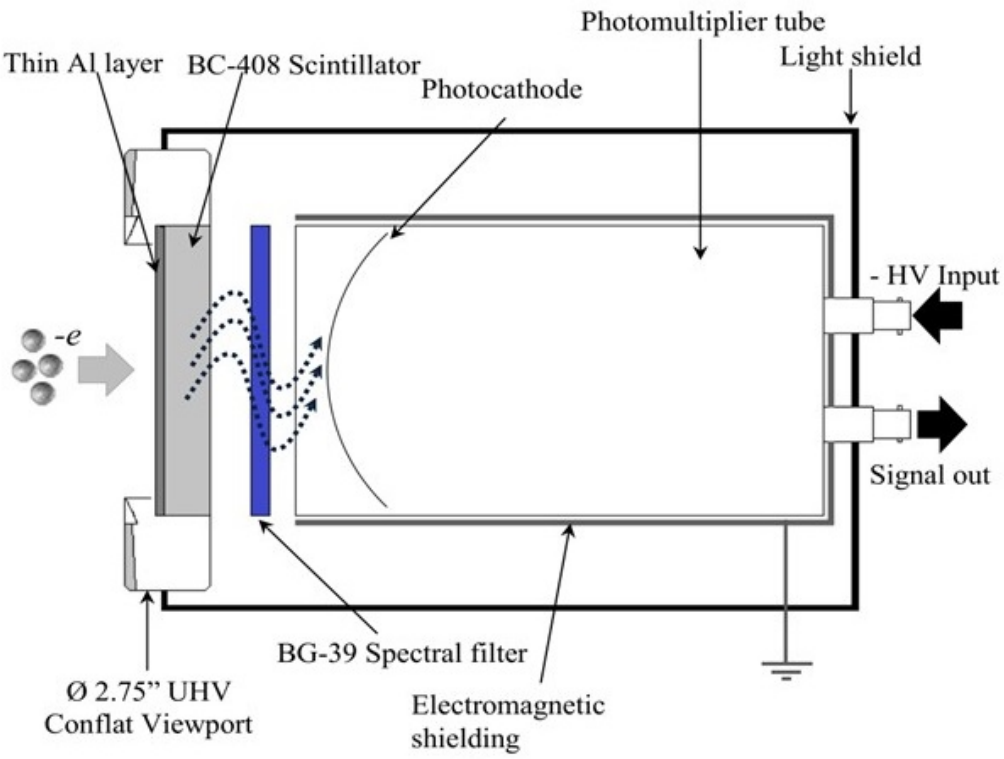

Figure 3.13: Schematic drawing of the scintillator and photomultiplier tube assembly used to detect high energy photoelectrons. Primary incident photoelectrons are represented by -e where a group of dotted arrows represents the beam of scintillation photons generated by the scintillator.

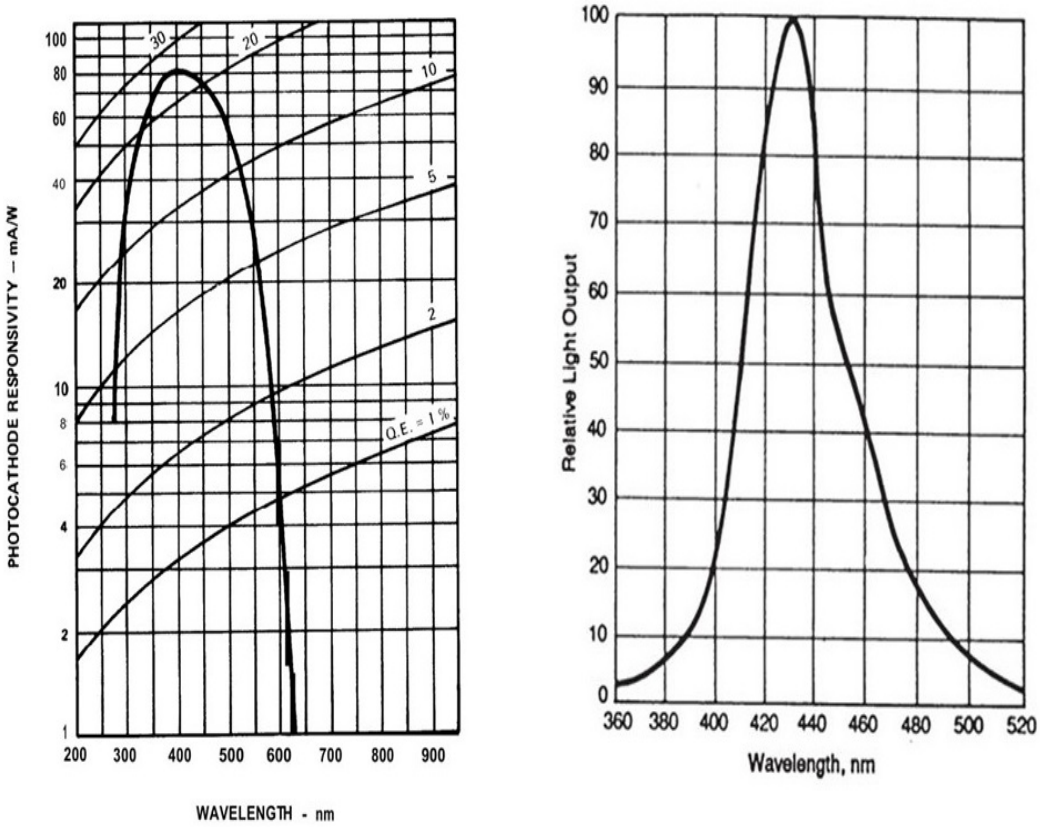

(a) (b)

Figure 3.14: Spectral response curves for 8575 photomultiplier tube (a) and BC-408 scintillator (b). Both the photomultiplier tube and the scintillator are not sensitive to the laser wavelength ($790 \pm 20nm$), therefore significantly reduce the signal noise due to laser photons.

scintillator material is capable of generating photons from photoelectron with kinetic energies up to 2 MeV. Based on the properties of the scintillator material and the selected geometry, the calculated scintillation light yield produced by the scintillator is 1 photon/keV.

The PMT provides a typical gain of 2.7×10^7 at 2000 V bias voltage, PMT is biased using a DC high voltage power supply ($\pm$ 5000 V, PS-350, Stanford Research Systems, Inc.) with a peak-to-peak ripple voltage < 0.002 of full scale. We operated the PMT at a bias voltage of -1750 V (I_{max} = 0.216 mA) in order to maintain its linear counting scale. Additionally, several layers of thick black fabric were utilized to optically isolate the PMT to keep ambient room light from reaching the detector.

Owing to its superior capability of capturing and measuring high energy electrons, we used a scintillator/PMT combination for the primary energy calibration of the electron spectrometer. However, the detection efficiency of such combination drops substantially at low energies ($<$ 50 keV). Therefore, an alternative technique is necessary in order to give us a more efficient way to measure low energy photoelectrons.

3.4.4.2 Micro Channel Plates

Though the majority of measurements were taken with the scintillator and PMT combination, we also introduced a micro channel plate (MCP) detector due to its superior timing characteristics and its efficiency in terms of low energy electron detection. MCP is an array of miniature electron multipliers oriented parallel to one another, allow electron multiplication factors of 10^4 - 10^7 coupled with ultra-high time resolution ($<$ 100 ps) and spatial resolution limited only by the channel dimensions and spacing which made it ideal for measurements about low energy photoelectrons ($<$ 50 keV). In this study, we made use of a matched set of micro channel plates arranged in a high gain Chevron configuration [23].

The top MCP of the Chevron is kept at -150 V potential, where the bottom is set to +1700 V, thus providing a net MCP bias of 1850V to achieve the required signal gain. Generated secondary electrons are further accelerated and collected using

an anode plate kept at +1900 V potential. A capacitively coupled signal plate then generates an electronic signal proportional to secondary electrons arrived at the anode. The electronic signal is then sent to a pre-amplifier (Ortec VT 120), pico-timing discriminator (ORTEC 9307), picosecond time analyzer (ORTEC 9308) and eventually downloaded to the computer system to generate a TOF histogram. Figure 3.15 gives a diagram of the detection scheme.

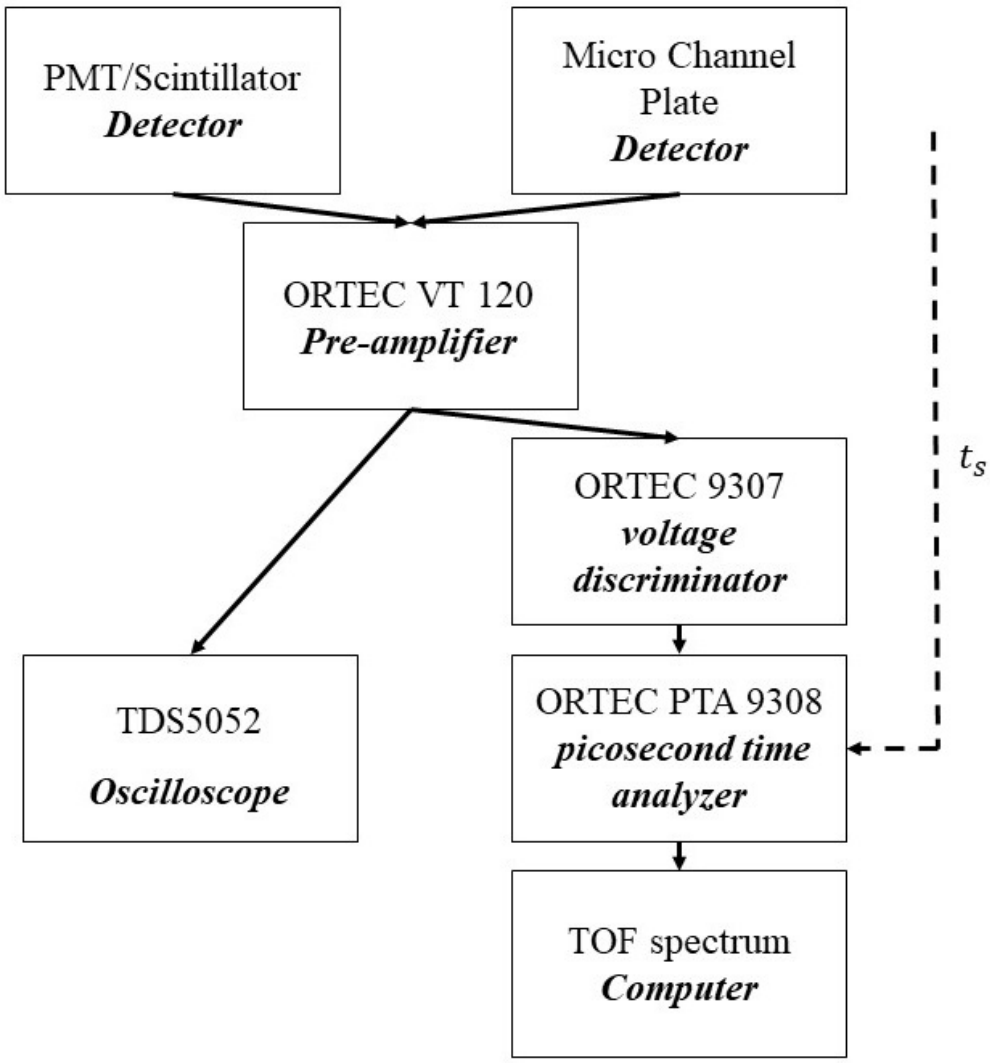

Figure 3.15: Block diagram of the detection scheme. Picosecond analyzer is synchronized with the terawatt laser using a sync signal (t_s), which initiates the analyzer clock to zero at the beginning of every laser pulse.

3.4.5 Background Level

For accurate calibration, it is essential to evaluate the background level. During the experiments, signals fall into four categories: recombination light noise, relativistic electrons, and non-relativistic electrons, which are coming from inside the chamber together with electronic radio frequency noise that is coming from the electronics of the laser system. Recombination light that scatters through the spectrometer baffle slits and makes it to the PMT detector is the primary source of the noise.

An uncoated transparent scintillator (no aluminum thin film) was used to show the recombination light in the data. Baffles are not presented in this experiment; we show results in figure 3.16. Recombination light was granted an unobstructed path into the detection assembly. The results show that with low and nonrelativistic energy photoelectron signals, the photon signal (red) and the electron signal (blue) are well separated in time; therefore, no requirement for baffling or discrimination. However, as the energy of the photoelectrons increases, the photon signal starts to overlap with the electron signal and, ultimately, becomes indistinguishable. As the design goal of this spectrometer is detecting high energy photoelectrons reliably, reduce, or even eliminate the noise coming from the recombination light is going to have a significant impact. The fastest pulse FWHM time for photons and high energy electrons is 4.7 ns FWHM. This response time is a convolution of the spectrometer energy resolution, PMT response (2.5 ns), scintillator decay time (2.5 ns), and electronics.

3.4.6 Noise Reduction

In order to minimize the signal noise generated due to photons and low energy photoelectrons arriving at the detector assembly, we employed several noise-reducing techniques. First, a thin layer of aluminum film is coated on the front surface of the scintillator. Such treatment effectively eliminates unwanted scatter photons and low energy electrons. The required electron attenuation length, λ_z, is calculated using the following formula [24]

$$\lambda_z = \lambda_{1keV} \left(\frac{E_{eV}}{1000} \right)^n \tag{3.13}$$

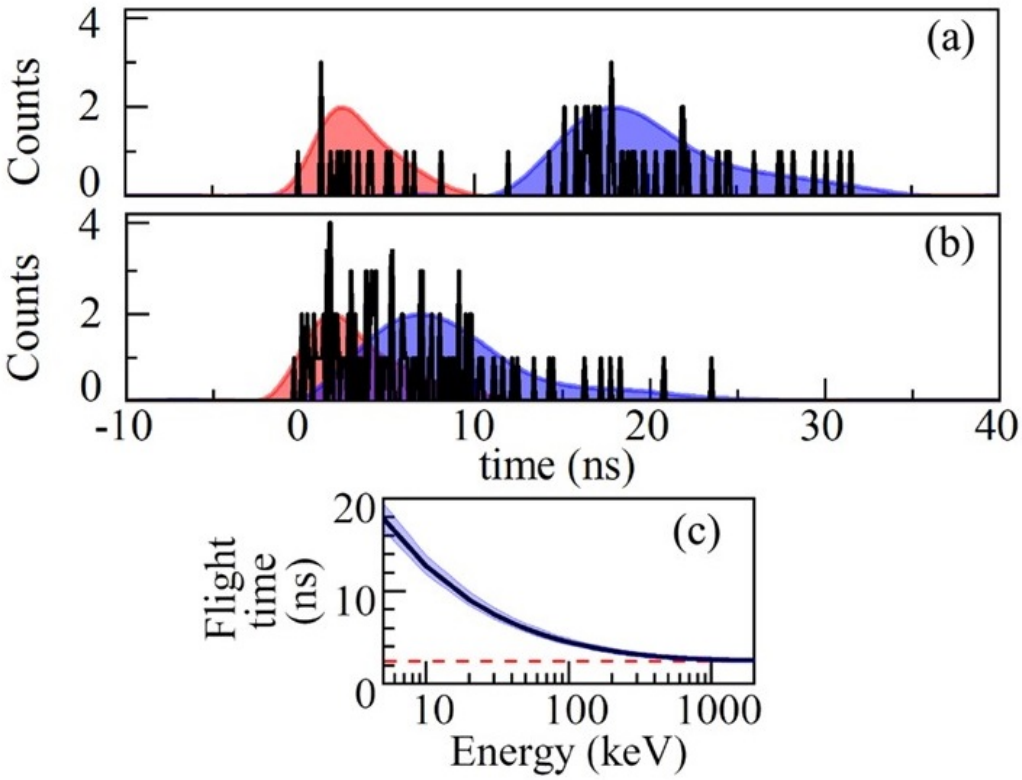

Figure 3.16: The signal from scattered photons (shown for the operation of the spectrometer without full baffling or discrimination) and analyzed electrons at 7 keV (a). A fit (red) is shown for the photons FWHM 4.7 ns and peak at 2.2 ns. The earliest, front edge of the response to light is at -250 ps ± 250 ps. The time axis has been adjusted, so the peak photon response corresponds to the photon flight time. The 7 keV resolved electron signal (blue) has an FWHM of 8.5 ns and a peak at 18 ns. As shown in (b), the TOF spectrum for a 50 keV electron is not resolvable from the photon peak. The 50 keV electron signal has an FWHM of 8.5 ns and a peak at 7 ns. The centroid TOF for the electron signal is shown as a function of energy (c). A dashed red line indicates the flight time for the speed of light.

for a desired percentage transmission given by

$$I/I_0 = e^{\left(-\frac{z}{\lambda_z}\right)} \tag{3.14}$$

where z is the thickness of the aluminum layer. λ_{1keV} and n are constants for a given material. For Al, λ_{1keV} = 1.9nm and n = 0.74. The transmission percentage of the photoelectrons through the deposited Al layer as a function of the thickness for four different energies of electrons is shown in figure 3.17. The thickness of the Al layer is set to 75nm. This thickness helps to reduce photoelectrons with energy less than 10 keV as well as photon from going into the scintillator and as a result, improves the overall signal to noise ratio. This layer of thin aluminum also reflected the scintillation photons towards the PMT, thus improving the overall detection efficiency.

Secondly, we placed a blue bandpass Schott glass filter (Ø50 mm, BG-39) in between the scintillator and the PMT. According to the specification provided, the transmission wavelength ranges from 300 nm to 650 nm with a peak approximately at 500 nm [25], which makes it a prime choice for not only filtering out stray laser photons (790±20 nm), but also allowing the photon signals generated by the scintillator reaching the photomultiplier tube.

Three layers of aluminum baffles are installed between the interaction region and the detection assembly. Those baffles are built to have a tight fit according to the dimensions of the chamber, with a clearance of less than 1 cm, therefore eliminates most photons and scattered electrons. Furthermore, all three baffles were coated with a uniform layer of graphite lubricating resistance coating (Aerodag-G). All three layers are mounted onto the top layer of the turntable, therefore the rotation of the baffles is synchronized with the magnetic analyzer. Each layer has a cutout made according to the simulated photoelectron trajectory to provide desired photoelectrons unobstructed access to the detection assembly placed at the top of the chamber.

We did a study to explore the effectiveness of the baffles using a ^{14}C beta emission radioactive source. Since ^{14}C have relatively low beta emission energy (mean beta particle energy ∼50 keV), a micro channel plate detector was utilized to capture the

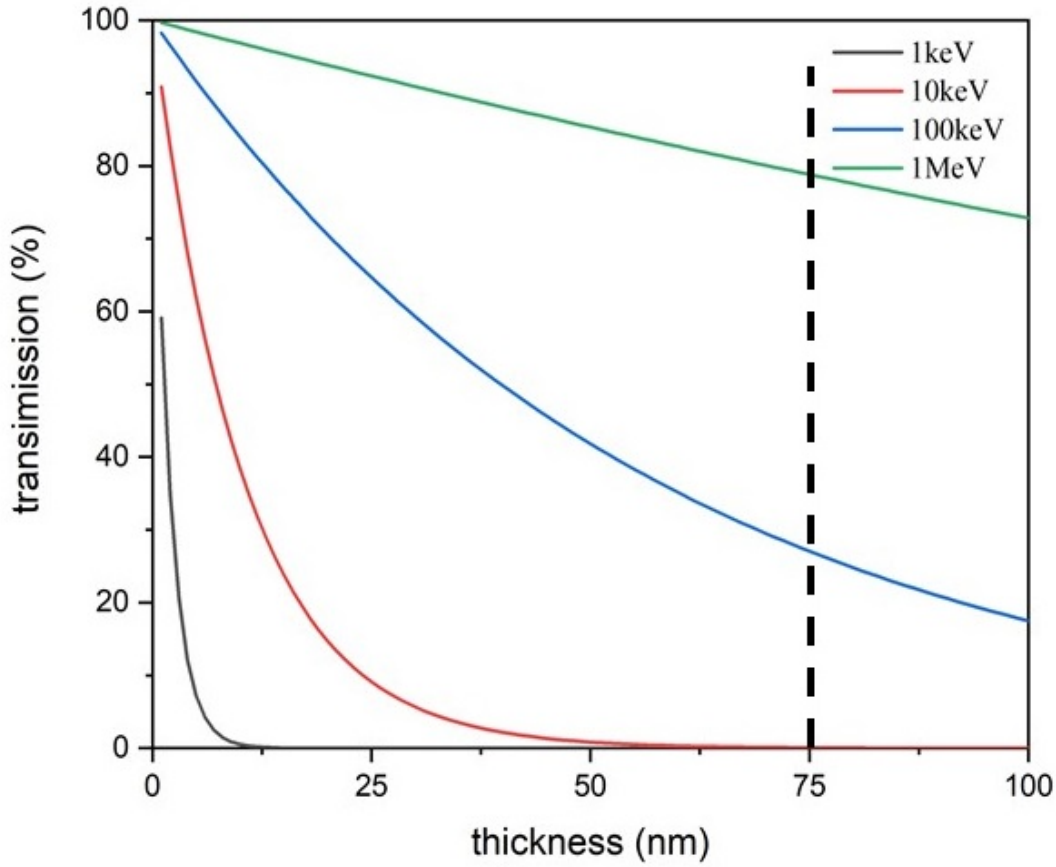

Figure 3.17: Transmission percentage of electrons with kinetic energies 1, 10, 100, and 1000 keV through an Al layer as a function of the layer thickness. To effectively eliminate low energy (< 10 keV) electrons, the thickness of the Al layer used in this study was set to 75 nm (shown by the dashed line).

electrons. The basic concept behind this experiment is straightforward. We deliberately offsetting an angle between the cutout in the baffles and the gap in between the electromagnet, By varying the angle, we recorded the change of the signal rate, therefore, revealing the amount of influence those baffles have on the signal. The ^{14}C source is placed at the position of the laser focus. Three layers of baffles are put in place, and to best replicate the real experiment, the chamber was pumped down to 3×10^{-8} Torr. Figure 3.8 shows the results can. The dark count measurement was done by completely remove the ^{14}C source. As the results suggest, the signal was reduced from an average of $\sim$1650 acquisitions per minute with 0° between the gap and the cutout to $\sim$150 acquisitions per minute from 10°, with a reduction factor of 10. Furthermore, the acquisition rate is virtually identical to those of dark counts, thus give us the confidence to believe the three layers of baffles are very useful in blocking scatter electron or photon signal from reaching the detector.

Finally, two beehive like "traps" were also set up both behind and below the electromagnet, which are also coated with Aerodag-G, to reduce the amount of scattering electrons and photons generated by having electrons hitting either the chamber wall behind or the turntable below the electromagnet.

Electronic radio frequency (RF) from the laser system electronics was another primary source of the noise. For the sake of simplicity, rather than trying to eliminate the noise from its source, the first approach we took was by shielding our detection assembly. Three layers of shields were employed. A layer of copper foil is used to wrap around the PMT, preamp, and connecting cables. Additionally, two layers of aluminum cylinders were custom-built and placed over the whole detector assembly. Those shields can also work as a light blocker to prevent room/background light from reaching the PMT. Furthermore, all the windows on the UHV chamber are double blocked using a thick layer of black fabric and aluminum foil.

With all the noise reduction approach introduced, the detection rate of recombination light was kept to 0.001 counts/shot by using electron and photon baffling slits

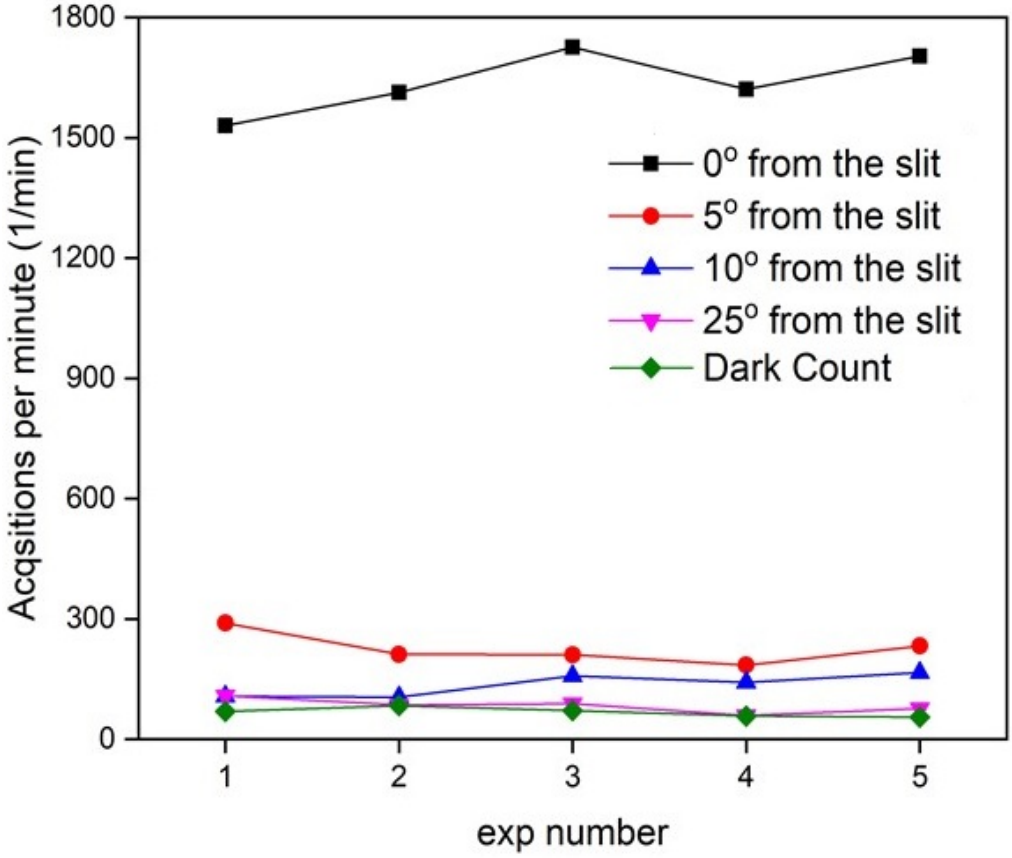

Figure 3.18: Accusations per minute at different angles between baffle cutout and the gap between electromagnet. The acquisition rate is virtually identical with dark count measurements with an angle larger than 10°.

within the spectrometer and two light absorption "traps" behind and blow the electromagnet. We achieved a further reduction to 10^{-6} counts/shot by coating the front of the scintillator with a 75 nm thin aluminum layer as a light block. RF noise is also reduced by three orders of magnitude and kept below the discrimination level.

3.5 Conclusions

We have constructed a high field magnetic deflection photoelectron spectrometer with an energy resolution $\Delta E_k/E_k = 0.4$. The ultimate pressure is at 10^{-9} Torr level. The range of energy detection is currently from 20 keV to 2 MeV. The maximum magnetic field generated by the electromagnet limit the 2MeV value. The spectrometer can choose the polar angle, θ, from 5° to 100° with respect to the laser propagation vector $\hat{k}$ by using the rotational analyzer.

REFERENCES

[1] A. T. Eppink and D. H. Parker, "Velocity map imaging of ions and electrons using electrostatic lenses: Application in photoelectron and photofragment ion imaging of molecular oxygen," *Review of Scientific Instruments*, vol. 68, no. 9, pp. 3477–3484, 1997.

[2] J. Ullrich, R. Moshammer, A. Dorn, R. Dörner, L. P. H. Schmidt, and H. Schmidt-Böcking, "Recoil-ion and electron momentum spectroscopy: reaction-microscopes," *Reports on Progress in Physics*, vol. 66, no. 9, p. 1463, 2003.

[3] S. Backus, C. G. Durfee III, M. M. Murnane, and H. C. Kapteyn, "High power ultrafast lasers," *Review of Scientific Instruments*, vol. 69, no. 3, pp. 1207–1223, 1998.

[4] C. Danson, D. Hillier, N. Hopps, and D. Neely, "Petawatt class lasers worldwide," *High Power Laser Science and Engineering*, vol. 3, 2015.

[5] G. A. Mourou, T. Tajima, and S. V. Bulanov, "Optics in the relativistic regime," *Reviews of Modern Physics*, vol. 78, no. 2, p. 309, 2006.

[6] S. Weber, S. Bechet, S. Borneis, L. Brabec, M. Bučka, E. Chacon-Golcher, M. Ciappina, M. DeMarco, A. Fajstavr, K. Falk, *et al.*, "P3: An installation for high-energy density plasma physics and ultra-high intensity laser–matter interaction at eli-beamlines," *Matter and Radiation at Extremes*, vol. 2, no. 4, p. 149, 2018.

[7] E. Liang, T. Clarke, A. Henderson, W. Fu, W. Lo, D. Taylor, P. Chaguine, S. Zhou, Y. Hua, X. Cen, *et al.*, "High e+/e- ratio dense pair creation with 10 21 w. cm- 2 laser irradiating solid targets," *Scientific Reports*, vol. 5, p. 13968, 2015.

[8] N. Ekanayake, S. Luo, P. D. Grugan, W. B. Crosby, A. D. Camilo, C. V. McCowan, R. Scalzi, A. Tramontozzi, L. E. Howard, S. J. Wells, C. Mancuso, T. Stanev, M. F. Decamp, and B. C. Walker, "Electron shell ionization of atoms with classical, relativistic scattering," *Phys. Rev. Lett.*, vol. 110, p. 203003, May 2013.

[9] G. Tarbox, E. Cunningham, R. Sandberg, J. Peatross, and M. Ware, "Radiation from free electrons in a laser focus at 10 18 w/cm 2: modeling of photon yields and required focal conditions," *JOSA B*, vol. 32, no. 5, pp. 743–750, 2015.

[10] C. Moore, J. Knauer, and D. Meyerhofer, "Observation of the transition from thomson to compton scattering in multiphoton interactions with low-energy electrons," *Physical Review Letters*, vol. 74, no. 13, p. 2439, 1995.

[11] D. Meyerhofer, J. Knauer, S. McNaught, and C. Moore, "Observation of relativistic mass shift effects during high-intensity laser–electron interactions," *JOSA B*, vol. 13, no. 1, pp. 113–117, 1996.

[12] G. D. Glenn, G. Tiwari, G. Dyer, C. Curry, M. Donovan, E. Gaul, M. Gauthier, S. Glenzer, J. Gordon, B. Hegelich, *et al.*, "Improved large-energy-range magnetic electron-positron spectrometer for experiments with the texas petawatt laser," *Journal of Instrumentation*, vol. 14, no. 03, p. P03012, 2019.

[13] M. Vogel, G. Birkl, M. Ebrahimi, D. von Lindenfels, A. Martin, G. Paulus, W. Quint, S. Ringleb, T. Stöhlker, and M. Wiesel, "Extreme-field physics in penning traps," *Hyperfine Interactions*, vol. 236, no. 1-3, pp. 65–71, 2015.

[14] B. Walker, M. Kaluža, B. Sheehy, P. Agostini, and L. DiMauro, "Observation of continuum-continuum autler-townes splitting," *Physical Review Letters*, vol. 75, no. 4, p. 633, 1995.

[15] P. Kruit and F. Read, "Magnetic field paralleliser for 2π electron-spectrometer and electron-image magnifier," *Journal of Physics E: Scientific Instruments*, vol. 16, no. 4, p. 313, 1983.

[16] E. A. Chowdhury, I. Ghebregziabher, J. MacDonald, and B. C. Walker, "Electron momentum states and bremsstrahlung radiation from the ultraintense field ionization of atoms," *Optics Express*, vol. 12, no. 17, pp. 3911–3920, 2004.

[17] E. A. Chowdhury, C. Barty, and B. C. Walker, ""Nonrelativistic" ionization of the L-shell states in argon by a "relativistic" 10^{19} W/cm^2 laser field," *Physical Review A*, vol. 63, no. 4, p. 042712, 2001.

[18] A. Gonsalves, K. Nakamura, J. Daniels, C. Benedetti, C. Pieronek, T. de Raadt, S. Steinke, J. Bin, S. Bulanov, J. van Tilborg, *et al.*, "Petawatt laser guiding and electron beam acceleration to 8 gev in a laser-heated capillary discharge waveguide," *Physical Review Letters*, vol. 122, no. 8, p. 084801, 2019.

[19] "Superior Essex Allex Heavy Build Round Magnet Wire Technical Datasheet." https://www.superioressex.com/uploadedFiles/Magnet_Wire_and_Distribution/North_America/Magnet_Wire_-_Winding_Wire/Allex.pdf.

[20] N. Ekanayake, *Photoionization of highly charged ions from ultra-intense, ultraviolet and near-infrared radiation fields*. PhD thesis, University of Delaware, ProQuest, 2013.

[21] "BC408 Premium Plastic Scintillators datasheet." http://www.detectors.saint-gobain.com/Plastic-Scintillator.aspx.

[22] "BURLE 8575 Photomultiplier datasheet." http://123.physics.ucdavis.edu/shot_files/Burle_8575PMT.pdf.

[23] J. L. Wiza *et al.*, "Microchannel plate detectors," *Nucl. Instrum. Methods*, vol. 162, no. 1-3, pp. 587–601, 1979.

[24] G. W. C. Kaye and T. H. Laby, *Tables of Physical and Chemical Constants*. National Physical Laboratory, 1995.

[25] "BG39 Blue Bandpass Filter datasheet." https://www.newport.com/p/FSQ-BG39.

Chapter 4

SPECTROMETER ENERGY CALIBRATION

4.1 Introduction

Photoelectron spectroscopy constitutes one of the elemental experimental methods used to study high intensity physics and time-resolved chemistry [1]. Different techniques were developed to record a spectrum of photoelectrons [2]. The procedures for the energy calibration of photoelectron spectra are of considerable importance [3]. Precise energy calibration of the magnetic deflection electron spectrometer is an imperative factor as the accuracy of the acquired data solely depends on it. Therefore, careful measurements were taken to calibrate the spectrometer over throughout two orders of magnitude of energy, from 10 keV to 1 MeV.

4.2 Sample Preparation

Beta radioactive sources are selected as the source of electron for our spectrometer energy calibration. Many factors were taken into consideration during the selection process. A broad energy span and high emission activity are preferred, as it will significantly reduce the time needed for data collection.

We used three different sources according to the principles mentioned above. Carbon 14 (^{14}C), emits electrons with an average kinetic energy of 49.5 keV, Q-value of 156.27 keV, and half-life of 5730 years [4]. Cesium 137 (^{137}Cs), emits electrons with an average kinetic energy of 510 KeV, with a Q-value of 1175.63 keV [5], and half-life of 30.17 years [6]. Thallium 204 (^{204}Ti) emits average kinetic energy of 347.5 keV, Q-value of 763.72 keV, and half-life of 3.78 years [7]. Beta emission energies span over two orders of magnitude energy scale from 10 keV to almost 1.2 MeV from all three sources. We obtained Certified radioactive beta emission sources from Spectrum

Techniques, LLC. The maximum activity under domestic and international U.S. NRC exempt quantity, ten μCi was used in these studies. All the beta emission sources are constructed using a 0.02" thick laminate disk that has a small (0.25") aluminum/Mylar window. Each source has a diameter of 1". According to the specification provided by the manufacturer, each source has an uncertainty of $\pm$ 20% of the labeled activity [8].

Among all three sources, ^{137}Cs is also an intense gamma radiation (γ) emission source with gamma energy of 0.6617 MeV [5]. Scintillator detectors are sensitive to gamma rays, as they use crystals that emit light when gamma rays interact with the atoms in the crystals [9]. The intensity of the light is usually proportional to the energy deposited in the crystal by the gamma ray. Therefore, to gain a pure beta emission response from the ^{137}Cs radioactive source, one must prevent gamma radiation from reaching the detector. As we have already shown in section 3.4, three layers of aluminum baffles are in between the interaction region and the detection assembly. We studied the gamma radiation transmission as a function of the thickness of various materials to determine the optimum approach to eliminate the gamma radiation signal.

The linear attenuation coefficient μ describes the fraction of a beam of x-rays or gamma rays that are absorbed or scattered per unit thickness of the absorber. This value accounts for the number of atoms in a cm^3 volume of material and the probability of a photon being scattered or absorbed from the nucleus or an electron of one of these atoms [10]. The transmission function of such x-ray of gamma ray can be written as [11, 12],

$$I = I_0 e^{-\mu x} \tag{4.1}$$

where I is the intensity transmitted across some distance, I_0 is the initial intensity, and x is the thickness of the material. Using attenuation data from the National Institute of Standards (NIST) [13], we show the transmission percentage as a function of the gamma energy for aluminum in figure 4.1.

From figure 4.1, gamma radiation emits by ^{137}Cs, can easily transmit through the aluminum baffles set up in the experiment. Even with the thickness of the aluminum

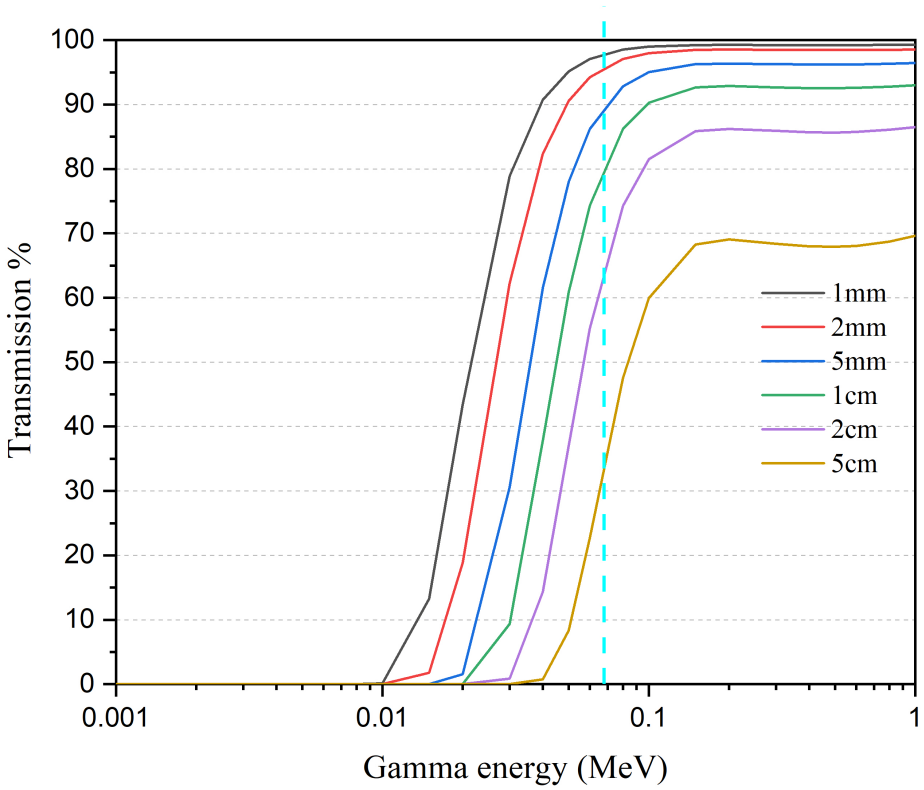

Figure 4.1: Transmission percentage as a function of gamma energy for aluminum, thickness of the aluminum from 1 mm to 5 cm are plotted, total thickness of three layers of aluminum baffles used in the experiment is 1cm, shown in green. Gamma radiation energy of ^{137}Cs is shown with a cyan dashed line.

up to 5cm, the transmission percentage is still at an unacceptable 68.1%. Therefore, seeking an alternative material to attenuate the gamma radiation becomes the apparent resolution. We made a cylinder profile copper housing with a diameter of 10 cm, then placed the ^{137}Cs source in the center. This configuration provided a 5 cm effective attenuation length in each direction. A small slit facing the gap between the electromagnet was also installed to grant beta particles an unobstructed path to the detector. Figure 4.2 shows the transmission percentage of the aluminum baffles together with the copper housing used in the experiment.

The transmission percentage of gamma radiation through the cooper housing is 7.1%, together with the aluminum baffles, the transmission percentage was reduced by two orders of magnitude, therefore significantly reduces the noise generated by the gamma radiation.

4.3 Fit Functions

Beta decay (β-decay) is a type of radioactive decay where a beta particle (electron or positron) is emitted from an atomic nucleus, transforming its original nuclide to its isobar. Beta emission sources used in this calibration are beta minus (β^-) decay, meaning a neutron converts to a proton, and the process creates an electron and an electron antineutrino. From the Fermi theory of beta (β) decay, the shape of the energy distribution for this transition is given approximately by the express [14],

$$F(Z,W) = \frac{2(1+S)}{((2S)!)^2}(2p\rho)^{2S-2}e^{\pi\eta}\left|(S-1+i\eta)!\right|^2 \tag{4.2}$$

where $S = (1-\alpha^2 Z^2)^{1/2}$, $\rho = R/(\hbar/mc)$, R is the nuclear radius, ρ is the electron momentum, Z is the nuclear charge on the daughter nucleus, α is a fine structure constant and $\eta = Ze^2/\hbar V$ where V is the speed of the beta particle far away from the nucleus.

There have been numerous attempts to give Fermi function simpler approximations [15, 16, 17, 18, 19]. In this study, we used the approximation given by Venkataramaiah, P., et al. [20] which is a simple relation for the calculation of the Fermi function

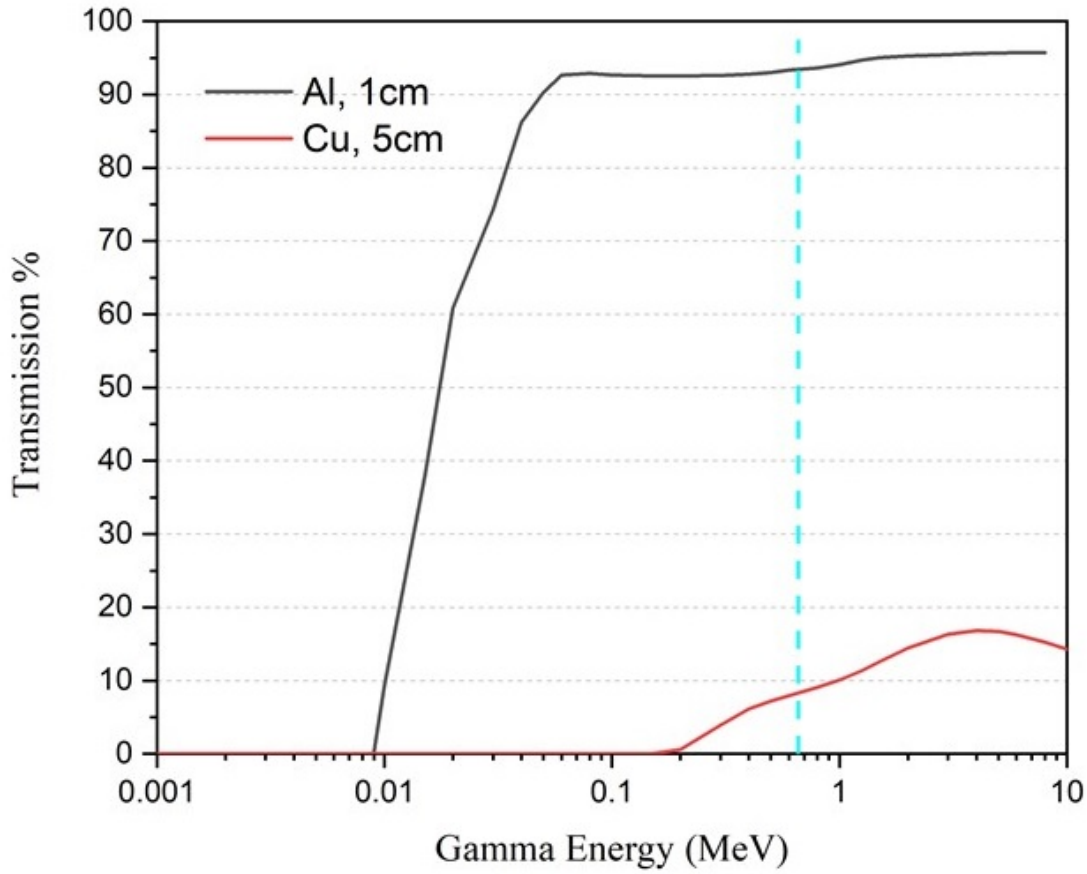

Figure 4.2: Transmission percentage as a function of gamma energy for aluminum (black) and cooper (red). Gamma radiation energy of ^{137}Cs is shown with a cyan dashed line.

for momenta $p \geq 25keV/c$.

$$F(Z,W) = [A + B/(W-1))]^{1/2} \tag{4.3}$$

The constants A and B for the beta emission sources used in the experiment, determined by a regression procedure are given in table 4.1.

Table 4.1: Values of A and B for Fermi function

Isotope	E_0 (keV)	Atomic no. of daugther	A	B
^{14}C	158	7	1.4864	0.0616
^{137}Cs	1173	56	25.2007	23.6665
^{204}Ti	770	82	161.9399	403.5703

Another fitting function used is super-Gaussian function,

$$g(x) = \frac{1}{\sqrt{2\pi}\sigma_0} exp\left(\frac{-(abs(x))^N}{2\sigma_0^N}\right) \tag{4.4}$$

with $\sigma = \sigma_0 \cdot (\pi/2)^{2/(N-1)}$ and σ_0 is the standard deviation. Super-Gaussian distribution is used to describe higher order Gaussian mode, and therefore more rectangular distributions. The steepness of the rectangular shape hints for a possible reduction in size and can be quantified by an additional parameter in the exponent. For $N = 2$ following function will give a Gaussian distribution, and for large N, the function will describe a more rectangular distribution, while small N fits a distribution with long tails on both sides [21]. Figure 4.3 shows the change of shape with different orders Together with a super Gaussian unit step function at Q-value cutoff and a beta decay Fermi function, the beta spectra are fit with the following function,

$$\begin{aligned} C_f exp(-(bE_k/Q_{max})^{20})((bE_k/c + m_e c^2) - (m_e c)^2)^{1/2} \\ \times (bE_k + m_e c^2)(Q_{max} - bE_k)^2 \end{aligned} \tag{4.5}$$

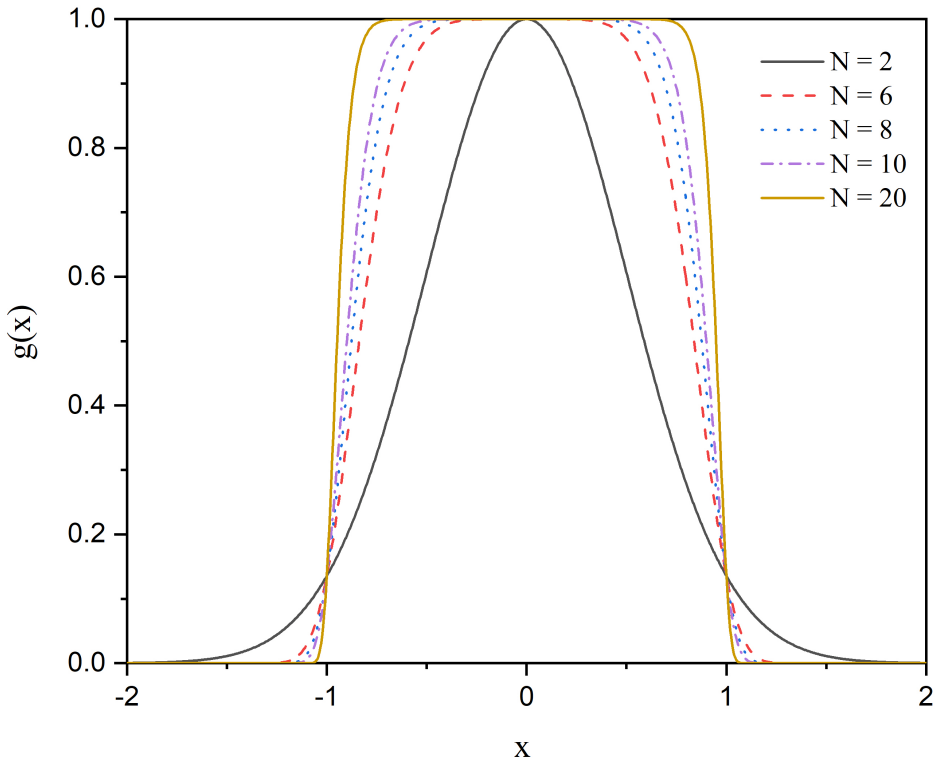

Figure 4.3: Profiles for super Gaussian distributions of orders N = 2, 6, 8, 10 and 20. Order of 20 is used in the fitting function for this experiment.

where C_f (electrons/s) and b (eV/eV) are fitting parameters in the calibration, E_k is kinetic energy of the electron, Q_{max} is the Q-value of each beta emission source, m_e is the rest mass of the electron and c is the speed of light in vacuum. Q_{max} of 0.662 MeV was used for ^{137}Cs due to the high conversion of the 0.662 MeV gamma rays into electrons at the source.

4.4 Experimental Setup

We used a premium plastic scintillator (Bicron BC-408) coupled to a photomultiplier tube (PMT) to perform calibration of the spectrometer owing to its superior capability at measuring high energy electrons. The spectrometer was set up as a high resolution mode as we desire the most accurate calibration results. Emission sources are placed at the laser focal point, temperately setup at the center of the chamber (except for ^{137}Cs, which was placed inside a custom built copper housing and elevated to the laser focal point using aluminum blocks). To best replicate experiment conditions, aluminum baffles are mounted in place, and the PMT configuration was used with standard voltage to acquire electrons from the beta emission sources. The chamber is pumped down using only the rouging pump, and the collection starts when chamber pressure reaches 10^{-1} Torr. We believe this pressure is low enough to generate reliable results for the following reason, the mean free path, which represents the average distance traveled by a moving particle (such as an atom, a molecule, in this case, an electron) between consecutive impacts can be written as

$$\lambda = \frac{RT}{\sqrt{2}\pi d^2 N_A P} \tag{4.6}$$

where R is the ideal gas constant, T is the absolute temperature, d is the diameter of the atom/molecule, N_A is Avogadro's number and P is the pressure.

Based on equation (4.6) at our operating pressure, the mean free path of the electron is 7×10^4 meter, while the average travel distance from the laser focal point to the detector in our spectrometer is 0.7 meter. It is extremely unlikely that any disturbance will impact the electron trajectory from the laser focal point to the detector.

Additionally, unlike MCP detectors, scintillators do not require a UHV environment to operate.

According to the dimensions of the spectrometer and the activities of the beta emission sources, the peak count rate for all three sources is 3 counts/s or $\sim 10^{-4}$ counts/(eV $\cdot$ s). Electronic signals generated by the PMT feeds into an oscilloscope via impedance matched coaxial cable for analysis. PMT signals were voltage discriminated and analyzed using a digital phosphor oscilloscope with two independent 500 MHz channels with 5 GS/s maximum real-time sampling rate (TDS5052). Fast frame accusation was employed as the primary method for signal analyze, due to its exceptional ability to count a large amount of signal in a short time. Event rates at each fixed magnet analyzer current, namely fixed E_k were recorded. 11 - 15 different measurements were taken for each beta emission source, ranging from 10 KeV to beyond the Q-value of each source, i.e., the total energy released in the beta decay. Measurements are done randomly, namely, the currents were not recorded in a particular ascending or descending order. Such arrangement can largely increase the reliability of the data, as it eliminates the chance of having signal change caused by merely the amount of time an apparatus has been operating. Standard demagnetization operations were performed.

4.5 Experimental Results and Discussion

After extracting the information of the count rate at different magnetic analyzer currents, a mapping between count rate and electron energy was obtained using the relationship mentioned in figure 3.12. Measured beta spectra were then fitted using equation (4.5) with the results shown in figure 4.4.

The highest electron energies observed were 125 keV, 750 keV, and 770 keV for ^{14}C, ^{137}Cs, and ^{204}Ti, respectively. The vertical error bar represents signal shot noise. Observations can be made from the beta spectra presented above in the low energy region ($<$ 50 keV). The deviation of the expected value from the measurements is relatively large, this is expected as detected electrons below 25 keV are not used in the

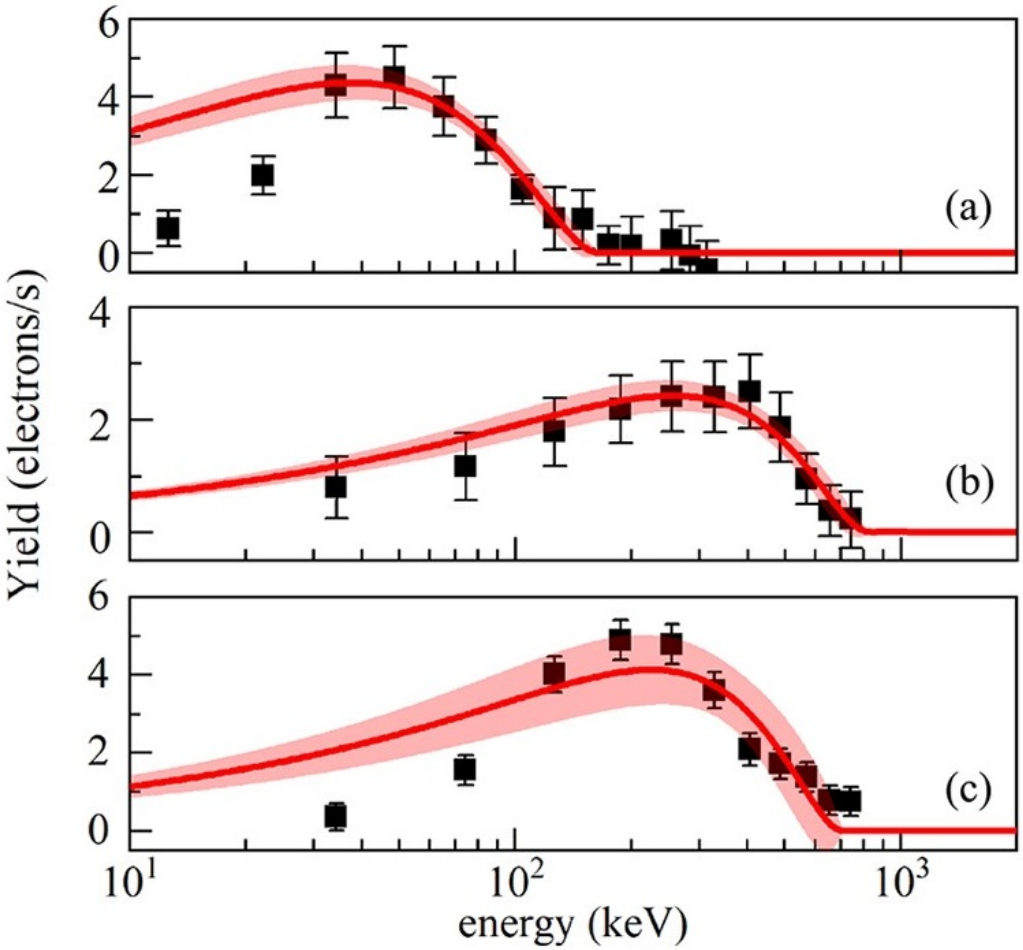

Figure 4.4: Electron yields with a 3 cm scintillator and PMT detector configured is shown with ^{14}C (a), ^{137}Cs (b) and ^{204}Ti (c). 95 % confidence band are shown with shading.

fitting routines due to their limited validity with the Fermi beta function. Furthermore, scintillators are known to have a low detection efficiency at low energy range [22]. Measurement values agree with the expected value much more closely in the high energy region (> 50 keV) of the beta spectra. Results indicate the spectrometer is capable of detecting high energy electrons with high efficiency. Based upon these fits, we expect an energy calibration accuracy of 10% for the spectrometer.

4.6 Conclusions

We have presented spectrometer calibration using three beta emission radioactive sources, ^{14}C, ^{137}Cs, and ^{204}Ti. Electrons with energies up to 770 keV are observed in the experiment. The beta spectra above 50 keV, in terms of electrons yield per second, are in agreement with a super Gaussian unit step function at Q cutoff and a beta decay Fermi function fitting function. The agreement indicates the spectrometer is capable of capturing high energy electron with high efficiency.

For electron energies below 25 keV, we noticed a large deviation from the fitting function and measurement value. It is caused by the inherited lack of validity with the Fermi beta function at such energies.

REFERENCES

[1] E. T. Nibbering, H. Fidder, and E. Pines, "Ultrafast chemistry: using time-resolved vibrational spectroscopy for interrogation of structural dynamics," *Annu. Rev. Phys. Chem.*, vol. 56, pp. 337–367, 2005.

[2] A. Kothe, J. Metje, M. Wilke, A. Moguilevski, N. Engel, R. Al-Obaidi, C. Richter, R. Golnak, I. Y. Kiyan, and E. F. Aziz, "Time-of-flight electron spectrometer for a broad range of kinetic energies," *Review of Scientific Instruments*, vol. 84, no. 2, p. 023106, 2013.

[3] G. Johansson, J. Hedman, A. Berndtsson, M. Klasson, and R. Nilsson, "Calibration of electron spectra," *Journal of Electron Spectroscopy and Related Phenomena*, vol. 2, no. 3, pp. 295–317, 1973.

[4] "C-14, comments on evaluation of decay data." http://www.nucleide.org/DDEP_WG/Nuclides/C-14_com.pdf.

[5] "Table of Radioactive Isotopes Cs-137." http://ie.lbl.gov/toi/nuclide.asp?iZA=550137.

[6] "Radionuclide half-life measurements data." https://www.nist.gov/pml/radionuclide-half-life-measurements-data.

[7] "Table of Radioactive Isotopes, TI-204." http://nucleardata.nuclear.lu.se/toi/nuclide.asp?iZA=810204.

[8] "Beta/gamma laminate disk sources." http://www.spectrumtechniques.com/products/sources/laminate-sources/.

[9] W. R. Leo, *Techniques for nuclear and particle physics experiments: a how-to approach; 2nd ed.* Berlin: Springer, 1999.

[10] "Transmitted Intensity and Linear Attenuation Coefficient." https://www.nde-ed.org/EducationResources/CommunityCollege/Radiography/Physics/attenuationCoef.htm.

[11] W. D. Ehmann and D. E. Vance, *Radiochemistry and nuclear methods of analysis.*

[12] B. Shleien and M. S. Terpilak, "The health physics and radiological health handbook," 1992.

[13] N. I. of Standards and Technology, "Xcom photon cross-sections database." https://physics.nist.gov/PhysRefData/XrayMassCoef/tab3.html, 1999.

[14] E. Fermi, "An attempt of a theory of beta radiation. 1.," *Z. Phys.*, vol. 88, no. UCRL-TRANS-726, pp. 161–177, 1934.

[15] N. Mott and H. Massey, *The Theory of Atomic Collisions, by N.F. Mott and H.S.W. Massey. 2nd Edition.* Clarendon Press (printed by C. Batey), 1949.

[16] H. A. Bethe and R. F. Bacher, "Nuclear physics a. stationary states of nuclei," *Reviews of Modern Physics*, vol. 8, no. 2, p. 82, 1936.

[17] D. Wilkinson, "The evaluation of allowed β-decay," *Nuclear Physics A*, vol. 143, no. 2, pp. 365–372, 1970.

[18] K. Siegbahn, *Alpha-, beta- and gamma-ray spectroscopy.* No. v. 1 in Alpha-, Beta- and Gamma-ray Spectroscopy, North-Holland Pub. Co., 1965.

[19] R. Evans, *The Atomic Nucleus.* International series in pure and applied physics, McGraw-Hill, 1972.

[20] P. Venkataramaiah, K. Gopala, A. Basavaraju, S. Suryanarayana, and H. Sanjeeviah, "A simple relation for the fermi function," *Journal of Physics G: Nuclear Physics*, vol. 11, no. 3, p. 359, 1985.

[21] F.-J. Decker, "Beam distributions beyond rms," in *AIP Conference Proceedings*, vol. 333, pp. 550–556, AIP, 1995.

[22] J. Birks and F. Brooks, "Scintillation response of anthracene to 6-30 kev photoelectrons," *Proceedings of the Physical Society. Section B*, vol. 69, no. 7, p. 721, 1956.

Chapter 5

LASER PHOTOIONIZATION SPECTRA

5.1 Introduction

Ultrahigh intensity laser light has always been imperative for advances across a board range of topics, including plasma physics [1], quantum control [2], multielectron ionization [3], recollision dynamics [4], attosecond science [5], molecular dynamics [6], optical science [7], high harmonic generation [8], coherent x-rays [9], and laser-induced fusion [10] to name a few. Current laser technology [11] has bought about the ultrahigh intensities ($\sim 10^{19}$ W/cm^2) in a laser focus, and the current goal of design [12] is an ambitious 10^{24} W/cm^2. These ultrastrong fields exceed the traditional strong field regime and push the physics into relativistic interactions.

In traditional strong fields (up to 10^{16} W/cm^2), experiments have verified the majority of the electrons released process kinetic energies < 200 eV [13]. Since the electron's kinetic energy is small compared to its rest mass energy, the electrons possess a speed insignificant compared to that of light. Traditional spectroscopy techniques such as time-of-flight (TOF), velocity map imaging [14], and cold target recoil ion momentum spectroscopy [15] have revolutionized laser-matter interactions measurements. Precision measurements of photoelectron momentum and energy distributions have provided essential insight into dynamics in strong laser fields [13].

Beyond the strong field, ultrastrong laser fields have increased laboratory light sources to intensities "billions and billions" time the intensity of sunlight on the earth [16]. Ultra-intense light-matter interactions have a profound influence on high field physics through the break down of the approximation $v/c = 0$, as photoelectrons with millions of electron-volts of energies been created by lasers [17], the introduction of laser

magnetic field effect, $\vec{B}_{laser}$, suppression of non-sequential ionization and many other phenomena. Atomic measurements have demonstrated the production of relativistic electrons from atoms interaction with an ultrastrong field by direct measurement of the photoelectron [18, 19] and indirectly from Thomson radiation [20]. At 10^{19} W/cm^2, the interaction of ultraintense laser with atoms and molecules creates photoelectrons with energies of 10^6 eV [21], well beyond the 200 eV limit of conventional apparatus. Traditional laser-matter spectroscopy techniques failed to accurately analyze photoelectrons and ions from ultrahigh intensity studies with terawatt and petawatt laser systems.

In this chapter, we present and discuss the results of experiments measuring the photoelectron spectra, angular distributions and photoelectron yields from the interaction of argon (Ar) atoms and chloromethane (CH_3Cl) molecules with a laser field of peak intensity of 1×10^{19} W/cm^2, center wavelength 790 nm and a pulse duration of 40 fs. The forward polar angles of $\theta = 90°$ and $\theta = 75°$ were integrated. The maximum photoelectron energy of 1.4 MeV was observed.

5.2 Photoelectron Dynamic in Relativistic Laser Fields

In the non-relativistic limit, the kinematics of a photoelectron in a laser is fully classical. Laser's electric field $\vec{E}_{laser}$ will impact the dynamic of the photoelectron. However, once entered the relativistic regime, namely $v/c \approx 1$, as we discussed previously that the laser magnetic field, $\vec{B}_{laser}$ is no longer neglectable, one can express Newton's second law as,

$$\frac{d\vec{p}}{dt} = e(\vec{E}_{laser} + \vec{v} \times \vec{B}_{laser}) \tag{5.1}$$

where e is the charge of an electron, t is the time, and the momentum $\vec{p}$ is

$$\vec{p} = \gamma m_0 \vec{v} \tag{5.2}$$

and γ is the Lorentz factor

$$\gamma = \frac{1}{\sqrt{1 - v^2/c^2}} \tag{5.3}$$

Here m_0 is the rest mass of the electron, v is the electron's velocity, and c is the speed of light in vacuum. In the paraxial limit, one can neglect all field components except the transverse fields, the field components in equation (5.1) can be written as,

$$\left|\vec{E}_x\right| = c\left|\vec{B}_y\right| \tag{5.4}$$

while field components on the other directions are.

$$\left|\vec{E}_y\right| = \left|\vec{E}_z\right| = \left|\vec{B}_x\right| = \left|\vec{B}_z\right| = 0 \tag{5.5}$$

Equations above localize electron motion to the $\hat{x}$-$\hat{z}$ plane so that,

$$p_z = \frac{p_x^2}{2m_0c} \tag{5.6}$$

The coordinate system used here has been discussed in Section 3.2. Equation (5.6) confines the motion of the electron to the plane containing the polarization and propagation axes. However, in ultrastrong fields, nonparaxial field components [22] can significantly alter the path of the free electron [23]. Such factors expose photoelectrons to more extended and complicated regions of the ultrastrong laser focus. For that, longitudinal field terms must be included to describe the motion of photoelectrons in ultrastrong fields accurately.

5.3 Experimental Setup

A university scale chirped pulse amplification (CPA) laser system [24] operating at the terawatt (10^{12} W) level is used in this experiment. It consisting of a Ti:sapphire self-mode-lock oscillator seeding a ring-type regenerative amplifier and a bow-tie multipass amplifier with a final output of 150 mJ/pulse at 790 nm with a 40 fs pulse duration operating at 10 Hz. A 30° off-axis f/2 parabolic gold-coated mirror focused the laser beam to a spot size of 2 μm in an effusive room temperature sample gas jet. The laser system and focusing geometry have demonstrated intensities of 10^{19} W/cm^2 [21, 25]. During collections, the working pressure in the chamber from the sample gas is kept below 10^{-7} Torr with a typical collection done at 2×10^{-8} Torr.

Data collections typically involve 1200 to 20000 laser shots, with the most extended collection take up to 100000 shots, in other words, several hours with the 10 Hz repetition rate laser system. Two considerable issues arose from the exceedingly time consuming data collections, namely, maintaining the laser stability and keeping the magnetic field consistent.

To resolve issues of this kind, we restrained the maximum amount of laser shots for a single collection to 9000, namely, 15 minutes. This approach provided us several benefits. It allows a routine check of the laser power in-between measurements. A light scattering screen was set up right before the laser entering the chamber. The scattered light was then captured using a photodiode with a series of neutral density filters to avoid detector saturation or damage. The laser system is tweaked based on the photodiode measurements. On the other hand, photoelectron energy measurements are taken randomly. Data collected at the same current will be combined and analyzed.

Ohmic heating introduced resistance increasing, together with residual magnetic field caused by magnetic hysteresis effect could significantly affect the reliability of the measurements. Therefore they must be addressed with great caution. Current going through the electromagnet was monitored throughout the entire data collection by a digital multimeter with a resolution of 0.001 A, the current variation never exceeds 0.02 A during collections. A dark count/background measurement was carried out following every measurement. Rather than disconnect the electromagnet from the DC power supply, they were connected with reverse polarity, therefore created an opposite field. A configuration of this kind ruled out the residual magnetic field, hence ensuring a pure background from the detector. Additionally, dark count measurements are typically taken at a reduced voltage, so it can also act as a "cool down" time for the electromagnet.

Once the photoelectrons have been deflected, a 1 cm thick plastic scintillator optically coupled to a 2" fast PMT was used to detect the photoelectrons. Signals are sent to a preamplifier (Ortec VT 120), a voltage discriminator (Ortec 9307), and finally a picosecond time analyzer (Ortec PTA 9308), the signal is then digitized and

downloaded to a computer to generate TOF histograms. A sample TOF spectrum is shown in figure 5.1. Signals in the TOF spectrum were selected by the calculated flight time of different energies of photoelectrons. Two factors determine the range of timing window, the energy resolution of the spectrometer, $\Delta E_K/E_k = 0.4$, and the response time of the electronics utilized in this experiment, namely, PMT response (2.5 ns), scintillator decay time (2.5 ns), and other electronics. The fastest pulse full-width at half-maximum (FWHM) is 4.7 ns for photons and high energy electrons. Figure 5.2 illustrates the centroid arrival time of different photoelectron energies in the TOF histogram.

5.4 Energy and Angle Resolved Photoelectron Spectra

The energy resolved photoelectron spectra for a linear polarized laser field with a peak intensity of 1×10^{19} W/cm^2 is shown in figure 5.3, 5.4, 5.5 in units of electron counts per laser shot into a keV energy bin. The collections are at $\theta = 90°$ and $\theta = 75°$ from $\hat{k}$ of the laser propagation direction for argon (Ar) and $\theta = 75°$ for chloromethane (CH_3Cl). The horizontal error bars represent the 40% energy uncertainty $\Delta E_k/E_k$ of the spectrometer. The vertical error bars represent signal shot noise, the noise floor of the spectrometer calculated from the background/dark measurements are shown with gray shading.

The energy spectra reveal photoelectrons with energies from 20 keV up to a maximum energy of 1.4 MeV for both argon (Ar) and chloromethane (CH_3Cl). The intensity of 1×10^{19} W/cm^2 is lower than in previous studies, primarily due to wavefront distortions in the final steering optics to the chamber and parabolic focusing optic. The intensity is still sufficiently high to ionize the L shell of argon, which is the source of high energy electrons at an energy of order 1 MeV. With the low energy electrons have the highest probability of production. The electron yield decreases as the energy increases. However, the yield of high energy electrons at this energy will be lower by a factor of 10^1 to 10^2.

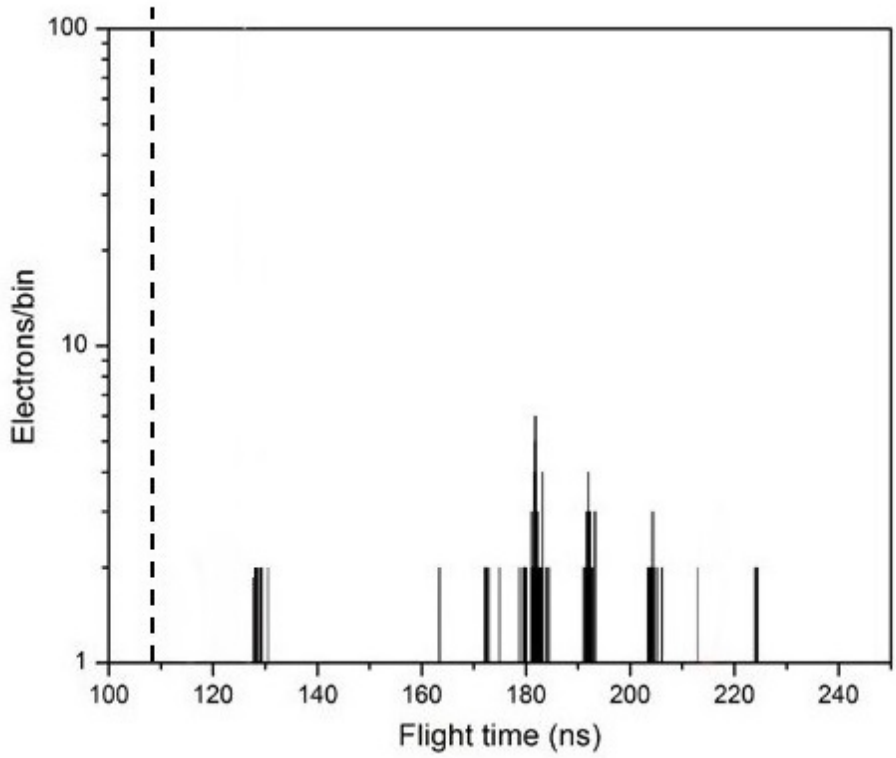

Figure 5.1: Sample time of flight spectrum obtained, thick dark lines represent the captured electron counts per time bin. The dashed line represents the photon flight time ($\sim$ 107 ns).

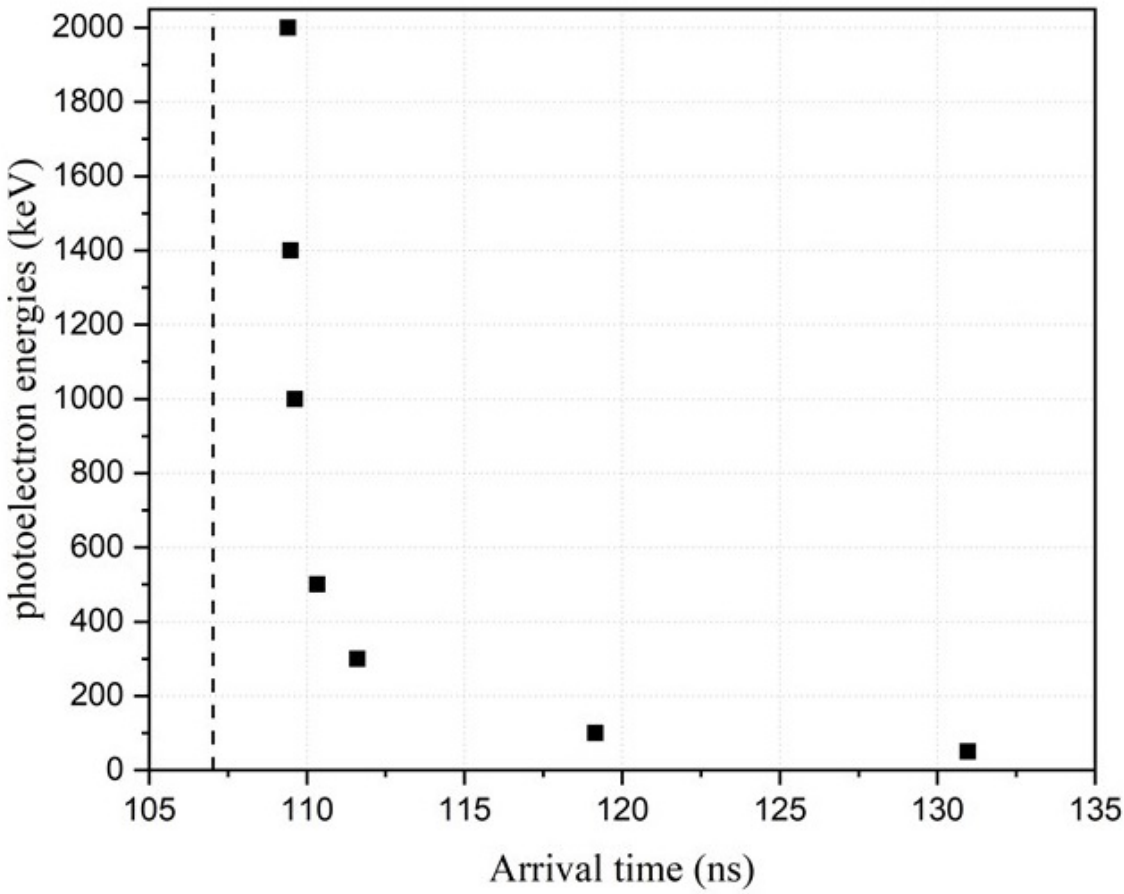

Figure 5.2: Centroid arrival time as a function of different photoelectron energies, the dashed line represents the arrival time of photons ($\sim$ 107 ns).

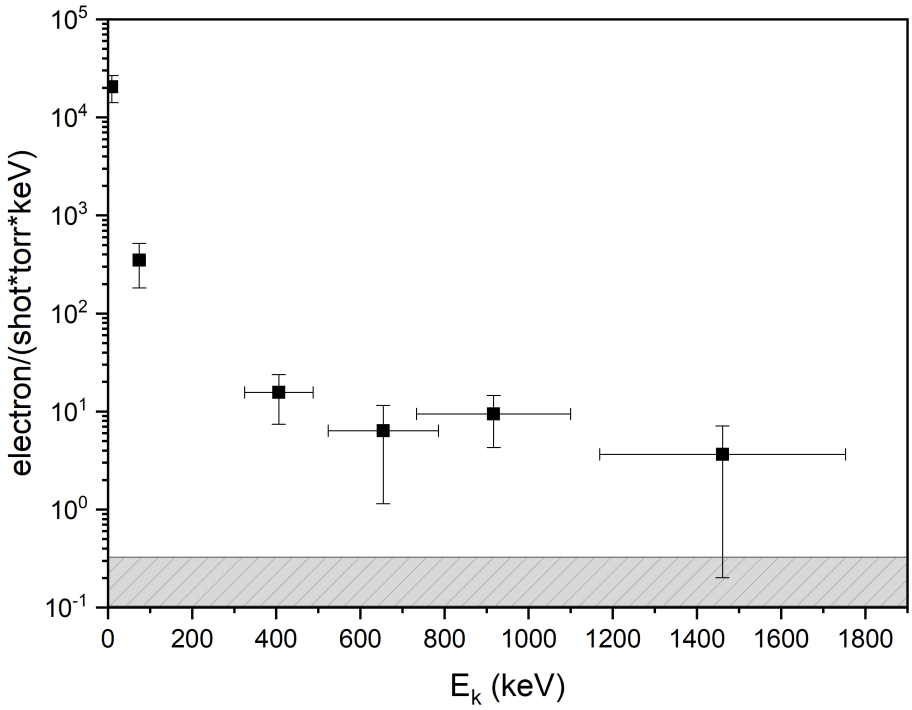

Figure 5.3: Photoelectron spectra in the single atom limit at an intensity of 1×10^{19} W/cm^2. Chloromethane is shown at $\theta = 75°$ The resolution of $\Delta E_k/E_k$ is shown with horizontal error bars and vertical error bars represent signal shot noise. Gray shading shows the noise floor.

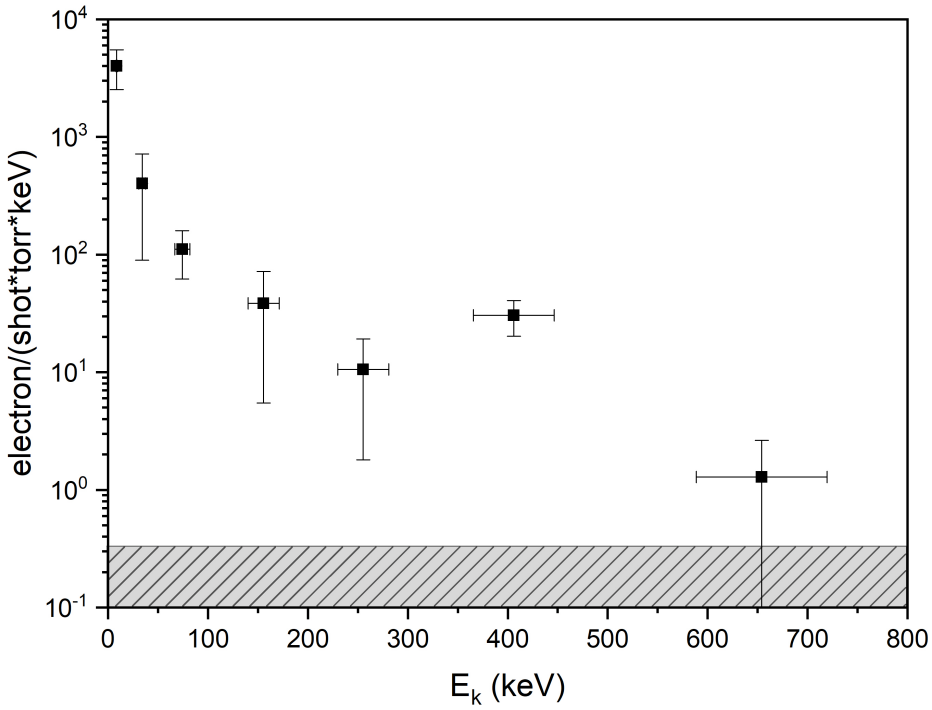

Figure 5.4: Photoelectron spectra in the single atom limit at an intensity of 1×10^{19} W/cm^2. Argon is shown at $\theta = 90°$. The resolution of $\Delta E_k/E_k$ is shown with horizontal error bars, and vertical error bars represent signal shot noise. Gray shading shows the noise floor.

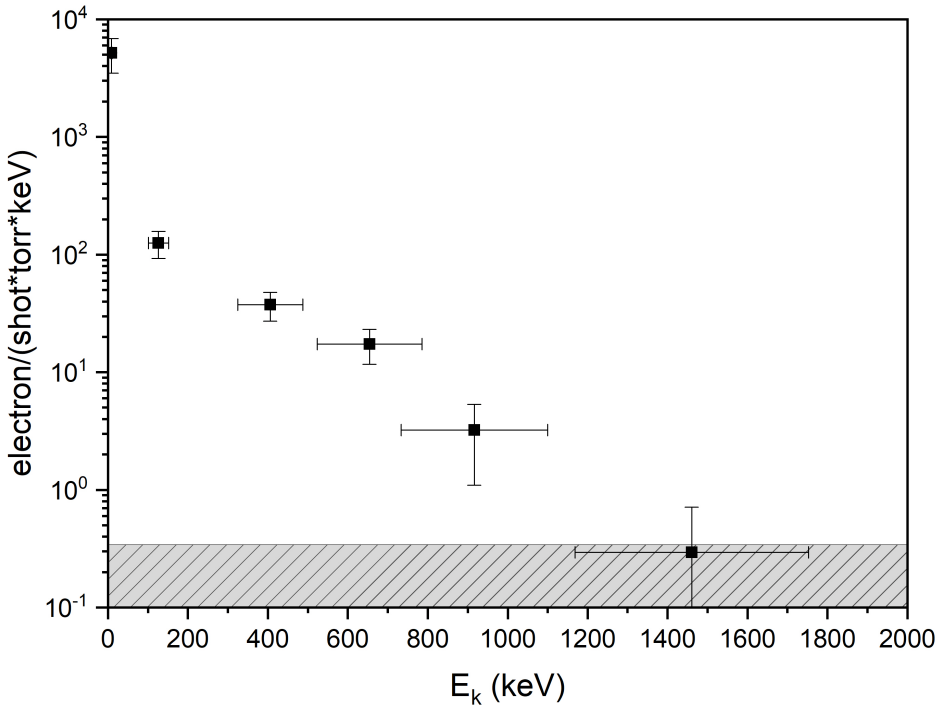

Figure 5.5: Photoelectron spectra in the single atom limit at an intensity of 1×10^{19} W/cm^2. Argon at $\theta = 75°$ is shown. The resolution of $\Delta E_k/E_k$ is shown with horizontal error bars, and vertical error bars represent signal shot noise. Gray shading shows the noise floor.

5.5 Conclusions

We have constructed a MeV photoelectron spectrometer that is capable of collecting $> 10^4$ signal dynamic range electron spectra with atomic and molecular samples in ultrahigh intensities at different angles and $\Delta E_k/E_k$ energy resolution. The presented UHV, magnetic deflection spectrometer with a rotational analyzer is capable of quantifying photoelectrons from the single atom and molecule response to an ultrahigh intensity laser. The specifications included a range of energies from 20 keV to 2 MeV, an angular resolution 2°, an adjustable measurement angle within a solid angle of $\sim 2\pi$ steradian, and a noise floor of order 10^{-1} events/(shot-Torr-keV).

REFERENCES

[1] W. P. Leemans, B. Nagler, A. J. Gonsalves, C. Toth, K. Nakamura, C. G. Geddes, E. Esarey, C. Schroeder, and S. Hooker, "Gev electron beams from a centimetre-scale accelerator," *Nature Physics*, vol. 2, no. 10, p. 696, 2006.

[2] R. J. Levis, G. M. Menkir, and H. Rabitz, "Selective bond dissociation and rearrangement with optimally tailored, strong-field laser pulses," *Science*, vol. 292, no. 5517, pp. 709–713, 2001.

[3] A. N. Pfeiffer, C. Cirelli, M. Smolarski, R. Dörner, and U. Keller, "Timing the release in sequential double ionization," *Nature Physics*, vol. 7, no. 5, p. 428, 2011.

[4] A. Shiner, B. Schmidt, C. Trallero-Herrero, H. J. Wörner, S. Patchkovskii, P. B. Corkum, J. Kieffer, F. Légaré, and D. Villeneuve, "Probing collective multi-electron dynamics in xenon with high-harmonic spectroscopy," *Nature Physics*, vol. 7, no. 6, p. 464, 2011.

[5] P. . M. Paul, E. Toma, P. Breger, G. Mullot, F. Augé, P. Balcou, H. Muller, and P. Agostini, "Observation of a train of attosecond pulses from high harmonic generation," *Science*, vol. 292, no. 5522, pp. 1689–1692, 2001.

[6] S. Baker, J. S. Robinson, C. Haworth, H. Teng, R. Smith, C. Chirilă, M. Lein, J. Tisch, and J. P. Marangos, "Probing proton dynamics in molecules on an attosecond time scale," *Science*, vol. 312, no. 5772, pp. 424–427, 2006.

[7] C. Thaury, F. Quéré, J.-P. Geindre, A. Levy, T. Ceccotti, P. Monot, M. Bougeard, F. Réau, P. d'Oliveira, P. Audebert, *et al.*, "Plasma mirrors for ultrahigh-intensity optics," *Nature Physics*, vol. 3, no. 6, p. 424, 2007.

[8] M. Lewenstein, P. Balcou, M. Y. Ivanov, A. L'Huillier, and P. B. Corkum, "Theory of high-harmonic generation by low-frequency laser fields," *Phys. Rev. A*, vol. 49, pp. 2117–2132, Mar 1994.

[9] T. Popmintchev, M.-C. Chen, D. Popmintchev, P. Arpin, S. Brown, S. Ališauskas, G. Andriukaitis, T. Balčiunas, O. D. Mücke, A. Pugzlys, *et al.*, "Bright coherent ultrahigh harmonics in the kev x-ray regime from mid-infrared femtosecond lasers," *Science*, vol. 336, no. 6086, pp. 1287–1291, 2012.

[10] S. Glenzer, B. MacGowan, P. Michel, N. Meezan, L. Suter, S. Dixit, J. Kline, G. Kyrala, D. Bradley, D. Callahan, *et al.*, "Symmetric inertial confinement fusion implosions at ultra-high laser energies," *Science*, vol. 327, no. 5970, pp. 1228–1231, 2010.

[11] B. C. Walker, C. Toth, D. N. Fittinghoff, T. Guo, D.-E. Kim, C. Rose-Petruck, J. A. Squier, K. Yamakawa, K. R. Wilson, and C. P. Barty, "A 50-ew/cm 2 ti: sapphire laser system for studying relativistic light-matter interactions," *Optics Express*, vol. 5, no. 10, pp. 196–202, 1999.

[12] S. Weber, S. Bechet, S. Borneis, L. Brabec, M. Bučka, E. Chacon-Golcher, M. Ciappina, M. DeMarco, A. Fajstavr, K. Falk, *et al.*, "P3: An installation for high-energy density plasma physics and ultra-high intensity laser–matter interaction at eli-beamlines," *Matter and Radiation at Extremes*, vol. 2, no. 4, p. 149, 2018.

[13] B. Walker, B. Sheehy, K. C. Kulander, and L. F. DiMauro, "Elastic rescattering in the strong field tunneling limit," *Physical Review Letters*, vol. 77, no. 25, p. 5031, 1996.

[14] A. T. Eppink and D. H. Parker, "Velocity map imaging of ions and electrons using electrostatic lenses: Application in photoelectron and photofragment ion

imaging of molecular oxygen," *Review of Scientific Instruments*, vol. 68, no. 9, pp. 3477–3484, 1997.

[15] R. Moshammer, D. Fischer, and H. Kollmus, "Recoil-ion momentum spectroscopy and "reaction microscopes"," in *Many-particle quantum dynamics in atomic and molecular fragmentation*, pp. 33–58, Springer, 2003.

[16] U. Keller, "Recent developments in compact ultrafast lasers," *Nature*, vol. 424, no. 6950, p. 831, 2003.

[17] T. Cowan, A. Hunt, T. Phillips, S. Wilks, M. Perry, C. Brown, W. Fountain, S. Hatchett, J. Johnson, M. Key, *et al.*, "Photonuclear fission from high energy electrons from ultraintense laser-solid interactions," *Physical Review Letters*, vol. 84, no. 5, p. 903, 2000.

[18] C. Moore, A. Ting, S. McNaught, J. Qiu, H. Burris, and P. Sprangle, "A laser-accelerator injector based on laser ionization and ponderomotive acceleration of electrons," *Physical Review Letters*, vol. 82, no. 8, p. 1688, 1999.

[19] A. DiChiara, I. Ghebregziabher, R. Sauer, J. Waesche, S. Palaniyappan, B. Wen, and B. Walker, "Relativistic mev photoelectrons from the single atom response of argon to a 10 19 w/cm 2 laser field," *Physical Review Letters*, vol. 101, no. 17, p. 173002, 2008.

[20] S. y. Chen, A. Maksimchuk, and D. Umstadter, "Experimental observation of relativistic nonlinear thomson scattering," *Nature*, vol. 396, no. 6712, p. 653, 1998.

[21] N. Ekanayake, S. Luo, P. D. Grugan, W. B. Crosby, A. D. Camilo, C. V. McCowan, R. Scalzi, A. Tramontozzi, L. E. Howard, S. J. Wells, C. Mancuso, T. Stanev, M. F. Decamp, and B. C. Walker, "Electron shell ionization of atoms with classical, relativistic scattering," *Phys. Rev. Lett.*, vol. 110, p. 203003, May 2013.

[22] A. Maltsev and T. Ditmire, "Above threshold ionization in tightly focused, strongly relativistic laser fields," *Physical review letters*, vol. 90, no. 5, p. 053002, 2003.

[23] B. Quesnel and P. Mora, "Theory and simulation of the interaction of ultraintense laser pulses with electrons in vacuum," *Physical Review E*, vol. 58, no. 3, p. 3719, 1998.

[24] A. DiChiara, E. A. Chowdhury, G. Ongadi, B. C. Walker, and R. S. Tamosaitis, "Tem 00 terawatt amplification by use of micro-optic spatial mode conversion," *Optics Letters*, vol. 28, no. 21, pp. 2106–2108, 2003.

[25] A. D. DiChiara, I. Ghebregziabher, R. Sauer, J. Waesche, S. Palaniyappan, B. L. Wen, and B. C. Walker, "Relativistic mev photoelectrons from the single atom response of argon to a 10^{19} W/cm^2 laser field," *Phys. Rev. Lett.*, vol. 101, p. 173002, Oct 2008.

Chapter 6

SUMMARY

The work presented in this dissertation provided a comprehensive and thorough description of the design and fabrication process of a photoelectron spectrometer capable of quantifying photoelectrons with energies span from 20 keV to 2 MeV. To the best of our knowledge, the spectrometer presented here is the first one capable of measuring photoelectrons from the interactions between ultrastrong fields and single atom and molecule reliably and accurately. This brief final chapter provides a condensed summary of work completed in the dissertation, potential future direction and the continuation of the presented work will be provided at the end.

6.1 Apparatus for Photoelectron Measurements

In Chapter 3, we detailed the design and fabrication process of a high field photoelectron spectrometer. One of the most outstanding characteristics of this spectrometer is its capability of measuring photoelectron emitting from $\theta = 5°$ to $\theta = 100°$ with respect to the laser propagation vector $\hat{k}$ continuously. In addition, the exceptionally powerful custom-built electromagnets can deflect photoelectrons with energy up to 2 MeV with an energy resolution $\Delta E_k/E_k = 40\%$. The combination of those features, together with the ultrahigh vacuum interaction region, empowers the spectrometer to perform photoelectron measurements in ultrastrong intensity regime with single electron sensitivity.

6.2 Calibration and Photoionization Spectra

In Chapters 4 and 5, we thoroughly discussed the calibration process as well as the photoelectron spectra generated by both argon (Ar) and chloromethane (CH_3Cl)

at different angles. The spectrometer has extraordinary signal to noise ratio after implementing various noise reduction techniques. The Noise level has been suppressed to an extremely low 10^{-6} counts/shot. Three radioactive sources with beta emission energies span from 1 keV up to almost 1.2 MeV were employed in energy calibration. The results suggest an energy calibration accuracy of 10% for this spectrometer.

Subsequently, we measured Lorentz deflected photoelectrons created from the photoionization of argon and chloromethane with an ultrastrong, 1×10^{19} W/cm^2 laser field, measurements including photoelectron yields, energy and angular resolved spectrum. Maximum photoelectrons energy of 1.4 MeV was observed. The measurements demonstrated that the spectrometer is capable of collecting a high signal dynamic range ($> 10^4$) photoelectron spectra up to MeV energies with both atomic and molecular sample gases at different angles [1].

6.3 Future Considerations

Ultrahigh intensity lasers have opened frontiers in science and new challenges to quantify the observables. Photoelectron spectroscopy for ultrahigh intensity laser experiments with the atoms and molecules requires measurements beyond traditional spectroscopy.

Magnetic deflection has been the spectrometer design most widely used in atomic [1, 2], molecular [3], plasma [4], and condensed matter [5] high intensity laser experiments. The spectrometer presented here represents this technique applied to single atom and molecule interactions with ultraintense lasers. The apparatus provides the current technical limit of background event rates, single electron sensitivity, $\Delta E_k/E_k$, and angular resolution.

In this application, the primary concerns that emerged included the solid angle of collection, $\Delta E_k/E_k$ for a diverging source, and shielding of the detector from background light emitted by the highly excited ions at the laser focus. The energy resolution of the magnetic deflection photoelectron spectrometer can be further improved for enhanced precision measurements in the future. The current energy resolution of

40% can be improved by a larger dimension magnetic area and electromagnet with better axial field uniformity.

In the calibrations completed in Chapter 4, an electron gun instead of beta emission radioactive sources could increase the energy calibration accuracy and reliability. For experiments conducted in Chapter 5, we investigated only two polar angles $\theta = 75°$ and $\theta = 90°$. Such measurements can be extended with a series of angles to take full advantage of the high range of motion rotational magnetic analyzer, thereby acquiring a complete angular resolved photoelectron spectra.

The current spectrometer design could operate at intensities of up to 10^{20} W/cm^2. However, with the rapid development of laser technology, it is reasonable to expect even more intense laser fields. For intensities beyond 10^{20} W/cm^2, photoelectron energies are likely to exceed 100 MeV. Photoelectrons with utterly high energies possess speed extremely close to the speed of light, limitations in the magnetic field will result in larger gyromagnetic radii, and the detector geometry would need to be modified to allow small angle deflection measurements, of order a few degrees, rather than the 60° magnetic deflection angle used here. Modification of such kind can be implemented by reducing the separation between the laser focal point and the electromagnet analyzer, as well as reposition the detector.

An additional concern for petawatt lasers lies within the low pulse repetition rate. The experimental apparatus presented uses a single channel detector and single angle magnet analyzer. This design has successfully characterized the energy, angle resolved photoelectron spectra for the atomic response to ultrastrong fields over decades of the signal range. However, the current configuration has lengthened the data collections to exceedingly long durations on high energy photoelectron acquisitions. The next step would be to improve the magnet design and increase the analyzed angles and detection channels to determine a complete angle and energy resolved spectra with few laser shots. Current efforts are underway to extend these single channel results to a multiple angle magnet analyzer and multichannel analyzer design. Such improvements

should make collecting photoelectrons emitting with different energies and angles simultaneously achievable.

REFERENCES

[1] N. Ekanayake, S. Luo, P. D. Grugan, W. B. Crosby, A. D. Camilo, C. V. McCowan, R. Scalzi, A. Tramontozzi, L. E. Howard, S. J. Wells, C. Mancuso, T. Stanev, M. F. Decamp, and B. C. Walker, "Electron shell ionization of atoms with classical, relativistic scattering," *Phys. Rev. Lett.*, vol. 110, p. 203003, May 2013.

[2] C. I. Moore, J. P. Knauer, and D. D. Meyerhofer, "Observation of the transition from thomson to compton scattering in multiphoton interactions with low-energy electrons," *Phys. Rev. Lett.*, vol. 74, pp. 2439–2442, Mar 1995.

[3] S. Palaniyappan, R. Mitchell, R. Sauer, I. Ghebregziabher, S. L. White, M. F. Decamp, and B. C. Walker, "Ionization of methane in strong and ultrastrong relativistic fields," *Phys. Rev. Lett.*, vol. 100, p. 183001, May 2008.

[4] A. J. Goers, G. A. Hine, L. Feder, B. Miao, F. Salehi, J. K. Wahlstrand, and H. M. Milchberg, "Multi-mev electron acceleration by subterawatt laser pulses," *Phys. Rev. Lett.*, vol. 115, p. 194802, Nov 2015.

[5] P. Korneev, Y. Abe, K.-F.-F. Law, S. Bochkarev, S. Fujioka, S. Kojima, S.-H. Lee, S. Sakata, K. Matsuo, A. Oshima, *et al.*, "Laser electron acceleration on curved surfaces," *Applied Physics B*, 2017.

Appendix A

PERMISSION

Reproduced from [Luo, S. Y., Grugan, P. D., Demircioglu, Z., Hoos, A., Germain, Z., McIntyre, R. A., ... & Walker, B. C. (2019). MeV photoelectron spectrometer for ultraintense laser interactions with atoms and molecules. Review of Scientific Instruments, 90(7), 073104.], with the permission of AIP Publishing.

Appendix B

SOURCE CODES

B.1 Wire Gauge Determination

A python file to calculate the maximum magnetic field possible based on the geometry of the solenoid, the wire gauge and the power supply specifications.

```
import numpy as np
import matplotlib.pyplot as plt
import time
from math import pi, floor, ceil

# declare Constants

# maximum voltage of power supply
voltage = 24

# resistivity of copper
CuResist = 1.68*10**-8

# outer Diameter
OD = 3.5

# inner Diameter
ID = 2.5
```

```
# difference between outer diameter and the plate
delX = .5

# legnth of the solenoid
L = 4

# permeability of free space
muC = 1.256629*(10**-6)

# rest mass of electrons
mElectron = 9.10938356*(10**-31)

# charge of electrons
chargeE =1.60217662*(10**-19)

# speed of light
C = 2.99792458e8

# mass in energy units
MassEinJ = 8.187e-14

# convert from inches to meters
def inchToM(val):
    return val*0.0254


# possible wire gauge
potentialGauges = {10:2.5882*(10**-3),
                   12:2.0525*(10**-3),
```

```
                    14:1.6277*(10**-3),
                    16:1.2908*(10**-3),
                    18:1.0237*(10**-3),
                    20:0.8118*(10**-3)}


# define a function
def valueDetermination(gaug):


# set initial max magnetic Field
maxB = 0
for gaug in potentialGauges:
    Length = 0

    # first calculate how many
    # layers you can have:
    numLayers = floor(inchToM(delX) /
        potentialGauges[gaug])

    # then loops across the device
    numLoops = floor(inchToM(L) /
        potentialGauges[gaug])
    for i in range(0,numLayers):

        # Find radius of each layer,
        # noting that it grows with more
        # layers it wraps around
        radius = inchToM(3.5)/2 +
```

```
            i*(potentialGauges[gaug])

        # radius of one ring times
        # of rings at that layer
        Length += 2*pi*radius*numLoops

    # calculate current of the whole wire
    resistance = CuResist *
        Length / (pi*((potentialGauges[gaug] /2)**2))

    print(CuResist, L, pi, potentialGauges[gaug]/2)
    current = voltage / resistance

    # NOTE: cosntant mu normalized to 1
    B = numLayers * current

    # determine the maximum magnetic field value
    if B > maxB:
        maxB = B
        bestGauge = gaug
        bestLay = numLayers
        bestLoop = numLoops
        bestResist = resistance
        bestLength = Length


# print out the output
print('Maximum Magnetic Field is ', muC*maxB,
    'T Achieved with a wire of', bestGauge, 'gauge \n')
```

```
print('This requiers: ', bestLay, 'layers, and ',
            bestLoop, 'loops across the solenoid\n')

print('This has resistance: ', bestResist, '\n')

print('Current in the system in parallel: ',
            voltage / (resistance/2), 'A')

print('Current in the system in series: ',
            voltage / (resistance*2), 'A')


    return muC*maxB
```

B.2 Electron Trajectory Simulation

A simulation of the photoelectron trajectory when being deflected by the magnetic field, written in Python.

```
# import packages

import numpy as np
import matplotlib.pyplot as plt
import time
import math


# declare Constants

# mass of the electrons
mElectron = 9.10938356*(10**-31)

# charge of the electrons
chargeE =1.60217662*(10**-19)

# mass in energy units
MassEinJ = 8.187e-14

# spped of light in vacumm
C = 2.99792458e8


# define Electon Path Function
```

```
# in terms of energy in keV,
# current of electromagnet
# and the angle with respect to horizontal

def electronPath(energy, mA, theta):


    # define default status
    hitsTarget = False

    # define magnetic field magnitude
    # based on current
    B1 = mA*0.113
    B1 /= 1e4
    B2 = mA*0.078
    B2 /= 1e4
    B3 = mA*0.034
    B3 /= 1e4
    B4 = mA*0.012
    B4 /= 1e4

    # convert energy from keV to joule
    energy = energy*1.60218*10**(-16)

    # calculate magnitude of momentum
    # based on energy
    momentum = sqrt(energy**2 - MassEinJ**2)

    # giving momentum angular distribution
```

```
momenta = np.array([momentum*np.sin(theta),0,
                    momentum*np.cos(theta)])

# calculate initial relativistic speed
vinit = sqrt(((momentum/mElectron)**2)/
          (1+(momentum/mElectron)**2/(C**2)))

# calculate Lorentz factor
gamma = 1/(np.sqrt(1-(vinit**2)/(C**2)))

# print initial velocity for examination
print (vinit)


# declare maximum travle time based on
# spectrometer geometry
maxTime = 1*10**-7

# covert angle from radiand to degree
theta  = theta *math.pi / 180

# magnetic field center coordinate
# and radius
xc = 0.15875
zc = 0.03
r1 = 0.025
r2 = 0.035
r3 = 0.045
r4 = 0.055
```

```
# define initial velocity with
# angular dispersion
velocity = np.array([vinit*np.sin(theta),0,
        vinit*np.cos(theta)])


B = valueDetermination(gauge)

# define magnetic field in vector form
print(B)
BField1 = np.array([0,B1,0])
BField2 = np.array([0,B2,0])
BField3 = np.array([0,B3,0])
BField4 = np.array([0,B4,0])

# define initial position as lists
xpos = []
zpos = []

# define timestep
dt =  1e-10

# define maximum steps
steps = maxTime//dt

# define force in vector form
force = np.array([0,0,0])
```

```
# set inital position at origin
xpos.append(0)
zpos.append(0)

# start the loops
for i in range(1, int(steps)):
    print('Working at time step: ', i)
    print (velocity,"i",i)
    print (xpos)
    print (zpos)



    # new position after each time step
    try:
        xpos.append((xpos[i-1] +
            velocity[0]*dt))
        zpos.append((ypos[i-1] +
            velocity[2]*dt))

        print('appending worked')

        # determine which magnetic
        # field magnitude
        # to use according to
        # elecron coordinates
        if np.sqrt((xpos[i]-xc)**2 +
            (zpos[i] - zc)**2) <= r1:

            # calculate Lorentz force
```

```
        force =
            -chargeE*
            np.cross(velocity, BField1)

        # calculate new momentum
        # after each time step
        momenta = momenta +
        chargeE*np.cross(velocity,BField1)

        # calculate the
        # magnitude of the momentum
        momentum = sqrt(momenta[0]**2 +
                        momenta[2]**2)

        # calculate new velocity
        # using new momentum
        velocity =
            sqrt(((momentum/mElectron)**2)/
            (1+(momentum/mElectron)**2/(C**2)))

        print('velocity worked')

        # print out position
        print("x",xpos[i-1], "z",zpos[i-1])


    elif np.sqrt((xpos[i]-xc)**2 +
        (zpos[i] - zc)**2) <= r2:
```

```
        force = -chargeE*
            np.cross(velocity, BField2)

        momenta =
        momenta +
        chargeE*np.cross(velocity,BField2)

        momentum = sqrt(momenta[0]**2 +
                        momenta[2]**2)

        velocity =
        sqrt(((momentum/mElectron)**2)/
        (1+(momentum/mElectron)**2/(C**2)))


    elif np.sqrt((xpos[i]-xc)**2 +
        (zpos[i] - zc)**2) <= r3:

        force = -chargeE*
            np.cross(velocity, BField3)

        momenta =
        momenta +
        chargeE*np.cross(velocity,BField3)

        momentum = sqrt(momenta[0]**2 +
                        momenta[2]**2)

        velocity =
```

```
            sqrt(((momentum/mElectron)**2)/
            (1+(momentum/mElectron)**2/(C**2)))



        elif np.sqrt((xpos[i]-xc)**2 +
            (zpos[i] - zc)**2) <= r4:

            momenta =
            momenta +
            chargeE*np.cross(velocity,BField3)

            momentum = sqrt(momenta[0]**2 +
                            momenta[2]**2)

            velocity =
            sqrt(((momentum/mElectron)**2)/
            (1+(momentum/mElectron)**2/(C**2)))


        # if there is no magnetic field presented
        else:

            force = np.array([0,0,0])


        print ("x",xpos[i],"y",ypos[i],"i",i)

    # if there is an error
```

```
# following code allow
# us to know on which
# iteration it went worng
except:
    print('Error at timestep', i,'\n pos is
    (',xpos[i-1], ypos[i-1],')\n Force is: )
    break

    # dimension of the detecor
    if (0.109 <= xpos[i] and xpos[i] <= 0.13)
        and (zpos[i] > 0.1524):

    # where the electron hits
    print('X: ', xpos[i])

    # output the momentum
    print("momentum:", momentum)

    #output the energy
    print("energy:", energy)

    # print the total time
    # electron has travled
    print('time:',i*1e-10)

    # plot the trajectory
    fig = plt.figure()
    ax = fig.add_subplot(1,1,1)
```

```
plt.plot(xpos,ypos)
plt.xlim([-.04, .34])
plt.zlim([-.02, .5])
plt.plot([-0.05, 0.05], [0.37, 0.37],
    linewidth=1)

circ = plt.Circle((xc,zc), radius=r4,
        fill = True, color='c')

ax.add_patch(circ)

plt.show()
hitsTarget = True
break

# if does not hit the detecor, discard
if (ypos[i] > 0.1524 and xpos[i] < 0.1) or
(ypos[i] > 0.1524 and xpos[i]>0.15) :
print('TARGET MISSED')
break

return hitsTarget



# determine field value that can deflect
# certain energy of electrons
# to the detector
```

```
potentialBfield = []

for mA in range(1400, 1701 , 10):
    if electronPath(50, mA , 0):
        print('Bfield:', mA*113/1e3)
        print("ma: ",mA)
        potentialBfield.append(mA*113/1e3)


print(potentialBfield)


# calculate for certain magnetic field,
# upper and lower limit of
# electrons that can reach the detector.


for a in range (-20,61,10):
    potentialEnergies = []
    hits = []
    a /= 10
    for energy in  range(1000, 2001, 50):
        if electronPath(energy, 14450, a):
            print("angle: ", a)
            print('Energy: ', energy)
            potentialEnergies.append(energy)
            hits.append(1)
        else:
            hits.append(0)
```

```
print(potentialEnergies)

# write resluts into a .txt file
with open("%s.txt" % a, 'w') as f:
    for item in potentialEnergies:
        f.write("%s\n" % item)
```